

Numerical Investigation of Crack Development and Internal Force  
Networks on Intact Rocks

by

Yiru Zhou

A thesis submitted in partial fulfillment of the requirements for the degree of

Master of Science

in

Geophysics

Department of Physics

University of Alberta

© Yiru Zhou, 2024

# Abstract

The structural integrity of underground excavations, resource extraction processes, and the overall safety of geotechnical operations hinge on a comprehensive understanding of brittle rock failure mechanisms and the distribution of internal stress within these formations. This research sheds light on the underexplored aspects of geomechanics, showing the complexities of brittle rock behavior under stress, specifically focusing on the internal force distributions that precipitate failure.

This thesis consists of three parts. First, validating the efficacy of the Bonded Particle Method (BPM) through the simulation of elastic wave propagation in response to a single point force excitation. This verification process underscores the method's reliability and accuracy, establishing a solid foundation for its application in subsequent analyses. Second, the BPM is applied to create a Particle Flow Code (PFC) 2D model of Lac du Bonnet granite. We demonstrate the material genesis procedures, model calibration, and delineate the general characteristics of the granite model and showcase the practical application of the BPM in understanding rock behavior. Third, we explore the rock failure and internal force networks within brittle intact rocks. We investigate the crack development under compressive loading, discover five distinct internal force networks and critical angles within the cemented granular system, and find that the failure occurs along the force subgroups with high force gradient. These findings from this thesis not only advance our understanding of brittle rock failure mechanisms but also have significant implications for geotechnical engineering, mining, and petroleum extraction industries. This thesis represents a

stride forward in geomechanics, offering a comprehensive analysis of brittle rock failure mechanisms that bridge theoretical concepts with practical applications.

# Preface

This dissertation is submitted for the degree of Master of Science in Geophysics at the University of Alberta. The research described herein is original, and neither this nor any substantially similar dissertation was or is being submitted for any other degree or other qualification at any other university.

# Acknowledgements

I want to express my sincere appreciation to my supervisors, Dr. Mirko van der Baan and Dr. Claire Currie, for their invaluable guidance, continuous support, and insightful feedback throughout the entire process of this thesis. Their expertise and encouragement have been instrumental in shaping the direction and quality of this work. I am deeply appreciative of my committee members, Dr. Moritz Heimpel and Dr. Juliana Leung, for their valuable support, advice and comments.

Special thanks are extended to Drew Chorney and Dr. Jim Hazard for graciously sharing their work, which has enriched the research and expanded its scope.

This thesis owes much to the generous financial support provided by the sponsors of the Microseismic Industry Consortium, and Itasca for providing licenses for the PFC software. I am sincerely grateful for their investment in this research.

To my parents, Jianlin Zhou and Qunxiao Zhang, I would like to express my deepest gratitude for their unwavering love. Their constant support has been a source of strength and motivation.

To my dear friends, Dr. Xiaowen Liu, Edouard Kravchinsky, Dr. Wenxi Liao, Tian Kong, Jessy Ma, Dr. Haosen Wen, Dr. Shan Wu, Gloria Zhu, Dr. Xiaoxue Jiang, Yue Du, Yihan Wang, Ling Chen, Kirin Cao, Yixin Guan, Jinhui Jiao, Dr. Jingchuan Wang, and Toffee Ma, thank you all for your encouragement and companionship throughout this academic journey. Your friendship and love have made the challenges more manageable and the successes more meaningful.

# Contents

<b>1</b>	<b>Introduction</b>	<b>1</b>
1.1	Background . . . . .	1
1.2	Microseismicity and Acoustic Emissions . . . . .	2
1.3	Motivation . . . . .	5
1.4	Contributions . . . . .	6
1.5	Thesis structure . . . . .	7
<b>2</b>	<b>Geomechanics</b>	<b>9</b>
2.1	Overview . . . . .	9
2.2	Continuum Mechanics . . . . .	10
2.2.1	Stress . . . . .	10
2.2.2	Strain . . . . .	13
2.3	Fracture Mechanics . . . . .	14
2.3.1	The problem at hand . . . . .	15
2.3.2	Initiation of a Microcrack . . . . .	17
2.3.3	Microcrack Propagation and interaction . . . . .	19
2.3.4	Rock Failure . . . . .	20
2.3.5	Sibson's Fault Reactivation . . . . .	21
<b>3</b>	<b>Numerical Modelling and the Bonded Particle Method</b>	<b>26</b>
3.1	Introduction . . . . .	26
3.2	Numerical Modelling . . . . .	27

3.2.1	Continuum Modelling . . . . .	27
3.2.2	Discontinuum modelling . . . . .	28
3.3	Bonded Particle Method . . . . .	29
3.3.1	Linear Parallel Bond Model . . . . .	30
3.4	Model Formulation . . . . .	33
3.4.1	Force-Displacement Law . . . . .	34
3.4.2	Law of Motion . . . . .	36
3.5	Moment Tensor . . . . .	38
3.6	Numerical Damping . . . . .	41
<b>4</b>	<b>Semi-analytical and Numerical Simulation of Stress</b>	<b>45</b>
	Summary . . . . .	45
4.1	Introduction . . . . .	46
4.2	Method . . . . .	46
4.2.1	Test Setup . . . . .	46
4.2.2	Semi-analytical Approach . . . . .	46
4.2.3	Numerical Approach . . . . .	52
4.3	Result . . . . .	54
4.3.1	Displacement field . . . . .	54
4.3.2	Stress field . . . . .	57
4.4	Discussion . . . . .	58
4.5	Conclusion . . . . .	59
<b>5</b>	<b>Material genesis and calibration of the Bonded Particle Models</b>	<b>66</b>
5.1	Introduction . . . . .	66
5.2	Procedures of Material Genesis . . . . .	66
5.2.1	Step 1 Compact initial assembly . . . . .	67
5.2.2	Step 2 Install specified material pressure . . . . .	69
5.2.3	Step 3 Reduce the floating particles . . . . .	69

5.2.4	Step 4 Install parallel bonds and assign micro-properties	70
5.2.5	Step 5 Remove the specimen from the material vessel	71
5.3	Calibration of Lac du Bonnet BPM Model . . . . .	71
5.3.1	Young's Modulus, unconfined compressive strength and poison's ratio . . . . .	72
5.3.2	Failure Criterion, Cohesion and Frictional Angle . . .	74
5.4	Conclusion . . . . .	77
<b>6</b>	<b>Analysis of Crack Development and Force Networks Evolution</b>	<b>80</b>
6.1	Introduction . . . . .	80
6.2	Background . . . . .	81
6.2.1	Deformation stages . . . . .	81
6.2.2	Internal Force Networks . . . . .	82
6.3	Workflow . . . . .	83
6.3.1	Tracking crack development . . . . .	84
6.3.2	Identifying properties of the three distinct force networks . . . . .	84
6.3.3	Identify the failure mechanism, the relationship between the formation of cracks and force networks . .	85
6.4	Results . . . . .	85
6.4.1	Crack Development . . . . .	85
6.4.2	Internal Force Networks . . . . .	90
6.4.3	Final failure plane and spatial distribution of forces .	101
6.5	Discussion . . . . .	103
6.5.1	Crack Development . . . . .	103
6.5.2	Internal Force Distribution . . . . .	108
6.5.3	Relationship between Cracks and Internal Force Networks . . . . .	116

6.6	Conclusion . . . . .	128
<b>7</b>	<b>Conclusion</b>	<b>129</b>
7.1	Summary of Results . . . . .	129
7.2	Industry Implications . . . . .	131
7.3	Suggested future research . . . . .	132

# List of Tables

3.1	Numerical damping of static and dynamic mode. . . . .	43
4.1	Seismic properties of the granite assembly. . . . .	48
4.2	Micro-properties of granite assembly . . . . .	54
5.1	Micro properties used to calibrate the Lac du Bonnet granite model, where $R_{max}$ and $R_{min}$ are the minimum and maximum particle radius; $\bar{\lambda}$ is the radius multiplier; $E_c$ and $\bar{E}_c$ are the Young's moduli of the grains and cement; $k_n/k_s$ and $\bar{k}^n/\bar{k}^s$ are the ratios of normal to shear stiffness of the grains and cement; $\mu$ is the friction coefficient of the grain; $\rho$ represents the density; $\bar{\sigma}_c$ and $\bar{\tau}_c$ are the tensile and shear strength of the cement, respectively. . . . .	73
5.2	Failure compressive strength $\sigma_1$ for Lac du Bonnet granite model under different confining pressure $\sigma_3$ . . . . .	76

# List of Figures

2.1	The process of nucleation and propagation of a wing crack from the tip of a sliding crack with length $2c$ , with the directions of the maximum and minimum principal stresses indicated. The sliding crack and wing crack are oriented at angles of $\gamma$ and $\theta$ relative to the $\sigma_1$ direction. Modified after Rawling et al. (2002). . . . .	23
2.2	The Mohr diagram with the solid red line represents the Mohr-Coulomb criterion. $c_0$ is the cohesion. $\phi$ is the internal friction angle of the rock. Plane P represents the failure plane, $\sigma_{n,P}$ and $\sigma_{s,P}$ are the normal stress and shear stress on the failure plane P, $\theta$ represents the angle between failure plane P and $\sigma_3$ . Modified after van der Pluijm and Marshak (2004). . . . .	24
2.3	Stress ratio, $R = \sigma_1/\sigma_3$ , required for frictional reactivation versus reactivation angle, $\theta_r$ for rock with friction coefficient $\mu = 0.75$ . The region of favourably oriented, unfavourably oriented (UO) or severely misoriented for fault reactivation is indicated in the diagram. Reproduced from Sibson (1990) with permission of Seismological Society of America. . . . .	25

3.1	The grain-cement system based on the linear parallel bond contact model. The gray circular discs represent the grain, and each red bar mimics a cement entity as a parallel bond. The blue bars indicate the contacts which connect the grain centers and are perpendicular to the parallel bonds. The width of the blue bar is proportional to the magnitude of contact force. . . . .	31
3.2	Rheological components (top) and behavior (bottom) of the linear parallel bond model. Left: The linear Parallel Bond Model before the bond breakage. The edged-threadlike lines are notional surfaces representing the parallel bond between the grains (red for the upper grain and green for the lower one). The force-displacement at the parallel bond contact is described by the normal $\bar{k}_n$ stiffness, shear stiffness $\bar{k}_s$ , the tensile strength $\bar{\sigma}_c$ , cohesion $\bar{c}$ and the friction angle $\phi$ . The short and thick lines represent the linear contact between the grains. The force-displacement at the linear contact is described by the normal stiffness and shear stiffness, $k_n$ and $k_s$ , the friction coefficient $\mu$ and the surface gap $g_s$ . Right: Linear contact model after the bond breakage. Reproduced from Itasca Consulting Group (2008) with permission of Itasca International, Inc. . . . .	32
3.3	The primary operations that occur during each cycle sequence.	33
3.4	The two forms of single force couple. The left one has two forces $\mathbf{f}$ offset by distance $d$ such that a torque is exerted. The other force dipole exerts no torque. Modified after Stein and Wyssession (2009). . . . .	39

3.5	An example seismic event caused by formation of a tensile crack. (a) Light arrows represents the particle velocities while the heavy arrows represent the contact force changes after the bond breakage. The sub-vertical black line between the dark grey source particles represents the crack. (b) Its corresponding moment tensor. Reproduced from Hazzard and Young (2002) with permission of Elsevier. . . . .	44
4.1	Excitation of the single point force and location of the source. The yellow arrow represents the force in the positive y-direction. The red dot represents the source location, where the force acts on. The point force is an impulsive function defined by a half-period of a 1000k Hz sine wave. . . . .	47
4.2	Workflow for obtaining semi-analytical solution of the stress field. . . . .	47
4.3	Model setup of assembly. The inner square represents the observation region assigned with a realistic low damping parameter. The outer square ring represents the damping region assigned with a high damping parameter to absorb energy reflected from boundaries. . . . .	53
4.4	Analytical solution of displacement field results in unit of $m$ . From top to bottom, it shows the complete, near-field, far-field P, and far-field S displacement fields at the time of 1e-5 sec. The left column shows the x-displacement, and right column shows the y-displacement. . . . .	60
4.5	Comparison of far-field P displacement field results in unit of $m$ . The results on the left is the far-field P result from Aki and Richards (2002). On the right is our analytical far-field P displacement field obtained and decomposed into x- (top left) and y-directions (bottom left). . . . .	61

4.6	Comparison of far-field S displacement field results in unit of $m$ . The results on the left is the far-field S result from Aki and Richards (2002). On the right is our analytical far-field S displacement field obtained and decomposed into x- (top left) and y-directions (bottom left). . . . .	62
4.7	Comparison of the complete displacement fields of the analytical and numerical simulations at the time of $1e-5$ sec in unit of $m$ . The top row represents the x-component of the complete displacement field, and the bottom row represents for the y-component. The results on the left are the numerical results from PFC2D. The results on the left are the analytical solutions. . . . .	63
4.8	Semi-analytical solution of stress in unit of $Nm^{-2}$ . From top to bottom, it shows the complete, near-field, far-field P, and far-field S stress fields at the time of $1e-5$ sec. From left to right, each column shows the $\sigma_{xx}$ component, $\sigma_{yy}$ component, $\sigma_{yx}$ component of stress, respectively. . . . .	64
4.9	Comparison of the complete stress fields of the semi-analytical and numerical simulations at the time of $1e-5$ sec in unit of $Nm^{-2}$ . The top row represents the x-component of the complete stress field, and the bottom row represents the y-component. The results on the left are the numerical results from PFC2D. The results on the left are the semi-analytical solutions. . . . .	65
5.1	PFC2D model of 25.2 cm x 63 cm Lac du Bonnet granite and the distribution of grains. The material vessels are indicated by the four blue lines surrounding the granite. . . . .	68

5.2	The stress-strain response and accumulative number of cracks occurring during unconfined loading of the Lac du Bonnet granite model (a) compared to (b) a similar laboratory test. Modified from source: Martin (1993). . . . .	78
5.3	Stress-strain curve of the model under different confining conditions. . . . .	79
5.4	Compressive rock strength and failure criterion of Lac du Bonnet granite model expressed as Mohr circles at failure. The red stars indicate where the failures occur along the failure criterion. The black dashed line indicates the linearized Mohr-Coulomb failure criterion. . . . .	79
6.1	Top diagram: histories of stress-strain (blue line), moment tensor (orange circles) with four observation windows (red dots) 30% peak stress, 70% peak stress, peak stress and 60% peak stress (post-peak). Each observation window is selected from the middle of each deformation phase: elastic, strain-hardening, peak and strain-softening. Bottom diagram: monitoring the type and quantity of the cracks. . . . .	86
6.2	Rose diagrams at observation windows representing the strain-hardening, peak and strain-softening (post-peak) phases. The length of the bar represents the quantity of the cracks, and the azimuth represents the orientation of the cracks. . . . .	89
6.3	Spatial evolution of total force at elastic, strain-hardening, peak and strain-softening (post-peak) deformation stages in unit of $N$ . The colored veins represent the forces in the bonds. The colour of the vein indicates the force magnitude. The tensile forces are in blue, and the compressional forces are in red. . . . .	92

6.4	Spatial evolution of linear contact forces at elastic, strain-hardening, peak and strain-softening (post-peak) deformation stages in unit of $N$ . The colored veins represent the linear contact forces in the bonds. The colour of the vein indicates . . . . .	93
6.5	Spatial evolution of parallel bond forces at elastic, strain-hardening, peak and strain-softening (post-peak) deformation stages in unit of $N$ . The colored veins represent the parallel bond forces in the bonds. The colour of the vein indicates the force magnitude. . . . .	94
6.6	Spatial distribution of compressive parallel bond forces and tensile parallel bond forces at elastic, strain-hardening, peak and strain-softening (post-peak) deformation stages in unit of $N$ . The colored veins represent the parallel bond forces in the bonds. The thickness of the vein indicates the force magnitude. The tensile forces are in red, and the compressional forces are in light blue. . . . .	95
6.7	Evolution of total force for elastic, strain-hardening, peak and strain-softening (post-peak) deformation stages in unit of $N$ . The x-axis represents the force magnitude. The y-axis represents the count of occurrence in a natural logarithmic scale. . . . .	96
6.8	Evolution of linear contact force for elastic, strain-hardening, peak and strain-softening (post-peak) deformation stages in unit of $N$ . The x-axis represents the force magnitude. The y-axis represents the count of occurrence in a natural logarithmic scale. The linear contact forces are compressive only. . . . .	97

6.9	Evolution of compressive parallel bond forces for elastic, strain-hardening, peak and strain-softening (post-peak) deformation stages in unit of $N$ . The x-axis represents the force magnitude. The y-axis represents the count of occurrence in a natural logarithmic scale. . . . .	98
6.10	Evolution of tensile parallel bond forces for elastic, strain-hardening, peak and strain-softening (post-peak) deformation stages in unit of $N$ . The x-axis represents the force magnitude. The y-axis represents the count of occurrence in a natural logarithmic scale. . . . .	99
6.11	The 2D total force distribution for the elastic, strain-hardening, peak and post-peak phases for the elastic, strain-hardening, peak and post-peak phases. There are three force subgroups: Strong A, Strong B, and Weak Force subgroups. The critical angles are the boundaries between force subgroups. Radius represents the force magnitude. The azimuth presents the dipping of the linear parallel bond, and the colour represents the count of occurrence. . . . .	100
6.12	The 2D linear contact force distribution for the elastic, strain-hardening, peak and post-peak phases for the elastic, strain-hardening, peak and post-peak phases. There are three force subgroups: Strong A, Strong B, and Weak Force subgroups. The critical angles are the boundaries between force subgroups. Radius represents the force magnitude. The azimuth presents the dipping of the linear parallel bond, and the colour represents the count of occurrence. . . . .	101

6.13	The 2D compressive parallel bond force distribution for the elastic, strain-hardening, peak and post-peak phases for the elastic, strain-hardening, peak and post-peak phases. There are three force subgroups: Strong A, Strong B, and Weak Force subgroups. The critical angles are the boundaries between force subgroups. Radius represents the force magnitude. The azimuth presents the dipping of the linear parallel bond, and the colour represents the count of occurrence. . . . .	102
6.14	The 2D tensile parallel bond force distribution for the elastic, strain-hardening, peak and post-peak phases for the elastic, strain-hardening, peak and post-peak phases. For tensile forces, there is only one Weak force subgroup with critical angle $38^\circ$ . Radius represents the force magnitude. The azimuth presents the dipping of the linear parallel bond, and the colour represents the count of occurrence. . . . .	103
6.15	The total force and acoustic emissions after peak pressure. On the left graph, veins in the background are forces in bonds with colour-coded magnitudes and the thick dashed lines represent the location of the major shearing plane. On the right graph, the crosses represent the moment tensor of acoustic emissions. The size of the cross is proportional to the magnitude, which is also color-coded. . . . .	104
6.16	Decomposition of total force distribution according to the critical angles at the peak stage. a) The 2D force distribution with critical angles, $38^\circ$ and $64^\circ$ , indicated by dashed lines of yellow and blue respectively. b) The angular distribution of forces is colour-coded by different force subgroups according to the critical angles. c) The 1D force distribution of different force subgroups. . . . .	110

6.17	Decomposition of linear contact force distribution according to the critical angles at the peak stage. a) The 2D force distribution with critical angles, 38° and 64°, indicated by dashed lines of yellow and blue respectively. b) The angular distribution of forces is colour-coded by different force subgroups according to the critical angles. c) The 1D force distribution of different force subgroups. . . . .	111
6.18	Decomposition of compressive parallel bond force distribution according to the critical angles at the peak stage. a) The 2D force distribution with critical angles, 38° and 64°, indicated by dashed lines of yellow and blue respectively. b) The angular distribution of forces is colour-coded by different force subgroups according to the critical angles. c) The 1D force distribution of different force subgroups. . . . .	112
6.19	Decomposition of tensile parallel bond force distribution according to the critical angles at the peak stage. a) The 2D force distribution with critical angles at 38°, indicated by dashed blue line. b) The angular distribution of forces is colour-coded by different force subgroups according to the critical angles. c) The 1D force distribution of different force subgroups. . . . .	113
6.20	The development of the Weak subgroup of total forces throughout the deformation stages: elastic, strain-hardening, peak, and strain-softening. . . . .	114
6.21	The development of the Strong B subgroup of total forces throughout the deformation stages: elastic, strain-hardening, peak, and strain-softening. . . . .	115

6.22	The development of the Strong A subgroup of total forces throughout the deformation stages: elastic, strain-hardening, peak, and strain-softening. . . . .	116
6.23	The development of the Weak subgroup of linear contact forces throughout the deformation stages: elastic, strain-hardening, peak, and strain-softening. . . . .	117
6.24	The development of the Strong B subgroup of linear contact forces throughout the deformation stages: elastic, strain-hardening, peak, and strain-softening. . . . .	118
6.25	The development of the Strong A subgroup of linear contact forces throughout the deformation stages: elastic, strain-hardening, peak, and strain-softening. . . . .	119
6.26	The development of the Weak subgroup of compressive parallel forces throughout the deformation stages: elastic, strain-hardening, peak, and strain-softening. . . . .	120
6.27	The development of the Strong B subgroup of compressive parallel forces throughout the deformation stages: elastic, strain-hardening, peak, and strain-softening. . . . .	121
6.28	The development of the Strong A subgroup of compressive parallel forces throughout the deformation stages: elastic, strain-hardening, peak, and strain-softening. . . . .	122
6.29	The development of the horizontal subgroup of tensile parallel forces throughout the deformation stages: elastic, strain-hardening, peak, and strain-softening. . . . .	123
6.30	The development of the vertical subgroup of tensile parallel forces throughout the deformation stages: elastic, strain-hardening, peak, and strain-softening. . . . .	124

- 6.31 Compressive bonds, total forces and shear cracks at the peak phase. Top: Orientation and count of the bonds under compression. Radius represents the count. The azimuth presents the orientation of the linear parallel bond, and the colour represents the count of occurrence. Middle: 2D total force distribution. Radius represents the force magnitude. The azimuth presents the orientation of the force in the linear parallel bond, and the colour represents the count of occurrence. Bottom: Angular distribution of shear cracks. The azimuth presents the orientation of the shear cracks, and the colour represents the count of occurrence. . . . . 126
- 6.32 Tensile bonds, tensile parallel bond forces and shear cracks at the peak phase. Top: Orientation and count of the bonds under tension. Radius represents the count. The azimuth presents the orientation of the tensile parallel bond, and the colour represents the count of occurrence. Middle: 2D tensile parallel bond force distribution. Radius represents the force magnitude. The azimuth presents the orientation of the force in the linear parallel bond, and the colour represents the count of occurrence. Bottom: Angular distribution of tensile cracks. The azimuth presents the orientation of the tensile cracks, and the colour represents the count of occurrence. . . . . 127

# Chapter 1

## Introduction

This chapter lays the groundwork by providing an overview of the topic, examining previous academic research, and explaining the reasons and contributions of the current study. The goal of this thesis is to increase our understanding of the mechanisms and distribution of internal forces that cause brittle rocks to fail. This knowledge will provide fresh perspectives on fracturing processes and aid in mitigating associated risks.

### 1.1 Background

Brittle rock failure significantly influences the stability of subterranean structures, the productivity of resource extraction, and the overall safety of geotechnical operations. By employing numerical simulations, we deepen our understanding of the mechanisms behind rock failure, providing essential insights that aid in the planning and analysis of geotechnical operations, including hydraulic fracturing. (Fink, 2013). Hydraulic fracturing creates a network of cracks, making it easier for trapped hydrocarbons to flow and be extracted to the surface. As a result, it allows access to oil and natural gas

reserves that were previously inaccessible. Hydraulic fracturing has completely transformed energy production, significantly impacting the energy industry, particularly in North America. Hydraulic fracturing has played a crucial role in the energy sector revolution over the past few decades, greatly influencing the economies of the United States and Canada (Soeder, 2018).

However, despite its benefits, hydraulic fracturing has also received substantial criticism and concern, including its potential impact of the technique on air and water quality, as well as the potential for induced earthquakes (Keranen and Weingarten, 2018; Shirzaei et al., 2016; Lee, 2002). In the future, it is likely that hydraulic fracturing technique will continue to evolve, with a focus on improving its environmental impact and minimizing the seismic risks. Most human-induced seismicity involves rock fracturing caused by various geological operations, including but not limited to hydraulic fracturing (Maxwell, 2014), such as wastewater injection (Ellsworth, 2013) and mining (Gibowicz, 1994). Thus, gaining knowledge about the mechanics of brittle rock failures becomes fundamental and crucial for these practices. In our research, we will provide insights into its fracturing geomechanics and its correlated internal stress distribution that can promote the development of optimizing hydraulic fracturing while ensuring its safe and sustainable use in the future.

## **1.2 Microseismicity and Acoustic Emissions**

There are two types of hydraulic-fracturing-induced seismicities: microseismicity and "felt" higher-magnitude seismicity (Bao and Eaton, 2016; Clarke et al., 2014; Shipton, 2012). Microseismicity or microseismic events are typically characterized by magnitudes of  $M_w \leq 3$ , and are usually not

felt at the Earth’s surface. These occurrences are frequently within the  $-3.0 \leq M_w \leq 0$  (Warpinski et al., 2012). However, larger magnitude seismic events can be created in the vicinity of the stimulated well when there are pre-existing faults, and some of these may reach magnitudes of  $M_w > 3$  and be felt at the surface.

Over the past decade, microseismic monitoring has emerged as a highly effective technique for hydraulic fracture diagnostics and control (Cipolla and Wright, 2000). The microseismic monitoring technique can be used for detecting and imaging the geometry of fracture networks and evaluating the distribution of stimulated reservoir volume (Rutledge and Phillips, 2003), which can provide valuable insights into the behaviour of subsurface reservoirs and the efficiency of hydraulic fracturing treatments.

The theoretical foundation of microseismic monitoring is based on acoustic emission (AE) and seismology principles. While field-scale hydraulic fracturing stimulation is a common source of microseismicity, microseismicity can also be induced through laboratory-scale stimulation, which is called acoustic emission (AE). In recent years, there has been an increase in laboratory experiments aimed at investigating fracture behaviour (Li et al., 2017; Wang et al., 2018), to improve our understanding of the mechanical properties of fractures and enhance the effectiveness of field-scale stimulation.

Collecting AE events in modern laboratories depends on computer-based detection, signal conversion, and localization (Labuz et al., 2001; Lockner, 1993). However, AE events may not be detected by acoustic emission sensors for various reasons, such as the low amplitude of the event, background noise levels, limited sensor coverage, signal attenuation, and insuffi-

cient sensor sensitivity. Analyzing the rock fracture behaviours in laboratories is challenging because of the constrained measurements, unreproducible rock specimen, and complex and interactive micromechanical processes involved. However, numerical simulations are becoming increasingly sophisticated with new algorithms and software tools that can handle complex geometries and loading conditions. Finite element numerical models have been applied to study these complex fracture patterns (Shah et al., 1997; Warpinski et al., 1994; Vandamme and Curran, 1989) while similar laboratory experiments also have conducted (Scott Jr et al., 2000; Groenenboom and Dam, 2000). A comparison of laboratory observations with numerical simulations produces some disagreements in terms of fracture patterns and fracture type to some extent. For a real failure and cracks to occur, interactions between micro-cracks (Okui and Horii, 1995) must occur. Therefore, because of its nature, the Discrete Element Method (DEM) has become more common in recent years to explain the micro-mechanical behaviour of rocks further. Numerous studies have shown that the Discrete Element Method, can accurately model emergent non-linear stress-strain behaviours at different confining pressures (Cundall and Strack, 1979a; Hazzard and Young, 2004). Furthermore, the DEM has proven to be a successful tool for studying various aspects of rock mechanics. For instance, it has been utilized to investigate rock fracture (Hunt et al., 2003; Young et al., 2000; Donzé et al., 1997; van der Baan and Chorney, 2019), crack propagation and coalescence (Hadi et al., 2014; Camones et al., 2013), as well as acoustic emission activity (Hazzard et al., 2000; Khazaei et al., 2015).

## 1.3 Motivation

1. Supporting Academic Advancements. There are considerable knowledge gaps in terms of how the internal force distribution changes in brittle rocks. This thesis is dedicated to numerically simulating the changing internal force distribution in brittle rocks, presenting new data and insight that will fundamentally change the way geoscientists and engineers approach the understanding, modeling, and management of subsurface rocks.
2. Optimize resource extraction technology. In mining and hydraulic fracturing, understanding the distribution of internal forces can help improve mining methods. This knowledge helps plan efficient and safer mining strategies by guiding drilling patterns, using fracturing fluids, and predicting fracture paths, thereby increasing production and reducing environmental and safety hazards.
3. Mitigating earthquake risks. The study of how internal forces are distributed in brittle rocks is also relevant to induced seismicity (the human-induced earthquakes produced by hydraulic fracturing, geothermal energy recovery, and disposal of wastewater). Knowing how internal stresses change when our activity disturbs the ground could allow us to reduce the potential for triggering large earthquakes.

Overall, studying the brittle failure of rocks is important because it helps us understand the process of rock failure and helps mitigate seismic activity.

## 1.4 Contributions

Our complete analysis of brittle rock failure that bridges theory and practice helps to advance our understanding of rock behavior under compression.

The main contributions of this analysis are the following:

1. Identification the Characteristics of Catastrophic Failure. We found that the catastrophic failure occurs after the peak stress is reached, accompanied by the most significant stress drop, the largest acoustic emission size, the highest crack formation rate, the highest acoustic emission rate and the highest shear-tensile crack ratio.
2. Discovery of Five Distinct Subgroup Forces. A key finding of this work is the identification of five distinct force subgroups within the overall internal force distribution: Weak, Strong A, Strong B, Horizontal and Vertical force subgroups. This differentiation allows for a more detailed analysis of the forces and facilitates a deeper understanding of their individual and collective impacts on rock failure. This thesis also identifies critical angles that delineate the boundaries between the identified force subgroups.
3. Determination of Relationship between Internal Forces and Failure. Catastrophic failure occurs in areas with a high force gradient, oriented according to the critical angle identified between the Strong A and B subgroups. Thus, this critical predicts the orientation of the final catastrophic failure if the loading persistently escalates. Simultaneously, the critical angle observed between the Strong B and Weak force subgroups delineates the foundational angular threshold for the occurrence of shearing.

## 1.5 Thesis structure

The study is carried out in the next six chapters:

1. Chapter 1: Introduction. It introduces the fundamental concepts required to understand the thesis. This chapter also provides an overview of the scope of the study, the motivations behind investigating brittle rock failure mechanisms and internal stress distributions.
2. Chapter 2: Fundamentals of Geomechanics. Chapter 2 offers a geomechanics review. It covers topics such as stress and strain in geological materials, fracture mechanics, Sibson's fault reactivation and the Mohr Circle.
3. Chapter 3: Numerical Modelling and Bonded Particle Method. In this chapter, the focus is on introducing the bonded particle method and the linear parallel bonds, as well as discussing the Particle Flow Code (PFC) software formulation. This chapter provides an overview of how numerical modeling contributes to our understanding of rock behavior.
4. Chapter 4: Validation of the Bonded Particle Method. Chapter 4 aims to verify the bonded particle method's effectiveness through numerical and analytical/semi-analytical methods. The chapter focuses on simulating elastic wave propagation by exciting a particle with a single point force, demonstrating the method's accuracy and reliability in modeling complex geomechanical processes.
5. Chapter 5: Material Genesis and Calibration. This chapter shows the application of the bonded particle method by preparing a Particle

Flow Code (PFC) 2D model of Lac du Bonnet granite, which is the most studied type of granite in this area of research. It covers the material genesis procedures and model calibration and discusses the general characteristics of the granite model. The main objective is to illustrate the process of model preparation and calibration, providing a blueprint for similar future studies.

6. Chapter 6: Analysis of Crack Development and Force Networks Evolution. Chapter 6 further investigates rock failure mechanisms and internal force networks in brittle intact rocks. It brings new insights into crack development under compressive loading and the dynamics of internal force networks within the brittle cemented granular system. It also demonstrates the relationship between crack formation and internal force distributions. This chapter represents the core of the thesis, presenting key findings that contribute significantly to the field of geomechanics.
7. Chapter 7: Conclusions and Future Directions. This chapter summarizes the key findings of the thesis and emphasizes the contributions made to understanding brittle rock failure and internal stress distributions. Also, it discusses the implications of the research for geotechnical engineering, mining, and other relevant fields. Finally, it outlines potential directions for future research, suggesting ways to build upon the work presented in this thesis.

# Chapter 2

## Geomechanics

### 2.1 Overview

The purpose of rock mechanics is to understand the mechanical responses of soil and rock and why they deform as a sporadic or catastrophic event. How rock fails is a key element in civil, geotechnical and petroleum engineering practices and is gaining interest within the oil and gas industry. To ensure the successful development of an unconventional reservoir, the deformation mechanism and fracture distribution must be fully understood and investigated. A rock mass can comprise both intact rock and various types of discontinuities. The discontinuities are commonly known to play a significant role in the deformability and mechanical behaviour of rock masses (Wang et al., 2013).

In this chapter, we will describe two major topics in Geomechanics: continuum mechanics and fracture mechanics.

## 2.2 Continuum Mechanics

Continuum mechanics use mathematics to describe the behaviour of materials in terms of deformation and stress. It assumes that materials are continuous and homogeneous, isotropic, i.e., the material is considered a continuous substance rather than a collection of discrete particles. At the microscale, the matter is discontinuous. However, the macroscopic appearance of solid objects appears continuous, with their properties changing gradually without disruption. By studying continuum mechanics, we can gain insight into the physical behaviour of matter on larger scales while considering its fundamental discrete composition. Within the framework of Continuum Mechanics, stress and strain are used to describe the mechanical behaviour of geological materials.

### 2.2.1 Stress

For a force perpendicularly acting on a certain area, the Area is  $A$ , and the force is denoted  $F$ , then the stress  $\sigma$  is defined as:

$$\sigma = F/A \tag{2.1}$$

The sign of the stress  $\sigma$  is not uniquely defined, and in rock mechanics, the sign convention suggests positive signs for compressive stresses and vice versa. This is because the stresses dealt with in the applied scenario are mostly compressive, and this sign convention simplifies the problem.

A structure can be subjected to two types of stress: normal stress  $\sigma_n$  and shear stress  $\sigma_s$ . The normal stress is the component of stress  $\sigma_n$  perpendicular to a surface. The shear stress  $\sigma_s$  is the portion of the stress

parallel to a surface. The overall stress on the surface is the vector sum of normal and shear stress.

### Stress tensor

In order to describe the complete stress state acting on a point, it is necessary to identify stresses on the surfaces oriented in all three orthogonal directions. The stresses related to a surface perpendicular to the x-axis may be denoted  $\sigma_{11}$ ,  $\sigma_{12}$  and  $\sigma_{13}$ , representing the normal stress, shear stresses in y-directions and the z-direction, respectively. Similarly, stresses related to a surface perpendicular to the y-axis are denoted  $\sigma_{21}$ ,  $\sigma_{22}$  and  $\sigma_{23}$ , and stresses related to a surface perpendicular to the z-axis are denoted  $\sigma_{31}$ ,  $\sigma_{32}$  and  $\sigma_{33}$ . These nine stress components give the stress tensor a complete description of the stress state at the point. The first index indicates the surface's normal direction for stress components, and the second index indicates the force direction.

$$\boldsymbol{\sigma}_{ij} = \begin{bmatrix} \sigma_{11} & \sigma_{12} & \sigma_{13} \\ \sigma_{21} & \sigma_{22} & \sigma_{23} \\ \sigma_{31} & \sigma_{32} & \sigma_{33} \end{bmatrix} \quad (2.2)$$

It is also worth noting that no stress components are independent. For an object, an equilibrium state implies that no net translational or rotational force is acting on it, and forces on opposite faces must be equal and

opposite. In other words, the equilibrium state requires that:

$$\begin{aligned}\sigma_{12} &= \sigma_{21} \\ \sigma_{13} &= \sigma_{31} \\ \sigma_{23} &= \sigma_{32}\end{aligned}\tag{2.3}$$

Therefore, only half of the shear stress components are independent; together with the normal stress components, six of the stress components are independent.

### **Principal stresses**

There will be three special planes perpendicular to each other that experience only normal and no shear stress. The poles of these planes are the stress axes, and according to the magnitude of stress acting along the axes, they are called the principal stresses.  $\sigma_1 > \sigma_2 > \sigma_3$ .

$$\begin{pmatrix} \sigma_1 & 0 & 0 \\ 0 & \sigma_2 & 0 \\ 0 & 0 & \sigma_3 \end{pmatrix}\tag{2.4}$$

It is important to remember that the primary stresses are the eigenvalues of the stress tensor, while the stress axes correspond to its eigenvectors. The stress condition is triaxial if two of the three primary stresses are greater than zero. The stress is biaxial if two of the primary stresses are non-zero and one of them is zero. The state of stress is referred to as uniaxial if two of the primary stresses are zero.

## Effective stress

Effective stress is the resultant stress transmitted between a geological material's solid grains. It is the difference between the total stress and the pore fluid pressure. When fluid has an abundant presence, the pore fluid pressure would significantly reduce the effect of normal stress on the mineral grains, leaving the shear stresses unaffected.

### 2.2.2 Strain

Strain is the relative change in the position of points within a body that has undergone deformation. Given the stress tensor expressing forces acting inside a solid body, the corresponding strain tensor expresses the deformation of the body in reaction to these forces.

$$\epsilon_{ij} = \begin{bmatrix} \epsilon_{11} & \epsilon_{12} & \epsilon_{13} \\ \epsilon_{21} & \epsilon_{22} & \epsilon_{23} \\ \epsilon_{31} & \epsilon_{32} & \epsilon_{33} \end{bmatrix} \quad (2.5)$$

where  $\epsilon_{ij}(i, j = 1, 2, 3)$  represent the components of the strain tensor  $\epsilon_{ij}$ . The strain tensor is also symmetric, and only six components are independent. Symmetry requires that:

$$\begin{aligned} \epsilon_{21} &= \epsilon_{12} \\ \epsilon_{31} &= \epsilon_{13} \\ \epsilon_{23} &= \epsilon_{32} \end{aligned} \quad (2.6)$$

The strain tensor also can be expressed in terms of relative displacement when the displacements of the material particles are assumed to be much

smaller than the dimension of the body:

$$\epsilon_{ij} \equiv \frac{1}{2} \left( \frac{\partial u_i}{\partial x_j} + \frac{\partial u_j}{\partial x_i} \right) \quad (2.7)$$

where  $u_i (i = 1, 2, 3)$  is the relative displacement. The geometric equation is the relationship between strain  $\epsilon_{ij}$  and relative displacement  $u_i$ . Written out in matrix notation, this index equation becomes

$$\begin{bmatrix} \epsilon_{11} & \epsilon_{12} & \epsilon_{13} \\ \epsilon_{21} & \epsilon_{22} & \epsilon_{23} \\ \epsilon_{31} & \epsilon_{32} & \epsilon_{33} \end{bmatrix} = \begin{bmatrix} \frac{\partial u_1}{\partial x_1} & \frac{1}{2} \left( \frac{\partial u_1}{\partial x_2} + \frac{\partial u_2}{\partial x_1} \right) & \frac{1}{2} \left( \frac{\partial u_1}{\partial x_3} + \frac{\partial u_3}{\partial x_1} \right) \\ \frac{1}{2} \left( \frac{\partial u_2}{\partial x_1} + \frac{\partial u_1}{\partial x_2} \right) & \frac{\partial u_2}{\partial x_2} & \frac{1}{2} \left( \frac{\partial u_2}{\partial x_3} + \frac{\partial u_3}{\partial x_2} \right) \\ \frac{1}{2} \left( \frac{\partial u_3}{\partial x_1} + \frac{\partial u_1}{\partial x_3} \right) & \frac{1}{2} \left( \frac{\partial u_3}{\partial x_2} + \frac{\partial u_2}{\partial x_3} \right) & \frac{\partial u_3}{\partial x_3} \end{bmatrix} \quad (2.8)$$

Normal strains mean a direct length change of an object along the uni-axial direction resulting from normal stress. Based on Equation 2.7, the normal strain along the  $i$ -th direction can be expressed as:

$$\epsilon_i = \frac{\partial u_i}{\partial x_i} \quad (2.9)$$

And the shear strain  $\epsilon_{ij}$  is acting along the  $j$ -th direction on the plane perpendicular to  $x_j$  axis and expressed as:

$$\epsilon_{ij} = \frac{1}{2} \left( \frac{\partial u_i}{\partial x_j} + \frac{\partial u_j}{\partial x_i} \right) \quad (2.10)$$

## 2.3 Fracture Mechanics

Both tensile and compressive failures start at local tensile stresses around discontinuities. In general, cracks initiate when the material's intermolecular bonds are stretched and can break when the cohesive bond strength

is exceeded. Cracks propagate and extend unstably if excess energy is released by an incremental crack growth that is more than the energy required for producing that increment, resulting in residual energy. The cohesive strength and energy criterion must be met for a crack to elongate. In the case of tension, the intermolecular bonds are stretched and can break when the cohesive strength is exceeded, and this tension strength is easy to be exceeded. Therefore, the propagation depends on whether the second criterion is met. However, compressing those bonds deforms them rather than breaks them in compression, and the strain energy stored in the material could be enormous, but the cracks do not propagate. Hence, in compression cases, the fulfillment of the first criterion dictates cracking, not the second one.

Another significant difference between tensile and compressive failures of the brittle rocks is the cracking pattern. When a tensile load is applied, the crack initiates at the flaw tip and propagates perpendicular to the applied external load, and the area resisting the applied force decreases. However, when a compressive load is applied, the crack propagates parallel to the applied load, and there is no decrease in the resisting area.

### 2.3.1 The problem at hand

Griffith (1921) proposed that when the tensile stress at or near the tip of the inherent open crack exceeds the material's cohesive strength, the tensile crack will grow, and the failure process is initiated. The equation governs the tensile failure initiation in a biaxial compressive stress field is expressed as follows:

$$\sigma_1 = \frac{-8\sigma_t \left(1 + \frac{\sigma_3}{\sigma_1}\right)}{(1 - \sigma_3/\sigma_1)^2} \quad (2.11)$$

where the  $\sigma_t$  is the uniaxial tensile strength of the material. Griffith's stress model (Griffith, 1924) was used for decades to study crack initiation. It suggests that a crack will start propagating from the tips of minute defects when the tensile stress exceeds the cohesive bond strength.

Following Griffith's stress model theory, significant advancements have been made in understanding tensile fracture and enhancing its predictability. Engineers have been using Linear Elastic Fracture Mechanics (Irwin, 1957, 1960) and Non-Linear Fracture Mechanics (include using methods such as Crack Opening Displacement (Wells, 1961; Burdekin and Stone, 1966), J-Integral (Rice, 1968; Rice et al., 1968)) to predict and describe the tensile fracture behaviour of various materials subjected to diverse loading conditions. In tension, general equations are available, applicable and highly accurate, conforming to experimental results and verified over the years. On the other hand, unfortunately, our understanding of the fracture process in brittle materials under compression has not developed at a comparable pace. There is no well-established theory for compressive failure, and as a result, engineering design practices often rely on empirical guidelines.

Under a compressive stress field, the applicability of Griffith's stress model was evaluated experimentally by Lajtai (1971); he found that the tensile fracture first appeared at the point of maximum tensile stress, and the crack later adjusted its direction to propagate parallel to the applied compression stress. Also, Lajtai et al. (1989) argued that the assumptions and simplifications made in the stress model make this theory unsatisfactory for solving brittle fracture in compression critical in predicting the strengths and failure of rock and brittle materials in geotechnical applica-

tions. One significant constraint of stress-based theories is their assumption of a thin crack, often called the Griffith crack, which ignores the crack closure phenomenon in case of compression. Also, Griffith's stress model can not explain the stepped path followed by propagating cracks. In general, Griffith's theory is applicable to describe the initiation of open microcracks. However, a complete model is required to fully understand the growing process of the cracks within the rock under compressive stresses.

### **2.3.2 Initiation of a Microcrack**

Rocks are naturally heterogeneous, and those pre-existing heterogeneities lead to various source defects that lead to the local stress concentrations where a microcrack starts to initiate. At the source defects, a "sliding crack" micromechanical model has been analyzed (Brace and Bombolakis, 1963; Brace et al., 1966; Fairhurst and Cook, 1966). In this model, the cracks are assumed to be closed under compressive loading. It considers the tensile stress concentrates at the tips of inclined pre-existing cracks (Figure 2.1) with length  $2c$  and oriented at angle  $\gamma$  to  $\sigma_1$ , the maximum principal compressive stress.

When compressive stress is applied, it generates a shearing stress along the plane of the crack. If this shear stress is strong enough to surpass the frictional resistance of the closed crack, it will cause a frictional slippage, leading to concentrated tensile stress at both ends of the sliding crack. This tensile stress may trigger the formation of "wing cracks" at the two tips. As the stress acting on a material increases, wing cracks can form. The driving force for initiating wing crack is determined by the stress intensity factor  $K_I$ . Once the value of  $K_I$  reaches a critical value of  $K_{Ic}$ , wing cracks

will begin to form. According to a study by Rawling et al. (2002), if the preferred orientation is given by the angle  $\beta$ , which is between the weakness plane and the principal stress  $\sigma_1$ , then the wing cracks are more likely to nucleate from sliding cracks that are oriented at this angle *beta* at a stress that is:

$$\sigma_1 = \frac{\sin 2\beta + \mu(1 + \cos 2\beta)}{\sin 2\beta - \mu(1 - \cos 2\beta)}\sigma_3 + \frac{\sqrt{3}}{\sin 2\beta - \mu(1 - \cos 2\beta)} \frac{K_{Ic}}{\sqrt{\pi c}} \quad (2.12)$$

In addition to the sliding crack model, a range of possible models were developed to describe the crack growth initiated at different types of microstructural heterogeneities, e.g. cylindrical pores (Sammis and Ashby, 1986) and elastic mismatch (Dey and Wang, 1981). As there are certain shared characteristics among all of these models, it is possible that a generic model can capture the fundamental aspects of crack growth. According to studies by Rudnicki and Chau (1996); Costin (1983, 1985), a generic model can be developed to describe stress-induced cracking without specifying the microstructural heterogeneity. They introduced the proportionality factor  $f'$  to characterize the tensile stress concentrations. The relationship between the principal stresses for penny-shaped cracks at the initiation of crack growth can be described by the following equation:

$$\sigma_1 = \left( \frac{3}{f'} + 1 \right) \sigma_3 + \frac{3\pi}{2f'} \frac{K_{Ic}}{\sqrt{\pi a_0}} \quad (2.13)$$

where  $a_0$  is the initial crack length. Values of  $f'$  vary depending on the rock type, e.g. granite typically has a value of 1.14 for  $f'$ , while marble has a higher value of 2.09 and tuff has a value of 1.28 (Rudnicki and Chau, 1996).

The models mentioned above predict that there is a linear relationship between the principal stresses that are present when wing crack growth initiates. Experimental data has also been found to support the presence of this linear relationship (Ashby and Sammis, 1990).

### **2.3.3 Microcrack Propagation and interaction**

According to the sliding crack model, one of the consequences of wing crack growth is the formation of stress-induced extendable cracks that propagate parallel to the largest principal stress ( $\sigma_1$ ) as the stress increases. Furthermore, as the applied stress increases, shorter and less favourably oriented sliding cracks are likely to become active, resulting in the nucleation and initiation of new wing cracks distributed throughout the material. As the number and dimensions of wing cracks grow, the interaction among the various cracks and their associated stress fields becomes increasingly complex (Hori and Nemat-Nasser, 1983). Due to the complex nature of interactions of cracks and their stress fields, analyzing a single primary crack using traditional fracture mechanics has yet to be deemed adequate.

There are two primary approaches used to analyze the mechanics of crack interaction. The first approach relies on continuum damage mechanics (Krajcinovic, 1995). Continuum mechanics address inelastic and failure behaviours by monitoring the evolution of internal variables under loading. The internal variables represent the current microstructural arrangement (Rice, 1975). In this micromechanics-based damage model, the term "damage" refers to an internal variable that reflects the density and geometry of numerous microcracks and pores within the brittle rock.

The second approach is a stochastic method that involves extensive nu-

merical computation of a system of cracks with geometric properties following specific statistical distributions. Our research will employ this latter method to simulate the interactions among microcracks.

### **2.3.4 Rock Failure**

#### **Mohr's Circle**

Mohr's circle is a graphical representation of the transformation equations for plane stress problems, named after the German Civil Engineer Otto Mohr. He also developed the graphical technique for drawing the circle in 1882. Mohr's circle is useful in visualizing the relationships between the normal and shear stresses acting on various inclined planes at a point in a stressed body. We can also calculate principal stresses, maximum shear stresses, and stresses on inclined planes using Mohr's Circle.

The idea behind Mohr's Circle is that if normal stress is plotted on the x-axis, and shear stress is plotted on the y-axis, then the circle represents all possible combinations of normal and shear stress fall inside with interception on the x-axis at  $\sigma_1$  and  $\sigma_3$ . With that, Mohr's Circle can be used to calculate the shear and normal stress on any plane, and it is possible to predict the orientation of the failure plane where the failure strength of the rock is exceeded. A failure envelope can represent the failure condition. When differential stress  $\sigma_d$  is increasing,  $\sigma_d = \sigma_1 - \sigma_3$ , the Mohr's circles increase and eventually intersect the failure envelope and fracture occurs at the intersection with certain normal stress, shear stress and orientation.

A more general and frequently used failure criterion is the Mohr-Coulomb criterion which is represented by the solid red line in Figure 2.2 and can be

expressed as follows:

$$\sigma_s = \sigma_n \tan \phi + c_0 \quad (2.14)$$

$c_0$  is the cohesion.  $\phi$  is the internal friction angle of the rock and is related to the coefficient of internal friction  $\mu$  by  $\mu = \tan \phi$ . Figure 2.2 show the angle  $2\theta$ , which gives the position of the point where Mohr's circle touches the failure line.  $\theta$  and  $\phi$  are related by:

$$\phi + \frac{\pi}{2} = 2\theta \quad (2.15)$$

From Eq.2.15, we have

$$\theta = \frac{\pi}{4} + \frac{\phi}{2} \quad (2.16)$$

The allowable range for  $\phi$  is from  $0^\circ$  to  $90^\circ$ , and therefore, it is clear that  $\theta$  may vary between  $45^\circ$  and  $90^\circ$ .

In this case of Mohr-Coulomb criterion (Figure 2.2), Mohr's circle intersects the failure envelope and fracture occurs at the intersection P, the failure plane, with certain normal stress  $\sigma_{n,P}$ , shear stress  $\sigma_{s,P}$  and angle  $\theta$  which is between failure plane P and  $\sigma_3$ .

### 2.3.5 Sibson's Fault Reactivation

Sibson (1990) identified the failure plane as favourably oriented, unfavourably oriented or severely misoriented based on the failure plane orientation to the principle stresses. The favourable orientation for fault reactivation is where the stress ratio,  $R = (\sigma_1/\sigma_3) = (1 + \mu \cot \theta_r)/(1 - \mu \tan \theta_r)$ , is low, where  $\theta_r$  is the angle of reactivation between failure plane and  $\sigma_1$  (Figure 2.3). This stress ratio  $R$  reaches a minimum positive value at the optimum angle for reactivation given by  $\theta_r^* = \frac{1}{2} \tan^{-1}(1/\mu)$  and the stress ratio will be

$R^* = \left( \sqrt{1 + \mu^2} + \mu \right)^2$ . This stress ratio  $R$  reaches infinity when  $\theta_r = 2\theta_r^*$ , so-called the potential "locked-up" angle, indicating that the stress ratio needed for failure plane reactivation goes to infinity. When  $\theta_r > 2\theta_r^*$ , i.e., the "locked-up" angle is exceeded, failure plane reactivation would not occur unless the minimum principal stress becomes tensile  $\sigma_3 < 0$  or pore fluid press  $P_f > \sigma_3$ .

Therefore, according to Sibson (1990), for typical rock friction coefficients, it is unlikely that normal faults will be reactivated as high-angle reverse faults or thrusts as low-angle normal faults unless the effective least principal stress is tensile. In the previous section, we talked about the Mohr Circle, and it is worth noting that the  $\theta$  used in Mohr's Circle is the between failure plane and  $\sigma_3$  while the  $\theta_r$  used in Sibson's reactivation angle is the angle between failure plane and  $\sigma_1$ . We can link Sibson's optimum reactivation angle with the idea of Mohr's circle: the optimum condition for fault reactivation is exactly where the Mohr's Circle is touching the failure envelope (Figure 2.2), i.e., the angle of failure plane given by the Mohr's circle is same as the Sibson's optimum reactivation angle,  $\theta_r^* = 90^\circ - \theta$ .

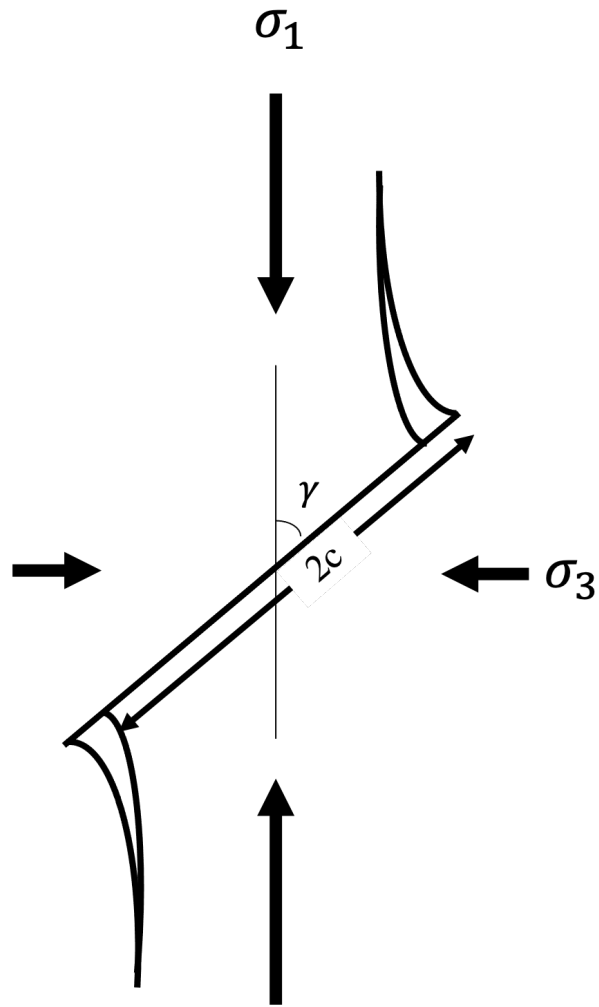


Figure 2.1: The process of nucleation and propagation of a wing crack from the tip of a sliding crack with length  $2c$ , with the directions of the maximum and minimum principal stresses indicated. The sliding crack and wing crack are oriented at angles of  $\gamma$  and  $\theta$  relative to the  $\sigma_1$  direction. Modified after Rawling et al. (2002).

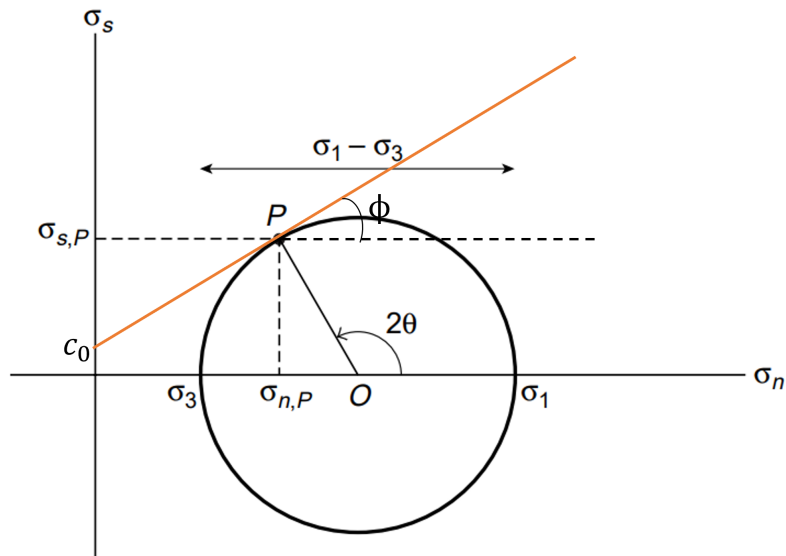


Figure 2.2: The Mohr diagram with the solid red line represents the Mohr-Coulomb criterion.  $c_0$  is the cohesion.  $\phi$  is the internal friction angle of the rock. Plane P represents the failure plane,  $\sigma_{n,P}$  and  $\sigma_{s,P}$  are the normal stress and shear stress on the failure plane P,  $\theta$  represents the angle between failure plane P and  $\sigma_3$ . Modified after van der Pluijm and Marshak (2004).

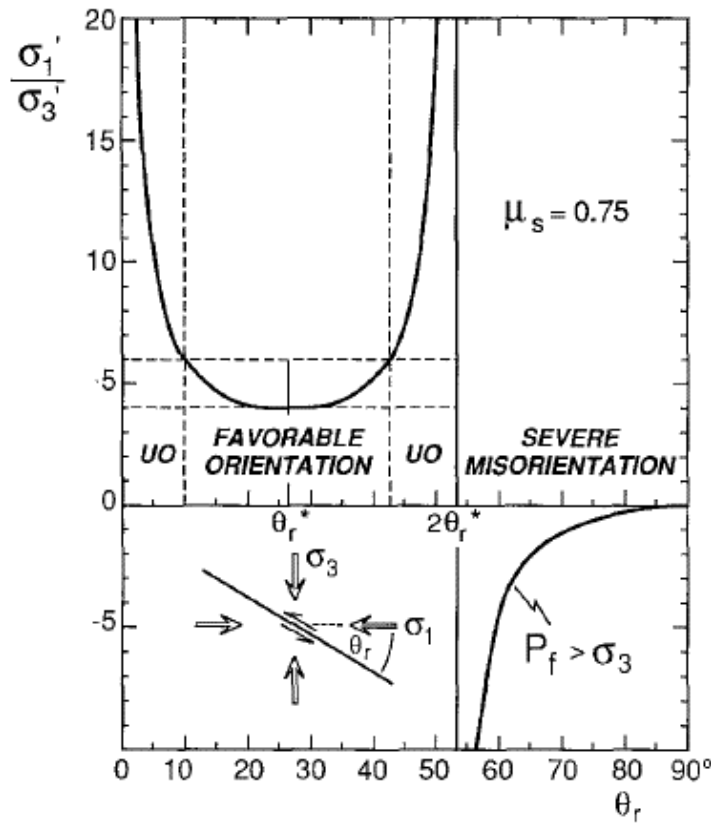


Figure 2.3: Stress ratio,  $R = \sigma_1/\sigma_3$ , required for frictional reactivation versus reactivation angle,  $\theta_r$  for rock with friction coefficient  $\mu = 0.75$ . The region of favourably oriented, unfavourably oriented (UO) or severely misoriented for fault reactivation is indicated in the diagram. Reproduced from Sibson (1990) with permission of Seismological Society of America.

# Chapter 3

## Numerical Modelling and the Bonded Particle Method

### 3.1 Introduction

In this chapter, the different types of numerical modelling methods will be introduced, followed by a discussion of the bonded particle method, software formulation, moment tensor and numerical damping.

The study of rock mechanics can be carried by physical, analytical and as well as numerical approaches. Thanks to the increased computing power and development of modelling methodology, we can conduct repeatable numerical simulations to investigate the geomechanical behaviour of brittle rocks with particle numbers comparable to those found in laboratory specimens. The Bonded Particle Method had been widely applied to rock and soil mechanics research in recent years (Cundall and Strack, 1979a; Cho et al., 2007; Kazerani and Zhao, 2010; Ivars et al., 2011; Potyondy et al., 2012a). In the mining, oil and gas extraction industries, the detailed physics of the rock deformation process is highly relevant to enhance productivity

and equipment design while ensuring the operations are safe.

## **3.2 Numerical Modelling**

In general, the numerical modelling methods of acoustic emissions and deformation analysis associated with failure processes in brittle rocks fall into two categories: 1) continuum modelling and 2) discontinuum modelling (Jing and Hudson, 2002).

### **3.2.1 Continuum Modelling**

Rock is a complex and discontinuous material. The continuum modelling method, e.g. the Finite Element Method (FEM), can simulate the variability in material types and non-linear constitutive behaviour in rock masses. Therefore, it allows accurate representation of complex geometries and inclusion of dissimilar materials.

For continuum modelling, the rock and soil mass model follow the assumption of continuity. The model is represented as a continuum divided into a set of simple geometrical mesh made by elements and nodes. Elements are the sub-domains; nodes are points at which exact solutions are calculated. Between nodes of a single element, The FEM exploits approximations to the connectivity of elements and continuity of displacements between elements, and the solutions are estimated through interpolation.

However, when simulating the process of fracturing in brittle rocks, the continuum modelling method is constrained by the requirement of the continuum assumption. Since continuity is required between neighbouring nodes, element sizes should be small, and the elements are limited to

small movement. Therefore, discontinuous features with large displacements, e.g. joints, are impossible to deal with (Nikolić et al., 2016). The FEM models require continuous re-meshing in order to simulate fracture growth. Therefore, the modelling of discontinuous features, including rock failures, fracture propagation and damage-induced failures in brittle rocks, becomes very restrictive and less efficient (Ibrahimbegovic, 2009; Wriggers, 2008). In contrast, natural discontinuities can be simulated in the discontinuum models; interactions between elements are constantly changing during the deformation processes.

### **3.2.2 Discontinuum modelling**

Most physical materials and systems are discontinuous, and rock is an obvious example of it. At the microscopic scale, rock is made of numerous amount of discrete grains. In discontinuum modelling, the rock mass is treated as an assemblage of interacting bodies subjected to external loads and undergoes significant motion with time and follows linear or non-linear stress-strain laws (Stead et al., 2006).

The Discrete Element Method is a discontinuum approach that efficiently explores the dynamic interactions of discontinuous objects. The Discrete Element Method's calculation procedure formulates and solves the dynamic equation of equilibrium for an assemblage of deformable rigid particles until the boundary conditions and motion laws are satisfied. As in the Finite Element Method, the Discrete Element Method accounts for complex non-linear interaction phenomena between bodies. We distinguish a discontinuous medium from a continuous medium through contacts or interfaces between the discrete bodies that comprise the system. Cundall and Hart

(1992) proposed that the definition of a Discrete Element Method applies to a computer program only if it: (a) allows finite displacements and rotations of discrete bodies, including complete detachment; and (b) recognizes new contacts automatically as the calculation progresses. Therefore, it provides the capability to represent discontinuities and the rotation of distinct bodies. However, it also implies that it requires an efficient algorithm for detecting and classifying the contacts between interacting bodies.

### **3.3 Bonded Particle Method**

Both soil and rock are materials composed of mineral grains. They could be very similar in their chemical composition, while they are very different in physical forms. For soils, those grains are readily disintegrated and mixed with water, air, and organic matter. However, the mineral grains in rocks are strongly bonded together only to be separated when a relatively considerable force is applied.

Cundall and Strack (1979b) implement the Discrete Element Method and apply disks and spheres to simulate the mechanical behaviour of unbonded particles. Since there is no cohesion between disks and spheres, such a system behaves like a granular material, such as soil. Nevertheless, according to the nature of rocks, we require a proper model to replicate the bonds between the mineral grains. Cundall and Strack (1979a) extend the Discrete Element Model to incorporate bonding between grains and argue that such a model's mechanical behaviour is similar to brittle rock's response. Such a modelling methodology is called the bonded particle method.

Since Cundall and Strack (1979a) firstly introduced the bonded particle method, it has been progressively improved and developed. The bonded-

particle modelling methodology now offers different microstructural models to simulate different forms of bonded material, e.g. incorporating clumped material (Cho et al., 2007) to mimic a group of glued particles that behave as a single rigid body, adding the smooth-joint contact model to mimic pre-existing large-scale joint (Mas Ivars et al., 2008) and flat-jointed contact model (Potyondy et al., 2012b) to mimic the microstructure of angular, interlocked grains.

### 3.3.1 Linear Parallel Bond Model

Cundall and Strack (1979a) propose a model for a rock represented by dense packing of non-uniform sized grains bonded together with parallel bonds at their contact point. This contact model is called the linear parallel bond model based on the author's two main arguments:

- Rock behaves like a cemented granular material of complex-shaped grains. Both the grains and the cement are breakable and deformable.
- The bonded particle model can mimic this system; circular discs of unit thickness directly mimic each grain, and the parallel bonds mimic the mechanical behaviour of a finite-sized piece of cement-like material.

This numerical grain-cement system (Figure 3.1), in principle, can replicate every aspect of the mechanical behaviours, and therefore demonstrate emergent behaviours and properties that match well with those of physical rock.

The linear parallel bond contact model provides the behaviour of two interfaces:

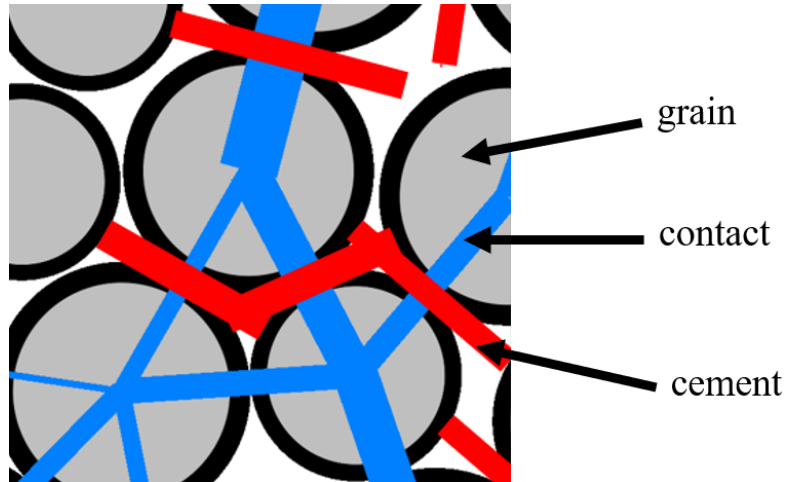


Figure 3.1: The grain-cement system based on the linear parallel bond contact model. The gray circular discs represent the grain, and each red bar mimics a cement entity as a parallel bond. The blue bars indicate the contacts which connect the grain centers and are perpendicular to the parallel bonds. The width of the blue bar is proportional to the magnitude of contact force.

- Parallel bond: a finite-size, linear elastic, and a bonded interface that describes the cement behaviour. The parallel bond carries forces and moments and resists tension and relative rotation. When the parallel bond interface is bonded, it is parallel with the linear contact interface (Figure 3.2). It is linearly elastic until the strength limit is exceeded and the bond breaks making it unbonded.
- Linear contact: an infinitesimal, linear elastic and frictional interface that describes the state of unbonded grains. The interface carries compressive and shear forces, but it does not resist tension and relative rotation. After the bond breaks, the parallel bond is removed. The unbonded linear parallel bond model is equivalent to the linear contact model.

When grains are bonded by cement, the grain behaviour is described

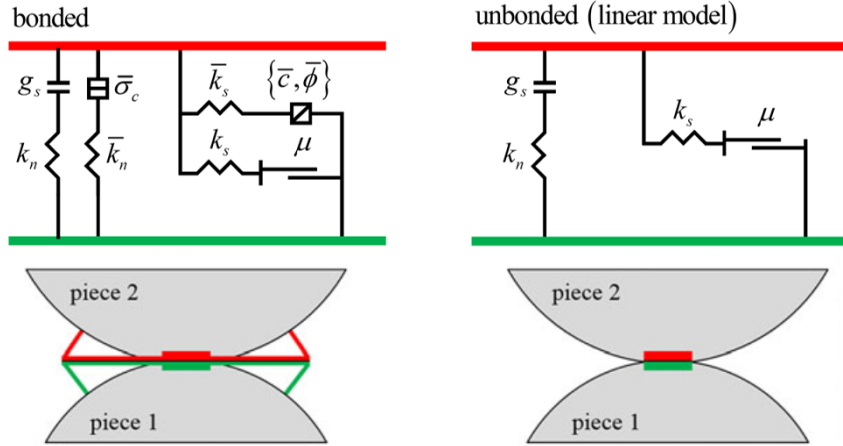


Figure 3.2: Rheological components (top) and behavior (bottom) of the linear parallel bond model. Left: The linear Parallel Bond Model before the bond breakage. The edged-threadlike lines are notional surfaces representing the parallel bond between the grains (red for the upper grain and green for the lower one). The force-displacement at the parallel bond contact is described by the normal  $\bar{k}_n$  stiffness, shear stiffness  $\bar{k}_s$ , the tensile strength  $\bar{\sigma}_c$ , cohesion  $\bar{c}$  and the friction angle  $\bar{\phi}$ . The short and thick lines represent the linear contact between the grains. The force-displacement at the linear contact is described by the normal stiffness and shear stiffness,  $k_n$  and  $k_s$ , the friction coefficient  $\mu$  and the surface gap  $g_s$ . Right: Linear contact model after the bond breakage. Reproduced from Itasca Consulting Group (2008) with permission of Itasca International, Inc.

by both parallel bond and linear contact interfaces. The parallel bonds can resist tension as well as transfer torques and moments. When the shear stress acting on the parallel bond exceeds the shear strength, or the tensile strength is exceeded, the parallel bond will break, and two grains become unbonded (Figure 3.2). Once the parallel bond breaks, it can not be healed. The bond material will be removed from the model along with its accompanying assigned properties, force and moment. Meanwhile, a micro-crack will form at the cement, replacing the parallel bond. In an unbonded state, grain behaviour is equivalent to that of the linear contact

model where the grains can still be in contact but are allowed to move freely.

### 3.4 Model Formulation

The Discrete Element Model's formulation is an explicit, time-stepping solution by executing a series of calculation cycles. During this cycling process, the interactions of bodies and emergent behaviours are continuously monitored. Each calculation cycle consists of a sequence of operations, termed cycle sequence. Figure 3.3 below shows a simplified cycle sequence that includes force-displacement law, contact detection and the law of motion.

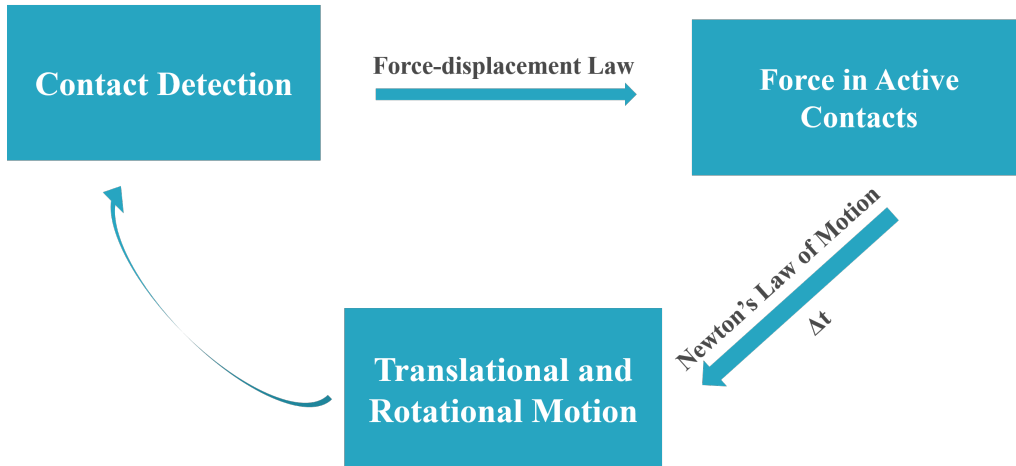


Figure 3.3: The primary operations that occur during each cycle sequence.

In the 2D model, the out-of-plane force component are not considered in the force-displacement law and the equations of motion. The two-dimensional grains can be considered as a collection of variable-radius cylinders with unit thickness.

### 3.4.1 Force-Displacement Law

The force-displacement law for the linear parallel bond 2D model updates the contact force and moment. It consists of the following steps (Cundall and Strack, 1979a):

1. Update the bond cross-sectional properties:

$$\bar{R} = \bar{\lambda} \begin{cases} \min(R^{(1)}, R^{(2)}), & \text{ball-ball} \\ R^{(1)}, & \text{ball-wall} \end{cases} \quad (3.1)$$

$$\bar{A} = 2\bar{R}, \quad (3.2)$$

$$\bar{I} = \frac{2}{3}\bar{R}^3, \quad (3.3)$$

where  $\bar{\lambda}$  is the radius multiplier used to set the parallel-bond radii. The particle size is non-uniformly distributed. The radii of the two particles  $R^{(1)}$  and  $R^{(2)}$  determine the parallel-bond radius  $\bar{R}$ .  $\bar{A}$  is the cross-section area, and  $\bar{I}$  is the moment of inertia of the parallel bond cross-section. The bond cross-section is a rectangle in 2D with unit thickness.

2. Update the parallel bond force  $\bar{\mathbf{F}}$ , normal force  $\bar{F}_n$  and shear force  $\bar{\mathbf{F}}_s$  components:

$$\bar{\mathbf{F}} = -\bar{F}_n \hat{\mathbf{n}} + \bar{\mathbf{F}}_s, \quad (3.4)$$

$$\bar{F}_n := \bar{F}_n + \bar{k}_n \bar{A} \Delta \delta_n, \quad (3.5)$$

$$\bar{\mathbf{F}}_s := \bar{\mathbf{F}}_s - \bar{k}_s \bar{A} \Delta \delta_s, \quad (3.6)$$

where tensile normal force is considered positive, and compressive force negative.  $\hat{\mathbf{n}}$  is the unit normal vector.  $\bar{k}_n$  and  $\bar{k}_s$  are the normal

stiffness and shear stiffness of the cement.  $\Delta\delta_n$  is the relative normal-displacement increment and  $\Delta\delta_s$  is the relative shear-displacement increment.

3. Update parallel bond moment  $\bar{\mathbf{M}}$ , twisting moment  $\bar{M}_t$  and bending moment  $\bar{\mathbf{M}}_{\mathbf{b}}$

$$\bar{\mathbf{M}} = \bar{M}_t \hat{\mathbf{n}} + \bar{\mathbf{M}}_{\mathbf{b}}, \quad (3.7)$$

$$\bar{M}_t := 0, \quad (3.8)$$

$$\bar{\mathbf{M}}_{\mathbf{b}} := \bar{\mathbf{M}}_{\mathbf{b}} - \bar{k}_n \bar{I} \Delta\boldsymbol{\theta}_{\mathbf{b}}, \quad (3.9)$$

where twisting moment  $\bar{M}_t$  is always zero for 2D model.  $\Delta\theta_t$  is the relative twist-rotation increment and  $\Delta\boldsymbol{\theta}_{\mathbf{b}}$  is the relative bend-rotation increment.

4. Update the maximum normal  $\bar{\sigma}$  and shear stresses  $\bar{\tau}$  acting on the periphery of a parallel bond:

$$\bar{\sigma} = \frac{\bar{F}_n}{A} + \frac{\|\bar{\mathbf{M}}_{\mathbf{b}}\| \bar{R}}{\bar{I}}, \quad (3.10)$$

and

$$\bar{\tau} = \frac{\|\bar{\mathbf{F}}_{\mathbf{s}}\|}{A}. \quad (3.11)$$

5. Update bond breakage. If the maximum tensile stress exceeds the tensile strength ( $\bar{\sigma} > \bar{\sigma}_c$ ) or the maximum shear stress exceeds the shear strength ( $\bar{\tau} > \bar{\tau}_c$ ), the parallel bond breaks in tension or shear. The shear strength  $\bar{\tau}_c = \bar{c} - \sigma \tan \bar{\phi}$ , where  $\bar{c}$  is the cohesion and  $\sigma = \bar{F}_n / \bar{A}$ .  $\sigma$  is the average normal stress acting on the parallel bond

cross-section area. The parallel bond is removed from the model along with its accompanying force, moment and stiffness by returning their values to zeros.

With the force and moment updated for each contact, the next movement of grain can be predicted by applying Newton's law of motion.

### 3.4.2 Law of Motion

The resultant force and moment acting upon a rigid particle determine the motion. Combining the forces and moments of the linear contact and the parallel bond component, we can update the resultant force and moment acting on a particle in the linear parallel bond model:

$$\mathbf{F} = \mathbf{F}^l + \bar{\mathbf{F}}, \quad \mathbf{M} = \bar{\mathbf{M}}, \quad (3.12)$$

where  $\mathbf{F}$  is the resultant force,  $\mathbf{F}^l$  is the linear contact force, and  $\bar{\mathbf{F}}$  is the parallel-bond force.  $\mathbf{M}$  is the resultant moment, and it equals to the parallel-bond moment  $\bar{\mathbf{M}}$  since the linear contact has no moment. The linear contact force  $\mathbf{F}^l$  is updated as in the linear contact model. The force  $\bar{\mathbf{F}}$  and moment  $\bar{\mathbf{M}}$  in the parallel bond are updated as described force-displacement law (Equations 3.4 and 3.7). With the updated forces and moments, the motion can be calculated in translational and rotational motion, as explained next.

#### Translational Motion

The translational motion can be described by its position  $\mathbf{x}$ , velocity  $\dot{\mathbf{x}}$  and acceleration  $\ddot{\mathbf{x}}$ , which can be solved from the equation of translational

motion:

$$\mathbf{F} = m(\ddot{\mathbf{x}} - \mathbf{g}), \quad (3.13)$$

where  $\mathbf{F}$  is the resultant force,  $m$  is the mass of the grain,  $\mathbf{g}$  is the gravitational loading. This translational equations of motion are solved via the second order Velocity Verlet algorithm (Verlet, 1967). Given resultant force solved at time  $t$  and calculation timestep  $\Delta t$ , the velocity at half timestep is calculated as:

$$\dot{\mathbf{x}}^{(t+\Delta t/2)} = \dot{\mathbf{x}}^{(t)} + \frac{1}{2} \left( \frac{\mathbf{F}^{(t)}}{m} + \mathbf{g} \right) \Delta t, \quad (3.14)$$

Using the half step velocity, we can obtain the position of grain at time  $t + \Delta t$ :

$$\mathbf{x}^{(t+\Delta t)} = \mathbf{x}^{(t)} + \dot{\mathbf{x}}^{(t+\Delta t/2)} \Delta t. \quad (3.15)$$

### Rotational Motion

The translational motion can be expressed by its angular velocity  $\boldsymbol{\omega}$ , angular acceleration  $\dot{\boldsymbol{\omega}}$ :

$$\mathbf{L} = \mathbf{I}\boldsymbol{\omega}, \quad (3.16)$$

where  $\mathbf{L}$  is the angular momentum,  $\mathbf{I}$  is the inertia tensor. By taking the time derivative we obtain the resultant moment  $\mathbf{M}$  acting on the rigid body:

$$\mathbf{M} = \dot{\mathbf{L}} = \mathbf{I}\dot{\boldsymbol{\omega}} + \boldsymbol{\omega} \times \mathbf{L}, \quad (3.17)$$

For a disk-shaped 2D body with radius  $R$ , the rotational axis remains in the out-of-plane direction. Therefore, the x-component and y-component

of the angular velocities and moment are zero:

$$\omega_x = \omega_y \equiv 0, \quad M_x = M_y \equiv 0. \quad (3.18)$$

The resultant moment  $\mathbf{M}$  is equivalent to the z-component moment. Equation 3.17 reduces to:

$$M_z = I\omega_z, \quad (3.19)$$

where the moment of inertia  $I = \frac{1}{2}mR^2$ . The half step angular velocity is obtained at time  $t + \Delta t/2$ :

$$\boldsymbol{\omega}^{(t+\Delta t/2)} = \boldsymbol{\omega}^{(t)} + \frac{1}{2} \left( \frac{M_z^{(t)}}{I} \right) \Delta t. \quad (3.20)$$

According to the updated motion of grains, we can then detect the contact between the grains according to their new position. The force-displacement law is applied again to solve for the contact forces, therefore establishing a complete operation cycle with timestep  $\Delta t$ .

The sections above describe the basics of the numerical modelling and bonded particle method. In the following sections of this chapter, we will introduce the additional concepts that play a significant role in implementing the numerical modelling.

## 3.5 Moment Tensor

### Definition of Moment Tensor

A seismic source in the Earth is usually modelled as a slip on a fault which is a discontinuous surface in displacement in the elastic media. To describe the fault slip, we must consider the relationship between the slip and forces

within the Earth. We could have a force couple consists of two force vectors of magnitude  $\mathbf{f}$  (Figure 3.4), acting in opposite directions and separated by a distance  $d$  perpendicular or along the force direction. The case with the distance  $d$  perpendicular to the force direction generates net torques, and the angular momentum is not conserved. For natural earthquakes, the source mechanism could only result from internal forces acting in opposing directions on a fault, so that momentum would be conserved. Therefore, it implies that there must have a complementary force couple to balance the momentum for natural earthquakes, and the resulting two force couples are called a double couple.

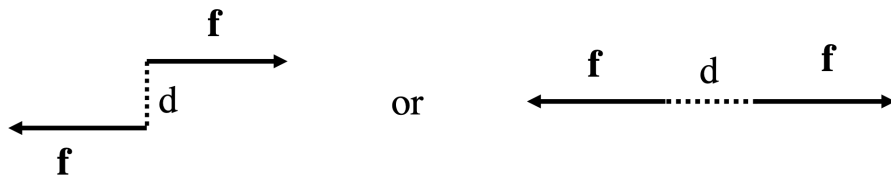


Figure 3.4: The two forms of single force couple. The left one has two forces  $\mathbf{f}$  offset by distance  $d$  such that a torque is exerted. The other force dipole exerts no torque. Modified after Stein and Wysession (2009).

A force couple in a 3D Cartesian coordinate system with axes 1, 2, 3, consists of two forces acting together. For example,  $M_{12}$  consists of two forces of magnitude  $\mathbf{f}$  acting on opposite directions along the 1-axis, separated by a distance  $d$  along the 2-axis. The magnitude of the force couple is  $\mathbf{f}d$  with unit of  $\text{dyn} \cdot \text{cm}$  or  $\text{N} \cdot \text{m}$  Aki and Richards (2002). Combining these nine force couples of different orientations into a matrix, we obtain

the seismic moment tensor  $\mathbf{M}_{ij}$ :

$$\mathbf{M}_{ij} = \begin{bmatrix} M_{11} & M_{12} & M_{13} \\ M_{21} & M_{22} & M_{23} \\ M_{31} & M_{32} & M_{33} \end{bmatrix} \quad (3.21)$$

The moment tensor represents a seismic source by a set of equivalent forces that produce the same displacements at the Earth's surface as the actual forces active at the source. Thus, it can precisely describe complex fault geometries of internal seismic sources via its force couple components. From the moment tensor, we also obtain the size of an earthquake from its seismic moment  $M_0$ . It is a scalar parameter that quantifies the amplitude of a moment tensor.

$$M_0 = \frac{1}{\sqrt{2}} \left( \sum \mathbf{M}_{ij}^2 \right)^{\frac{1}{2}}, \quad (3.22)$$

Kanamori (1977) introduced the concept of moment magnitude  $M_w$ , which is a logarithmic scale defined in terms of the seismic moment of the earthquake.

$$M_w = \frac{2}{3} \log_{10} (M_0) - 6. \quad (3.23)$$

### **Simulative Approach**

A bond breakage in the modelling represents a single micro-crack. When the bond breaks, the two source particles on either side of the crack will move. Therefore, a change in force will be induced around the source. If each micro-crack is considered a single seismic event, then almost all the recorded events would have similar magnitude. This is unrealistic since the seismic magnitude generally follows a power law distribution. Therefore,

when multiple bond breakages occur at a connected time and location, those micro-cracks are identified as part of the same rupturing event. In this case, the centroid of the acoustic emission is its geometric center. For one crack event, the event centroid is simply assumed to be the location of the previously bonded contact. Figure 3.5 shows an example of a seismic event caused by the formation of a tensile crack and its corresponding moment tensor. Then a summation operation is performed over the source surface  $S$  enclosing the event to calculate components of the moment tensor from the force changes and contact locations (Hazzard and Young, 2002):

$$\mathbf{M}_{ij} = \sum_S \Delta F_i R_j \quad (3.24)$$

where  $\Delta F_i$  is the  $i$  th component change in contact force, and  $R_j$  is the  $j$  th component of the distance between the event centroid and the contact point.

### 3.6 Numerical Damping

When a fault ruptures, a stress change is induced near the fault. This stress change results from both transient (dynamic) and permanent (static) stress perturbations. The dynamic stress perturbations are associated with a passage of transient seismic waves (Hill et al., 1993; Brodsky et al., 2000). The dynamic stress perturbations are easier to observe at a seismic station since it has a more extended range interaction with a delay in time. Measuring the static stress perturbation is much more challenging. The static stress perturbation due to the permanent displacement attenuates much faster than the dynamic stress perturbation. Therefore, it is only observable in

the near-field. However, the static and dynamic stress perturbations are difficult to distinguish between in the near field since they co-exist in the same time and space.

In this numerical study, we can control the system’s static and dynamic stress perturbations by adjusting the numerical damping level. Therefore, the static stress perturbations can be isolated by eliminating the dynamic stress perturbation in the system. We can execute static and dynamic failure modes by assigning high and low numerical damping coefficients (Table 3.1), respectively.

In the dynamic mode, the model is run with low damping to mimic a realistic attenuation level resulting from internal friction and wave scattering (Hazzard et al., 2000). Thus, each time a bond breaks, a micro-crack forms. The stored strain energy partially converts to kinetic energy released in the form of seismic waves so that realistic dynamic stress perturbations in natural rocks can be simulated. However, in the static mode, models can run with a high level of numerical damping; the equation of motion is damped heavily to reach a force equilibrium state as quickly as possible. The high numerical damping makes the model absorb and store most of the energy in the bond. Therefore, the seismic waves are mostly eliminated from the static system. The stress perturbation is solely related to the permanent static deformation from a slipping crack.

The magnitude of the damping force  $F^d$  is proportional to the unbalanced force  $F_{net}$  to stabilize particles:

$$F^d = -\alpha|F| \text{sign}(v) \tag{3.25}$$

where  $F^d$  is the fictitious damping force,  $\alpha$  is the damping parameter deter-

mining the damping level,  $\mathbf{f}$  is the magnitude of the unbalanced force and  $\text{sign}(v)$  is the sign (positive or negative) of the velocity of the particle. In natural materials, the internal friction and wave scattering dissipate kinetic energy. A common measure of damping and attenuation is described as the seismic quality factor  $Q$ . The quality factor is defined as  $2\pi$  times the ratio of stored energy to dissipated energy in one wavelength:

$$Q = 2\pi(W/\Delta W), \quad (3.26)$$

where  $W$  is the energy, and  $\Delta W$  is the loss of the energy. For a single degree of freedom system,  $\alpha$  can be expressed in terms of energy loss in one cycle by (Hazzard et al., 2000)

$$4\alpha = \Delta W/W, \quad (3.27)$$

Combining Equation 3.26 and 3.27 yields

$$Q = \pi/2\alpha. \quad (3.28)$$

Mode	Quality Factor $Q$	Damping Coefficient $\alpha$
Static	2.2	0.7
Dynamic	220	0.015

Table 3.1: Numerical damping of static and dynamic mode.

In the following chapters, we will apply the bonded particle method and perform numerical simulations either statically or dynamically to investigate the geomechanical behaviour of brittle rocks.

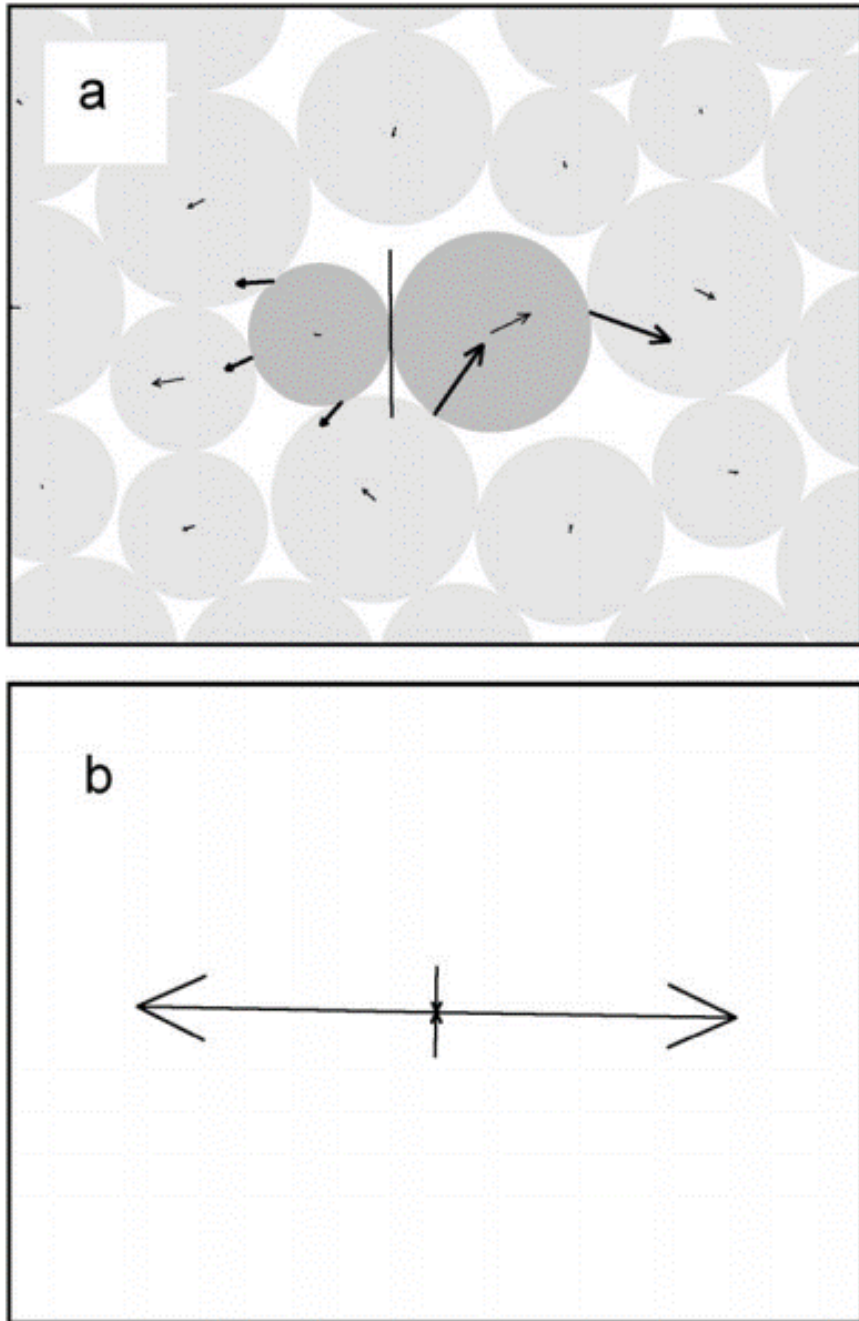


Figure 3.5: An example seismic event caused by formation of a tensile crack. (a) Light arrows represents the particle velocities while the heavy arrows represent the contact force changes after the bond breakage. The sub-vertical black line between the dark grey source particles represents the crack. (b) Its corresponding moment tensor. Reproduced from Hazzard and Young (2002) with permission of Elsevier.

# Chapter 4

## Semi-analytical and Numerical Simulation of Stress

### Summary

I thoroughly discussed the numerical modelling and the bonded particle method in the previous chapter. Before creating the rock specimen and conducting numerical simulations, it is necessary to first verify the bonded particle method. This chapter uses numerical methods and analytical/semi-analytical methods to simulate the elastic wave propagation by exciting a particle with a single point force. The semi-analytical approach is used to verify whether the numerical method is valid and assess how accurate the numerical simulation is in computing displacement and stress fields of microseismicity. The numerical simulation is conducted using a discrete element model based on the bonded particle method, namely PFC, in 2D. The numerical simulation result of that single force excitation is compared with the corresponding semi-analytical result, and an excellent agreement was found between the two.

## 4.1 Introduction

A single point source of force is applied to trigger wave propagation in both the semi-analytical and numerical simulations. First, I will demonstrate how to use the Elasticity Theorem to obtain the displacement field induced by an event source, followed by deriving the stress field by using a semi-analytical approach. I will also demonstrate the numerical simulation procedures to show how to obtain the displacement field and stress field induced by the same source. Finally, I will then compare the simulation results obtained from the two approaches, verify the performance of the numerical simulation, and discuss the characteristics of wave propagation in the discrete element model.

## 4.2 Method

### 4.2.1 Test Setup

In both the semi-analytical and numerical simulations, the tests will take place in a  $200 \text{ mm} \times 200 \text{ mm}$  homogeneous and isotropic medium. The single point force applied for excitation is a pulse defined by a half-period of a  $1000 \text{ kHz}$  sine wave. The direction of force points up in the positive  $y$ -direction at the center of the homogeneous medium (see Figure 4.1).

### 4.2.2 Semi-analytical Approach

The semi-analytical solution of the single point force source will serve as the reference for the numerical simulations. The computation workflow follows the relationship among displacement, strain and stress, as summarized in

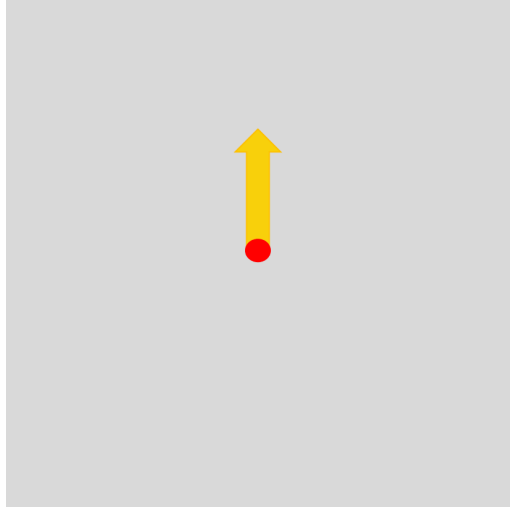


Figure 4.1: Excitation of the single point force and location of the source. The yellow arrow represents the force in the positive y-direction. The red dot represents the source location, where the force acts on. The point force is an impulsive function defined by a half-period of a 1000k Hz sine wave.

Figure 4.2. The computation procedures are generalized into three steps:

1. computation of displacement field  $\mathbf{u}$  resulting from the single point force source that is applied in the positive y-direction
2. computation of strain  $e_{ij}$  based on the displacement.
3. computation of stress  $\sigma_{ij}$  based on the strain.



Figure 4.2: Workflow for obtaining semi-analytical solution of the stress field.

The detailed computation processes will be demonstrated below.

## The Displacement Field

I start with calculating the exact solution of the displacement field  $\mathbf{u}$ . A point force  $F_p$  is applied in the  $p$  direction at the origin of a homogeneous, isotropic and unbounded medium. Aki and Richards (2002) provide an exact analytical 3D solution to such a point source  $\mathbf{u}_n$ , the resulting  $n$  component of displacement  $\mathbf{u}$ , is defined as the convolution of source  $F_p$  and Green's function  $G_{np}$ :

$$\begin{aligned}
 \mathbf{u}_n(\mathbf{x}, t) &= F_p * G_{np} \\
 &= \frac{1}{4\pi\rho} (3\gamma_n\gamma_p - \delta_{np}) \frac{1}{r^3} \int_{\frac{r}{\alpha}}^{\frac{r}{\beta}} \tau F_p(t - \tau) d\tau \\
 &+ \frac{1}{4\pi\rho\alpha^2} (\gamma_n\gamma_p) \frac{1}{r} F_p(t - \frac{r}{\alpha}) \\
 &- \frac{1}{4\pi\rho\beta^2} (\gamma_n\gamma_p - \delta_{np}) \frac{1}{r} F_p(t - \frac{r}{\beta}),
 \end{aligned} \tag{4.1}$$

in which  $\tau$  is the time dummy variable, and  $t$  is time.  $r$  is the source-receiver distance, given by  $r = |\mathbf{x} - \xi|$ .  $\xi$  is the spatial origin which is set to be  $(0, 0, 0)$ .  $\mathbf{x}$  is the 3D location coordinate in vector format.  $\delta_{np}$  is the Kronecker delta function of directions  $n$  and  $p$ , and  $\gamma_i$  is the direction cosine for vector  $\mathbf{x}$ , so that  $\gamma_i = x_i/r$ .  $\alpha$  and  $\beta$  are the P-wave and S-wave velocities respectively,  $\rho$  represents the density of the medium (Table 4.1).

Parameter	Value	Unit
Grain density	3169	$kg/m^3$
P-wave Velocity	5525	m/s
S-wave Velocity	3310	m/s

Table 4.1: Seismic properties of the granite assembly.

The relative magnitude of different terms depends upon the source-receiver distance  $r$ . The first term in Equation 4.1 containing  $r^{-3}$  dominates

as  $r \rightarrow 0$ . Therefore, the first term is called the near-field term. The remaining terms containing  $r^{-1}$  become dominant as  $r \rightarrow \infty$ , and these two terms are named as far-field P and far-field S terms, respectively. Most of the seismic data are collected in the far-field. The near-field effect plays a key role in the final static offset due to faulting at the source location.

The displacement solution derived from Aki and Richards (2002) is in 3D; however, in 2D DEM models, the force transfer in the out-of-plane direction is not considered, neither is the particle movement in the out-of-plane direction. Since the numerical simulation is in 2D, I will simplify the problem by extracting the corresponding 2D plane from the 3D result. The final displacement result is the xy-plane taken from the 3D result at  $z = 0$ . However, differences in magnitude of displacement should be expected due to the limitation of 2D modelling.

## Strain

The strain field contains the spatial derivative of the displacement field. The relationship between the displacement field and strain field is represented by the Geometric Law describing the deformation. For the elastic displacement  $\mathbf{u}(\mathbf{x}, t)$  in a 2D coordinate system with axes  $x$  and  $y$ , the corresponding symmetric strain tensor resulting from  $\mathbf{u}(\mathbf{x}, t)$  is  $e_{ij}$ ,  $ij \in x, y$ :

$$e_{ij} = \frac{1}{2} (u_{i,j} + u_{j,i}), \quad (4.2)$$

where the  $u_{i,j}$ ,  $ij \in x, y$ , represents the partial derivative of Cartesian component  $u_i$  with respect to  $j$ . In matrix form it is expressed as:

$$e_{ij} = \begin{pmatrix} e_{xx} & e_{xy} \\ e_{yx} & e_{yy} \end{pmatrix}. \quad (4.3)$$

Then, using 4.2, every strain tensor component becomes:

$$\begin{aligned} e_{xx} &= u_{x,x}, \\ e_{yy} &= u_{y,y}, \\ e_{xy} &= \frac{1}{2}(u_{x,y} + u_{y,x}), \\ e_{yx} &= \frac{1}{2}(u_{y,x} + u_{x,y}). \end{aligned} \quad (4.4)$$

And the strain tensor is reformatted to:

$$e_{ij} = \begin{pmatrix} u_{x,x} & \frac{1}{2}(u_{x,y} + u_{y,x}) \\ \frac{1}{2}(u_{y,x} + u_{x,y}) & u_{y,y} \end{pmatrix}. \quad (4.5)$$

Due to the complexity of the original displacement function, solving the partial differential equation in the analytical form is cumbersome. Therefore, we use a semi-analytical solution technique for solving the strain tensor component involving partial derivatives. Solving this semi-analytical solution involves the following steps: 1) discretizing the spatial domain; 2) decomposing the displacement field into  $u_x$  and  $u_y$ ; 3) computing the second order derivatives  $u_{x,x}$ ,  $u_{y,y}$ ,  $u_{x,y}$  and  $u_{y,x}$ , the directional gradient of the  $u_x$  and the  $u_y$  with respect to either the  $x$  or the  $y$  directions using the forward derivatives. These second order derivatives are calculated by using the forward difference method:

$$f'(x, y) = \frac{f(x + h, y) - f(x, y)}{h}, \quad (4.6)$$

where the  $f$  is the first derivative  $u_x$  or  $u_y$ ,  $h$  is the x- or y-increment.

The strain tensor  $e_{ij}$  will then be used in the next step to obtain each stress tensor  $\sigma_{ij}$ .

## Stress

The Elastic Constitutive Law describes the relationship between strain and stress in isotropic media. It represents the material properties, including material strength and stiffness. In our case of 2D plane stress, i.e, there is no force and stress exerted in the z-direction, the stress tensor can be expressed as  $\sigma_{ij}$ ,  $ij \in x, y$ :

$$\sigma_{ij} = \lambda e_{kk} \delta_{ij} + 2\mu e_{ij}. \quad (4.7)$$

The two constant components  $\lambda$  and  $\mu$  are the Lamé parameters.  $e_{kk}$  is the volumetric strain, also called the dilation. It is measured as the change in volume per unit volume associated with the deformation. The dilatation  $e_{kk}$  is given by the sum of extension or contraction in each of the x and y directions:

$$\frac{\Delta V}{V} = e_{kk} = u_{x,x} + u_{y,y}. \quad (4.8)$$

By inserting the 4.8 into 4.7, every stress tensor component is obtained:

$$\begin{aligned} \sigma_{xx} &= (\lambda + 2\mu)u_{x,x} + \lambda u_{y,y}, \\ \sigma_{yy} &= (\lambda + 2\mu)u_{y,y} + \lambda u_{x,x}, \\ \sigma_{yx} &= \sigma_{xy} = 2\mu u_{y,x}. \end{aligned} \quad (4.9)$$

and therefore, the stress tensor can be reformatted to:

$$\begin{aligned}\sigma_{ij} &= \begin{pmatrix} \sigma_{xx} & \sigma_{xy} \\ \sigma_{yx} & \sigma_{yy} \end{pmatrix} \\ &= \begin{pmatrix} (\lambda + 2\mu)u_{x,x} + \lambda u_{y,y} & 2\mu u_{y,x} \\ 2\mu u_{y,x} & (\lambda + 2\mu)u_{y,y} + \lambda u_{x,x} \end{pmatrix}\end{aligned}\tag{4.10}$$

The stress fields are directly computed based on the numerical values in the displacement field using the forward difference approximation. Therefore, the stress field computed here is a semi-analytical solution.

### 4.2.3 Numerical Approach

Same as the semi-analytical approach, a half-period of a 1000k Hz sine wave will be applied as the single point force for excitation. The single point force points in the positive y-direction and originates from the center of the experiment area. The first step is to construct the Lac du Bonnet granite specimen. There are two distinct regions, which are the inner observation region and the outer damping region (Figure 4.3). The total dimension of the granite assembly is 300 mm \* 300 mm. The thickness of the damping region is 50 mm, so the observation region's dimension is 200 mm \* 200 mm. The damping region is set up to eliminate the influence of energy and wave reflecting back from the boundaries. For numerical simulations, the Particle Flow Code applies the force-displacement law and law of motion to solve the wave propagation induced by the single point force (see chapter 3 for details). The resultant displacement and stress fields will be analyzed.

The first step of the numerical simulation is to generate particles within the 300 mm \* 300 mm box to achieve this model setup. There are approxi-

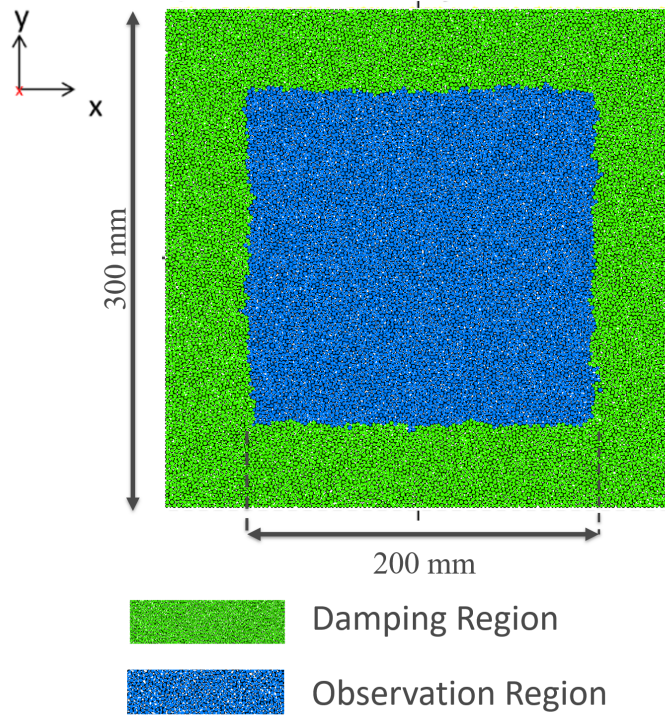


Figure 4.3: Model setup of assembly. The inner square represents the observation region assigned with a realistic low damping parameter. The outer square ring represents the damping region assigned with a high damping parameter to absorb energy reflected from boundaries.

mately 18000 grains, and the grain radii are randomly distributed between 1 mm and 1.5 mm. Then, different damping parameters  $\alpha$  are assigned to both regions. A higher damping parameter  $\alpha$  indicates higher energy loss due to the damping. A much higher damping parameter, 0.7, is assigned to the damping region, while a realistic damping parameter of Lac du Bonnet granite based on lab measurements, 0.0157, is assigned to the observation region instead.

Following the material genesis procedures described in Chapter 3, I create the square granite assembly with specified damping. The micro-properties of the granite particles and the bonds are listed in Table 4.2.

Except for the damping parameter, the properties of the material in the observation region and damping region are kept the same.

Parameter	Value	Unit
Grain density	3169	$kg/m^3$
Minimum grain size (radius)	2	mm
$R_{max}/R_{min}$ grain size ratio	1.5	N/A
Friction coefficient	0.5	N/A
Parallel bond Young's modulus	65	GPa
Stiffness ratio for parallel bond	2.5	N/A

Table 4.2: Micro-properties of granite assembly

In PFC2D, the displacement of each particle can be directly computed at the end of the calculations cycle, but the stress data can not be directly obtained. However, we can obtain the corresponding high-resolution stress map by utilizing a "measurement region." Measurement regions return average values computed over objects in the measurement region. The quantities available for measurement include but are not limited to stress. Each measurement region is created with the same radius of the corresponding particle at the same position. Therefore, every particle in the assembly has one stress measurement, and the stress measurements of all the particles will make up a high-resolution numerical stress field. Then, the numerical stress field will be compared with the semi-analytical stress field.

## 4.3 Result

### 4.3.1 Displacement field

For a force applied in the positive y-direction at the center, Figure 4.4 shows the different displacement components derived from the first term, second term, and third term of Equation 4.1, respectively. By decomposing

the displacement vectors along the x and y axes, we can obtain the x-components (first column) and y-components (second column), respectively, for the total displacement field and the displacement of the near-field wave, far-field P wave and far-field S.

For the x-components (first column), all the terms have a circular pattern splitting into four lobes with an alternating sign within four quadrants, and  $y = x$  and  $y = -x$  are the two axes of symmetry. The near-field and far-P wave terms have the same polarities, but the far-S wave terms have opposite polarities with the other. The entire x-component displacement field is simply the summation of three displacement field components. It appears to have two layers of distinct circular patterns. This is because the far-S wave travels slower than the others and leads to the formation of the inner circle. For the y-components (second column), the axes of symmetry of the y-components are the x and y axes. Instead of having alternating patterns within four quadrants, the entire y-component displacement field is dominated by the positive y-displacement. The positive displacement appears to be more diffusive at the top and bottom but more concentrated as two crescents at the sides. The corresponding far-field P and S displacement fields are compared with the Aki and Richard's solution (Figure 4.5 and 4.6), which show the radiation patterns of the far-field P wave and S wave. Our analytical results are consistent with their solutions in terms of amplitude and direction.

For the validation test, an identical single point force is applied to the center of the numerical model. For numerical simulations, the observation is the total field, the summation of all the wave fields. Figure 4.7 shows the entire displacement fields obtained by the numerical (first column) and

analytical methods (second column). The analytical solution provides the theoretical result by assuming the medium is perfectly isotropic and homogeneous; however, PFC2D tries to replicate the real rock specimen, which is naturally flawed and heterogeneous and leads to a lower resolution. The order of magnitude of results obtained from two approaches are different, and it could be caused by two reasons: 1. PFC2D is a idealized 2D model while the analytical solution is 3D-based. 2. Dissipation of energy in PFC2D's granular system. Generally, the results simulated by PFC2D are very similar to the analytic solutions in the polarity and patterns.

The excitation force applied at the center in the positive y-direction pushes out the top region from the center and pulls in the bottom region to the center. This point force deforms the surrounding region with permanent deformation, represented by the near field term. Both x and y components show that the P-wave propagates faster than the S-wave, but the latter has a more substantial magnitude. The P wave component pushes the top region and pulls the bottom region. Therefore it facilitates the compression at the top and dilation at the bottom. Thus, the P wave creates the alternating pattern of x-displacement due to the point force source originating from the center and two strong positive crescent-like patterns at the top and bottom of the y-displacement. In an S wave, particles slide past one another and undergo shearing along with force. Therefore, shearing motion wraps the source and moves in the same direction as the point force. The shearing around the source creates the alternating pattern of x-displacement and two strong crescent-like patterns of y-displacement at the two sides.

### 4.3.2 Stress field

In Figure 4.8, different stress fields are shown on rows, in order, displaying the total stress field, the stress of the near-field wave, far-field P wave and far-field S wave. The columns display the horizontal  $\sigma_{xx}$ , vertical  $\sigma_{yy}$ , and shear  $\sigma_{yx}$  components of the stress fields. Stress fields are composed of multiple layers of alternating lobes due to the second order forward differentiation involved in the computation processes of stress. For horizontal  $\sigma_{xx}$  and vertical  $\sigma_{yy}$  stress fields, the axis of symmetry is the y-axis. They are also symmetric about the x-axis in terms of the pattern but with the opposite sign. For shear  $\sigma_{yx}$  stress field, the axis of symmetry is the y-axis, and they are also symmetric about the y-axis, but values have the opposite sign. Like the displacement field, the far-field S displacement is more dominant than the near-field and far-field P displacement components. The total stress field is the summation of the three displacement fields.

Comparing the semi-analytical with the numerical results (Figure 4.9) for validation purposes, all the stress field are more disordered compared with the displacement field with a persistent irregular pattern, particularly at the central regions, in the numerical simulations. The irregularities are created by wave scattering due to the random packing of the bonded particles. In general, the numerical PFC results of the stress fields agree with the semi-analytical results in terms of pattern, polarity and symmetry. Figure 4.9 shows the horizontal  $\sigma_{xx}$  and vertical  $\sigma_{yy}$  components have two stronger inner loops splitting into four quadrants with opposite polarities. The stronger inner loops are wrapped by weaker outer loops. The shear stress  $\sigma_{yx}$  also has two stronger inner loops and two weaker outer loops with opposite signs, but instead of splitting into four quadrants, four loops

split two portions placed at the sides with alternating signs.

## 4.4 Discussion

The analytical solution of displacement and semi-analytical solution of stress is based on the assumption of a homogeneous, isotropic and elastic medium. Nevertheless, in numerical simulations with PFC, we have an inhomogeneous and damped system consisting of individual grains connected by cement. So noticeable differences between these two solutions should be expected.

For the displacement field, as the two solutions are shown at the same time and space instance (Figure 4.7), the major difference is the magnitude of displacement in the two results. The magnitude of displacement in PFC simulations is smaller than the analytical results due to the damping of the numerical system. We see some irregularities resulting from the irregular wave scattering in the central region. Despite these two points, the PFC results show a remarkable degree of matching with the analytic solutions.

The stress field is more complex than the displacement field. The semi-analytical solutions and PFC simulation of the stress field show similar results in terms of patterns and polarity of stress (Figure 4.9). However, the irregularities at the central region is much more significant than that observed in the numerical simulation. The irregularities mainly affect the innermost loop clearly visible in the semi-analytical solutions. The irregularities in the stress field results from discretized grains, leading to wave scattering and stress heterogeneity in the central region after waves pass through.

## 4.5 Conclusion

The agreement between semi-analytical and numerical simulation of the displacement field and the stress field verifies that the bonded-particle methods can reliably generate the displacement and stress responses comparable to analytical and semi-analytical solutions. This verification provides us with a good starting point to investigate in detail the influence of force and stress on rock failures.

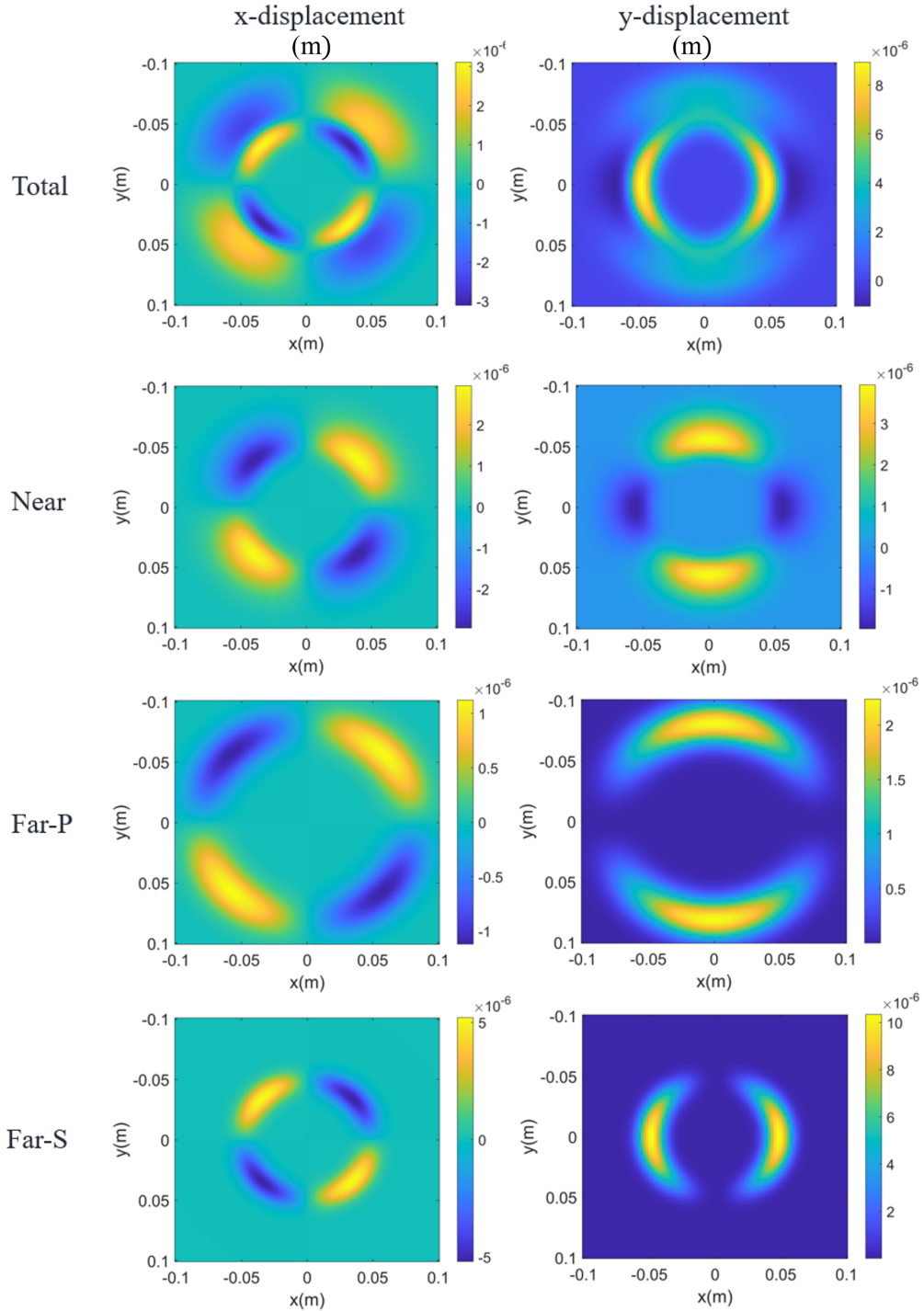


Figure 4.4: Analytical solution of displacement field results in unit of  $m$ . From top to bottom, it shows the complete, near-field, far-field P, and far-field S displacement fields at the time of  $1e-5$  sec. The left column shows the x-displacement, and right column shows the y-displacement.

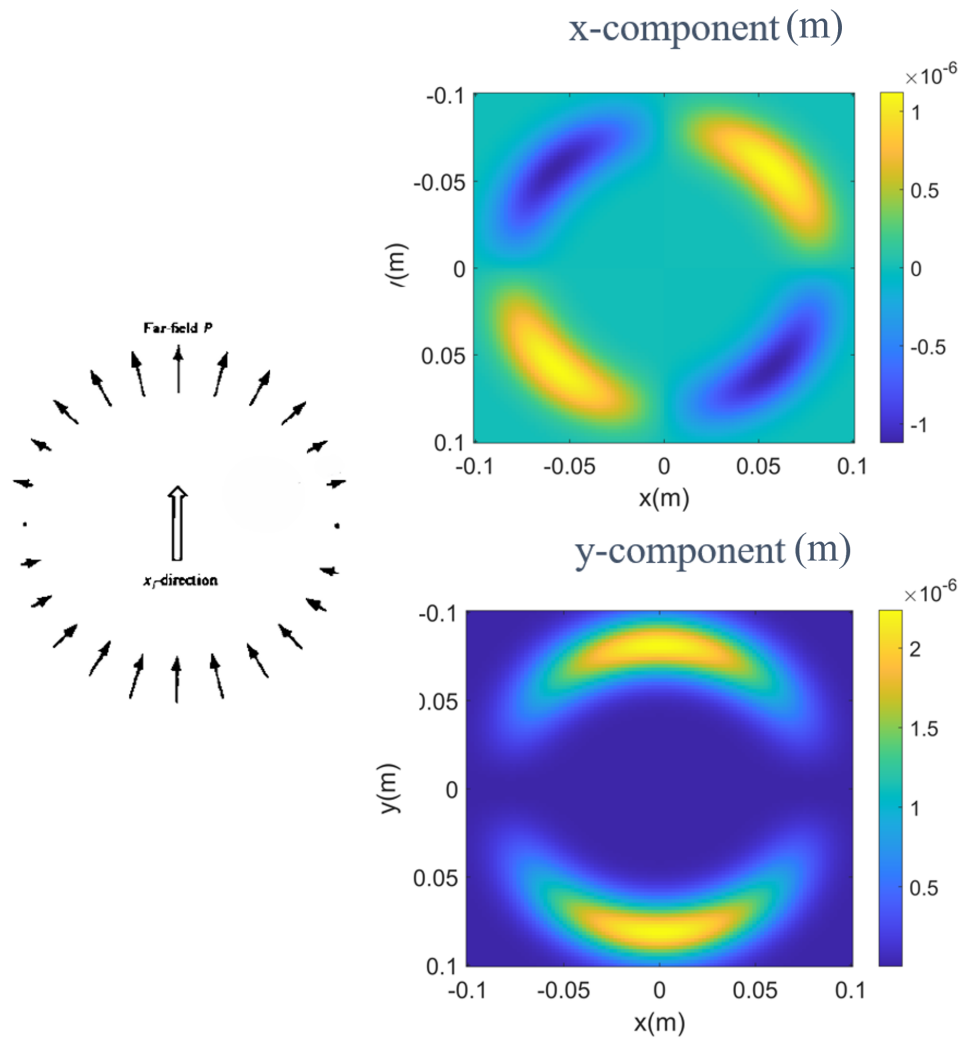


Figure 4.5: Comparison of far-field P displacement field results in unit of  $m$ . The results on the left is the far-field P result from Aki and Richards (2002). On the right is our analytical far-field P displacement field obtained and decomposed into x- (top left) and y-directions (bottom left).

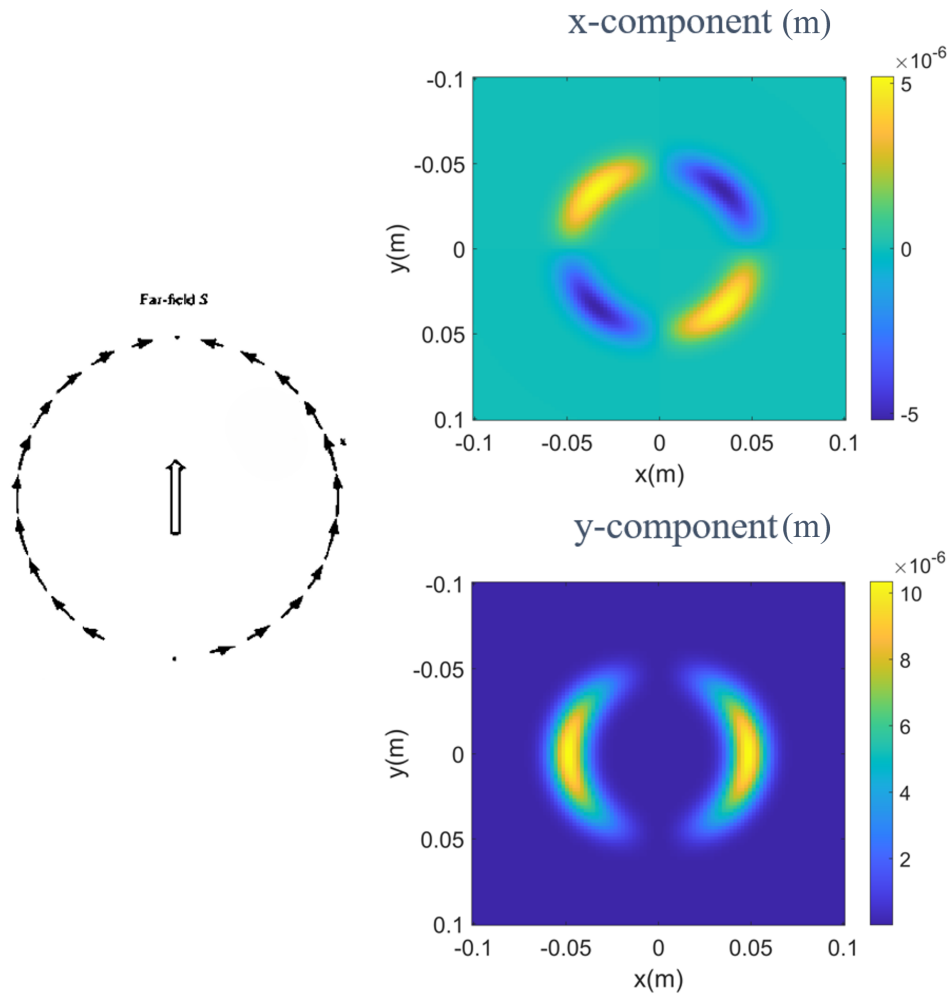


Figure 4.6: Comparison of far-field S displacement field results in unit of  $m$ . The results on the left is the far-field S result from Aki and Richards (2002). On the right is our analytical far-field S displacement field obtained and decomposed into x- (top left) and y-directions (bottom left).

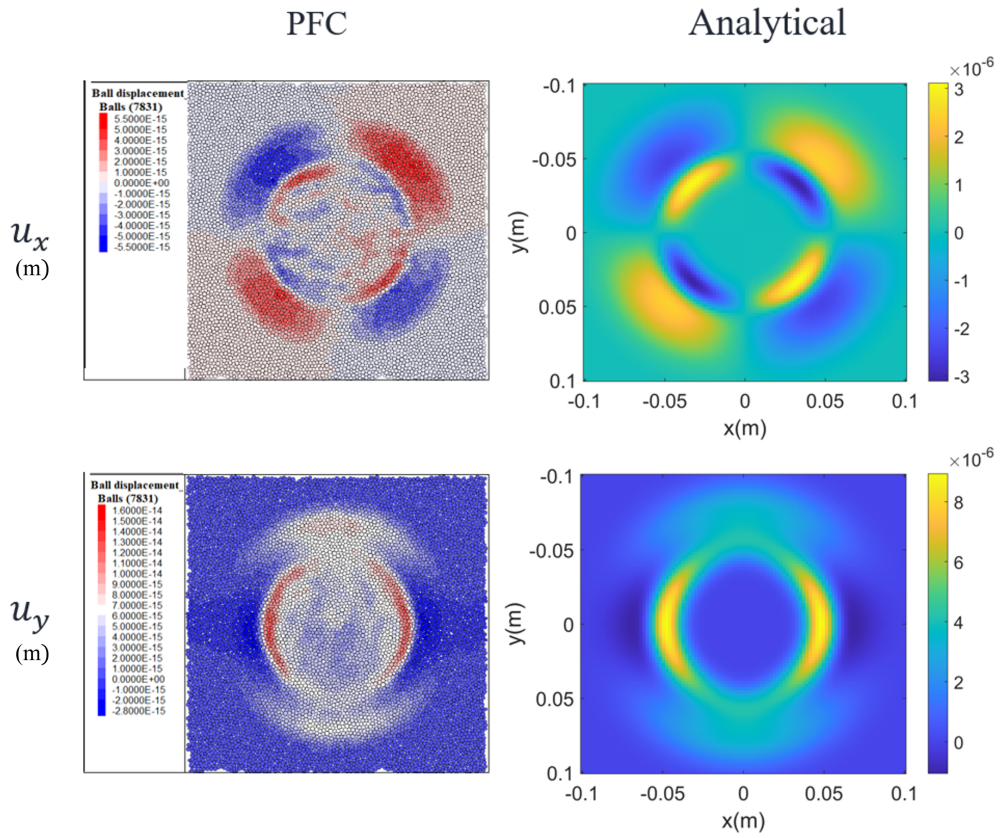


Figure 4.7: Comparison of the complete displacement fields of the analytical and numerical simulations at the time of  $1e-5$  sec in unit of  $m$ . The top row represents the x-component of the complete displacement field, and the bottom row represents for the y-component. The results on the left are the numerical results from PFC2D. The results on the left are the analytical solutions.

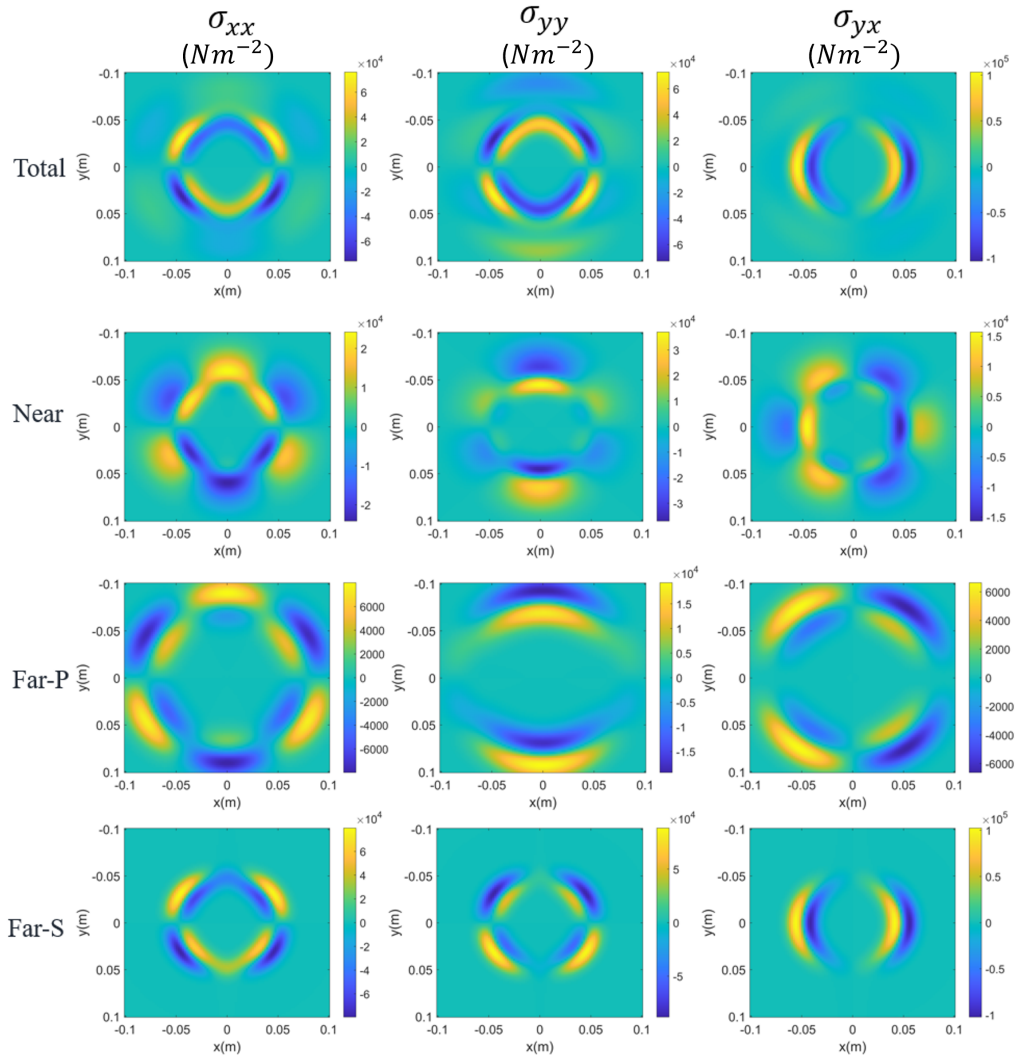


Figure 4.8: Semi-analytical solution of stress in unit of  $Nm^{-2}$ . From top to bottom, it shows the complete, near-field, far-field P, and far-field S stress fields at the time of  $1e-5$  sec. From left to right, each column shows the  $\sigma_{xx}$  component,  $\sigma_{yy}$  component,  $\sigma_{yx}$  component of stress, respectively.

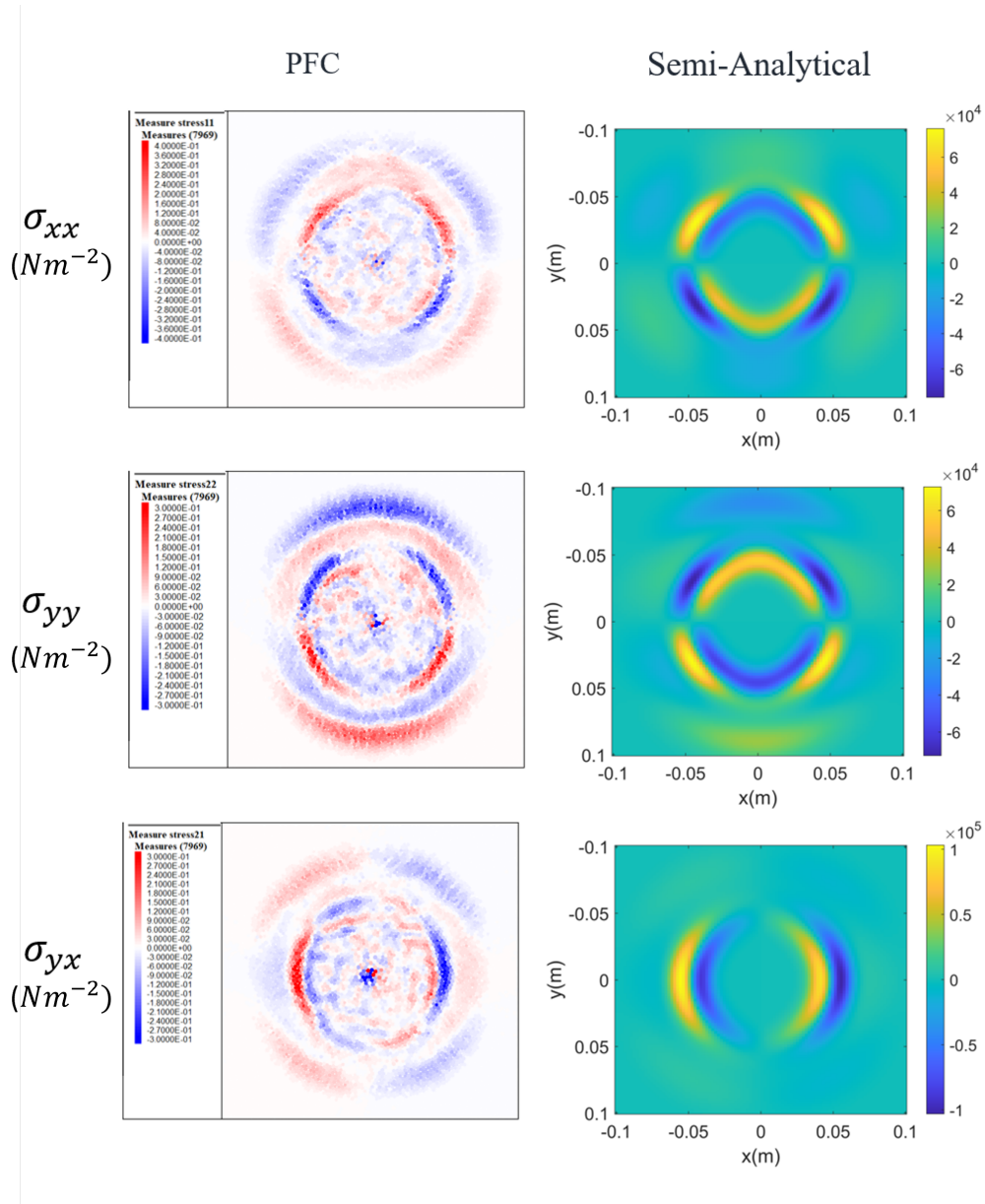


Figure 4.9: Comparison of the complete stress fields of the semi-analytical and numerical simulations at the time of  $1e-5$  sec in unit of  $Nm^{-2}$ . The top row represents the x-component of the complete stress field, and the bottom row represents the y-component. The results on the left are the numerical results from PFC2D. The results on the left are the semi-analytical solutions.

# Chapter 5

## Material-genesis and Calibration of the Bonded Particle Models

### 5.1 Introduction

In this chapter, we will utilize the bonded particle method to prepare a PFC2D model of Lac du Bonnet granite, followed by a discussion of the calibration and general characteristics of the granite model. The main objectives of this chapter are to describe the material genesis procedures and calibrate the model for the following simulations.

### 5.2 Procedures of Material Genesis

The material genesis procedure is defined in Cundall and Strack (1979a) and extended in Potyondy (2014). The procedures occur within a material vessel and produce a rock specimen consisting of a well-connected grain assembly

with a specified non-zero material pressure. The geomechanical behaviour of the Lac du Bonnet granite has been studied extensively in the laboratory and field (Martin, 1993) as well as in numerical simulations (Potyondy et al., 1996; Al-Busaidi et al., 2005; Hazzard et al., 2000). Therefore, the Lac du Bonnet Granite is chosen to be modelled for this study.

In our experiment, a 25.2 \* 63 cm sample (Figure 5.1) of Lac du Bonnet granite consists of particles that are drawn from a uniform size distribution with radii ranging from 2 to 3 mm. This sample size is commonly used in the mechanical experiments conducted by Atomic Energy of Canada Limited in their studies of Lac du Bonnet (Hazzard et al., 2000). The particle size is chosen to be approximately comparable to the size of the actual mineral grains of the Lac du Bonnet granite (Kelly et al., 1993).

### **5.2.1 Step 1 Compact initial assembly**

Material genesis occurs within a material vessel, which is a rectangle bounded by four planar frictionless walls for PFC2D (Figure 5.1). The wall normal stiffnesses are set just higher than the average particle normal stiffness to ensure that the particle-wall overlap remains small.

The first step is compacting the initial assembly. The packing is achieved by a grain-scaling method. The grain-scaling procedure produces a dense packing of a granular material that will subsequently become a bonded material. Grains are created within the material vessel. The number of particles is determined such that the overall porosity, the proportion of void spaces, of the PFC2D model is 16% (Cundall and Strack, 1979a). The particle radii satisfy a uniform size distribution bounded by  $R_{min} = 2mm$  and  $R_{max} = 3mm$ . The particles are arbitrarily placed to fill the vessel

such that they may have grain-grain overlaps and large internal stresses. In order to eliminate the large grain overlaps, and to provide an isotropic and dense-packed state, the material friction coefficient remains equal to zero throughout the entire packing process. The friction-less system will allow the grains to rearrange the positions liberally until either static-equilibrium is obtained or the mean stress is near zero. The mean stress for the 2D model is defined as the average of the in-plane stresses. These stresses are measured by dividing the average of the total force acting on opposing walls by the area of the corresponding specimen cross-section. Stresses in the PFC2D models are computed, assuming that each particle is a disk of unit thickness.

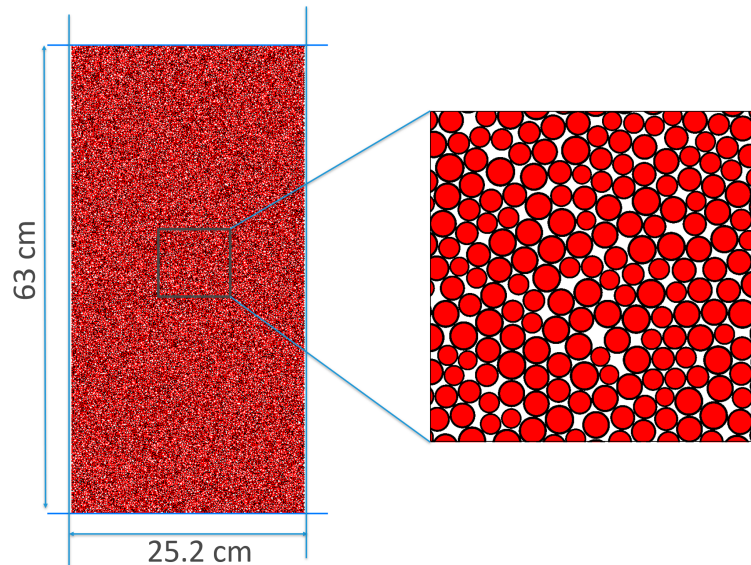


Figure 5.1: PFC2D model of 25.2 cm x 63 cm Lac du Bonnet granite and the distribution of grains. The material vessels are indicated by the four blue lines surrounding the granite.

### **5.2.2 Step 2 Install specified material pressure**

Then, the radii of all particles are re-scaled iteratively until the measured mean stress achieves the target material pressure, and static equilibrium is obtained (Itasca Consulting Group, 2008). The material pressure is typically set to a low value for a bonded material relative to the material strength. To install the specified material pressure, the mean stress is set equal to approximately 1% of the uniaxial compressive strength (Cundall and Strack, 1979a) of the granite to achieve a low material pressure. This step helps to reduce the magnitude of the locked-in forces in the rock. The locked-in forces are the residual force within an object, even though the object is free of external forces. Without installing the material initial pressure, locked-in forces will significantly develop after the parallel bond installation in the next step. The locked-in forces also occur and develop when the specimen model is removed from the material vessel and relaxed. These locked-in forces can significantly affect the internal stress distribution and interrupt the following simulations of rock behaviour.

### **5.2.3 Step 3 Reduce the floating particles**

In an assembly of non-uniform-sized circular particles, typically 10% to 15% of the total number of particles could be floating particles (Cundall and Strack, 1979a). Floating particles have less than three contacts in an assembly of randomly placed particles with a non-uniform radius. We wish to obtain a densely packed and well-connected assembly to mimic granite with highly interlocked grains and fewer voids in our granite models. Therefore, it is necessary to have fewer floating particles so that the assembly will achieve a denser network of bonds in the next bond installation step.

The elimination procedures are described as follows. We first identify all the floaters that have less than three contacts. Next, all the particles except the identified floaters are fixed, and then the floaters are expanded by a sufficient amount (30%) so that they have contacts with all of their neighbouring particles. Then, the size of the floaters is reduced until the mean contact normal force is small enough (one-tenth of the mean contact normal force of assembly). The floaters will be reduced considerably after executing expansions and contractions iteratively on every particle.

However, if there are still many floaters in the specimen, the elimination procedures can be repeated a few more times for a better elimination result. We obtain a bonded assembly for which nearly all particles away from the specimen boundaries have at least three contacts.

#### **5.2.4 Step 4 Install parallel bonds and assign micro-properties**

During this process, parallel bonds are installed between grains close to each other throughout the assembly. The micro-properties of parallel bonded material will be assigned to the grain-grain contacts. The installation of parallel bonds obeys the general rule on the installation gap. That is, only those grain-grain contacts with a gap less than or equal to the specified installation gap are bonded. Increasing the installation gap indicates more qualified grain-grain contacts. In our simulations, we set the installation gap to be  $10^{-6}$  times the mean radius of the two-grain particles (Cundall and Strack, 1979a) to ensure the particles that have parallel bonds installed are nearby. The parallel bonds are installed, and it is the only time that the parallel bonds installed (see Chapter 3 for more detail on installation

of parallel bonds).

### **5.2.5 Step 5 Remove the specimen from the material vessel**

The material genesis is completed by removing the specimen from the material vessel and allowing the assembly to relax. This is done by deleting the vessel walls and calming the specimen. During this relaxation process, the specimen expands, releases internal stresses, and generates a set of self-equilibrating locked-in forces similar to those in a free specimen of bonded rock. Finally, the assembly is ready for calibration.

## **5.3 Calibration of Lac du Bonnet BPM Model**

After the material genesis is complete, appropriate micro-parameters need to be determined. The micro-parameters govern the mechanical responses of a bonded particle model. Selecting the optimal micro-parameters to achieve the desired macroscopic mechanical response is not intuitive. No model is complete or fully verifiable, but the model's validity is demonstrated by comparing model behaviour with measured and observed responses of Lac du Bonnet granite at the laboratory. Therefore, the micro-parameters have to be adjusted so that the model matches experimental macro properties, including Young's Modulus, unconfined compressive strength (UCS), Poisson's ratio, cohesion and frictional angle.

### 5.3.1 Young's Modulus, unconfined compressive strength and poisson's ratio

First, the technique is to conduct uniaxial tests to match the sample's Young's modulus, compressive strength and Poisson's ratio. The micro-properties are adjusted in such a way that they generate desired macroproperties. The final adjusted micro-properties are listed in Table 5.1. The microproperties are the small-scale, inherent characteristics of materials that govern their interactions and behavior at the particle level.  $\rho$  represents the density to describe the particle packing.  $R_{max}$  and  $R_{min}$  are the minimum and maximum particle sizes. Existing research shows that the size dependence (specimen size/particle size) has a small influence on a Discrete Element Model specimen if the ratio is sufficiently large (Yang et al., 2006; Fakhimi and Villegas, 2007). The default parallel bond radius multiplier  $\bar{\lambda}$  is set to be 1, which simply means that the parallel bond fills the gap between the two particles.  $E_c$  and  $\bar{E}_c$  are Young's moduli of the grains and cement, respectively.  $k_n/k_s$  and  $\bar{k}^n/\bar{k}^s$  are the ratios of normal to shear stiffness of the grains and cement, respectively. In most simulations, Young's moduli and the ratios of normal to shear stiffness for both the particles and the cement are set to be the same value to reduce the number of free parameters (Cundall and Strack, 1979a; Yang et al., 2006).  $\mu$  is the friction coefficient of the grain. Due to the complex mechanics involved in simulations, a friction coefficient of 0.5 is recommended as a reasonable value for the simulation of a bonded particle model (Cundall and Strack, 1979a).  $\bar{\sigma}_c$  and  $\bar{\tau}_c$  are the tensile and shear strength of the cement, respectively. In PFC modelling, the shear strength is set to cohesion. In soil mechanics, cohesion is equivalent to the shear strength when the

compressive stresses are equal to zero (Yokoi, 1968).

Grains	Cement
$R_{max} = 3 \text{ mm}$	
$R_{min} = 2 \text{ mm}$	$\bar{\lambda} = 1$
$E_c = 60 \text{ GPa}$	$\bar{E}_c = 60 \text{ GPa}$
$k_n/k_s = 2.5$	$\bar{k}^n/\bar{k}^s = 2.5$
$\mu = 0.5$	$\bar{\sigma}_c = 200 \text{ MPa}$
$\rho = 2630 \text{ kg/m}^3$	$\bar{\tau}_c = 220 \text{ MPa}$

Table 5.1: Micro properties used to calibrate the Lac du Bonnet granite model, where  $R_{max}$  and  $R_{min}$  are the minimum and maximum particle radius;  $\bar{\lambda}$  is the radius multiplier;  $E_c$  and  $\bar{E}_c$  are the Young's moduli of the grains and cement;  $k_n/k_s$  and  $\bar{k}^n/\bar{k}^s$  are the ratios of normal to shear stiffness of the grains and cement;  $\mu$  is the friction coefficient of the grain;  $\rho$  represents the density;  $\bar{\sigma}_c$  and  $\bar{\tau}_c$  are the tensile and shear strength of the cement, respectively.

The Young's modulus and unconfined compressive strength are calibrated to match the laboratory parameters conducted by Martin (1993), which is  $E = 69 \text{ GPa}$  and  $\sigma_c = 205 \text{ MPa}$  (Figure 5.2(b)). After several uniaxial tests, while tweaking various micro parameters listed in Table 5.1, the sample is calibrated to a peak stress of 189.0 MPa, Young's modulus  $E = 68.6 \text{ GPa}$ . The poisson's ratio is  $\nu = 0.27$  which is well matched with the Lac du Bonnet granite poisson's ratio from the published literature (Stone et al., 1989; Read and Martin, 1996).

Figure 5.2 shows the stress-strain curve from the unconfined uniaxial test. The shapes of the curves are very similar, and the strength and stiffness of the Lac du Bonnet granite are approximately reproduced. The curve shows elastic deformation of the sample until abrupt brittle failure occurs as the axial stress rapidly drops. The elastic regime of the curve is very stiff, showing minimal hardening at the beginning of the simulation.

The most apparent difference between the model and rock response is the lack of initial curvature observed during the laboratory tests at low-stress levels. This curvature is absent from the model response because the numerical model is intact and has no pre-existing cracks (Hazzard et al., 2000; Zhang et al., 2019). On the other hand, the voids and cracks in the natural rock specimen lead to the formation of the initial curvature. Secondly, no post-peak information was recorded due to the sample failure’s explosive nature in the laboratory tests. Therefore, comparisons cannot be made with the model results over the post-peak part of the stress-strain curve. However, in the numerical simulations, we observe a dramatic strength reduction and crack number surge observed in the model curve (Figure 5.2(a)) after the peak stress, indicating brittle explosive failure.

### **5.3.2 Failure Criterion, Cohesion and Frictional Angle**

Four additional biaxial compressive tests under different confining conditions are conducted. The Mohr failure criterion is determined by experimental data rather than theoretical calculations. Using the experimental data, we can investigate the effect of confining pressure on rock behaviour, construct the Mohr circles, and assess the calibrated model’s failure criterion. Cohesion and internal friction angle are the macro-properties obtained from the failure criterion. In the next chapter, they are particularly useful for model verification and provide supportive information for future failure and force distribution analysis.

Including the unconfined compressive test, we obtain five datasets from five compressive tests for the PFC2D Lac du Bonnet granite model. The

confining pressures are 0, 10, 20, 30, and 60 MPa. The confining pressure is the pressure exerted on the sidewalls of the vessel. Loadings are exerted by the top and bottom platens' incremental movement while keeping the confining pressure constant during the experiment. Both platens move at a constant strain rate (the time rate of change of the rock-vessel length) of  $0.002 \text{ s}^{-1}$ . The strain rate would have a minor effect on the modelled sample as long as it is slow enough that no transient waves are being produced (Hazzard et al., 2000). The stress-strain response history was recorded during the tests (Figure 5.3). The wedges at the bottom of the curves represent the preparation stage for the biaxial tests, and the cut-off points are the corresponding confining pressures. The wedges exist because the model will be compressed first, and once the model achieves the desired confining pressure, the strain deformation will be reset to zero. In Figure 5.3, deviations from the ideally linear elastic behaviour can be seen in the stress-strain curves, and the effect is more obvious at higher confinements. The stress-strain curve becomes nonlinear when the stress is beyond the material's yield point. Plastic deformation induced by the stress will be stored in the material until a localized failure occurs to release the energy. Also, a higher axial loading is required to deform the rock and make it fail as the confining pressure increases. It implies that the strength of the model increases with the confining pressure. Moreover, for Young's modulus, the slope of the stress-strain curve, no clear tendency on slope change can be detected when comparing the slopes at different confining pressure. Therefore, the Young's modulus is found to be unchanged with increasing confining pressure. These findings are consistent with the laboratory experiment (Hokka et al., 2016) and numerical simulation on granite

rocks (Cundall and Strack, 1979a; Hazzard et al., 2000).

For biaxial compressive tests, the compressive rock strength (the peak stress along the axial loading direction at failure) is the first principal stress  $\sigma_1$ ; the confining pressure is the second and third principal stresses  $\sigma_3 = \sigma_2$ . From these five compressive tests (Table 5.2), the Mohr circles and the failure criterion of the granite model is constructed (Figure 5.4). The Mohr-Coulomb criterion is the best-known method to describe intact rock failure (Byerlee, 1978; Al-Ajmi and Zimmerman, 2006). It is based on the relationship between shear stress and normal stress acting on the failure plane. The Mohr-Coulomb failure envelope has a relatively curved shape, but it is usually normalized on the linear equation:

$$\sigma_s = \sigma_n \tan \phi + c_0, \quad (5.1)$$

where  $\sigma_s$  is shear strength,  $c_0$  is cohesion,  $\phi$  is the angle of internal friction, and  $\sigma_n$  is the normal stress on the failure envelope.

$\sigma_3$ (MPa)	$\sigma_1$ (MPa)
0	189.0
10	236.1
20	292.8
30	310.2
60	372.2

Table 5.2: Failure compressive strength  $\sigma_1$  for Lac du Bonnet granite model under different confining pressure  $\sigma_3$  .

In our research, only low confining pressure conditions (10 MPa) are involved. Therefore, the linearized Mohr-Coulomb criterion (Figure 5.4) will be adequate for predicting the failure condition of brittle rocks involving

low confining pressure. Based on the equation 5.1, we can find the cohesion  $c = 40MPa$ , internal angle of friction in the numerical model is  $39.6^\circ$ , and therefore the coefficient of friction is 0.83 (Figure 5.4), and these values are consistent with laboratory measurements (Wyllie, 2017). Similar to the other laboratory tests, a nonlinearity is observed in the granite model under high confining pressure (Murrell, 1965; Hobbs, 1966; Patton et al., 1966; Byerlee, 1967; Engelder and Marshak, 1988). It occurs in the intact rocks under high confining pressure (Barton, 1976) and even low confining pressure Mogi (1974) if the rock is weak.

## 5.4 Conclusion

Based on the numerical simulation results, we found that the compressive rock strength increases with confining pressure while the Young's modulus remains the same. Laboratory experiment results were used to verify the calibration method. The micromechanical parameters of Lac du Bonnet granite were calibrated, and we found that the macroscopic parameters of the calibrated numerical model are similar to the laboratory sample. The results show that the calibrated model is reliable. In future simulation and analysis, this calibrated specimen of intact Lac du Bonnet granite will be used in the final numerical model.

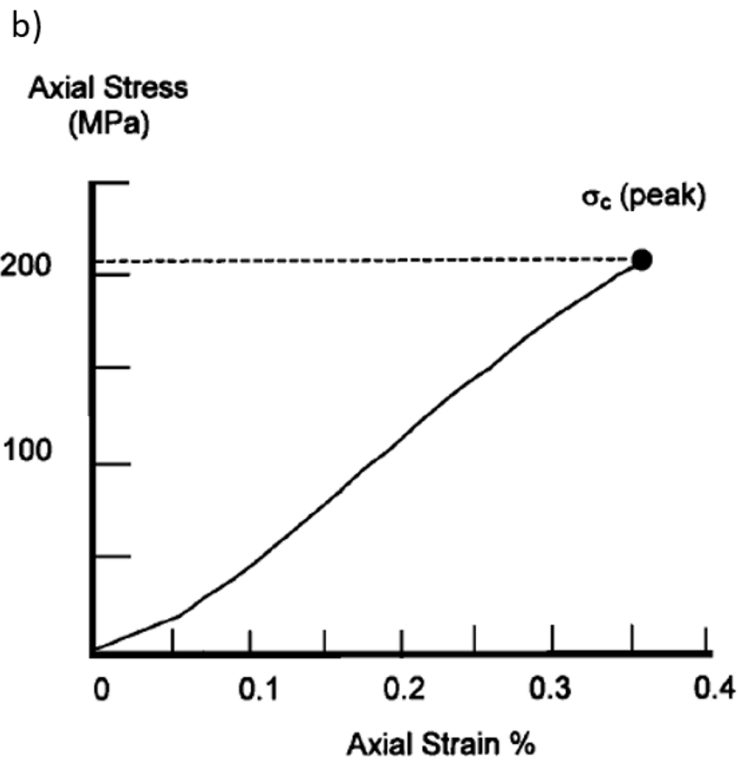
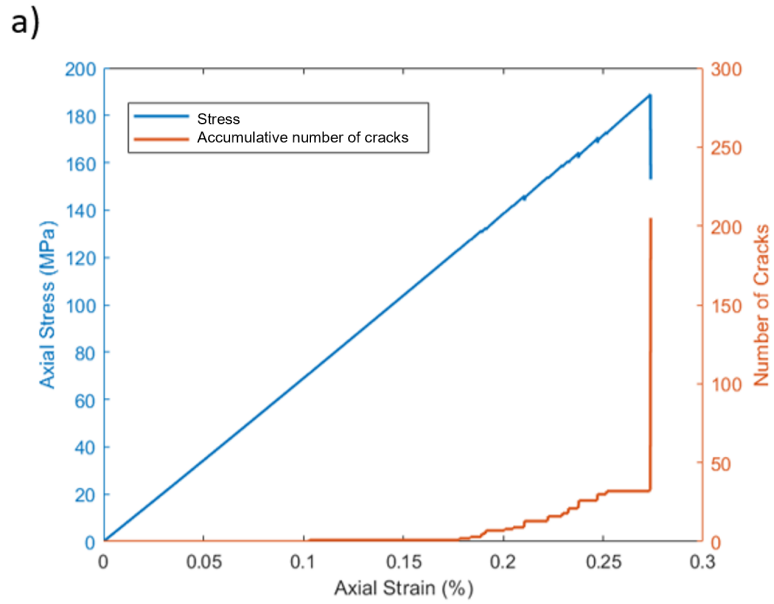


Figure 5.2: The stress-strain response and accumulative number of cracks occurring during unconfined loading of the Lac du Bonnet granite model (a) compared to (b) a similar laboratory test. Modified from source: Martin (1993).

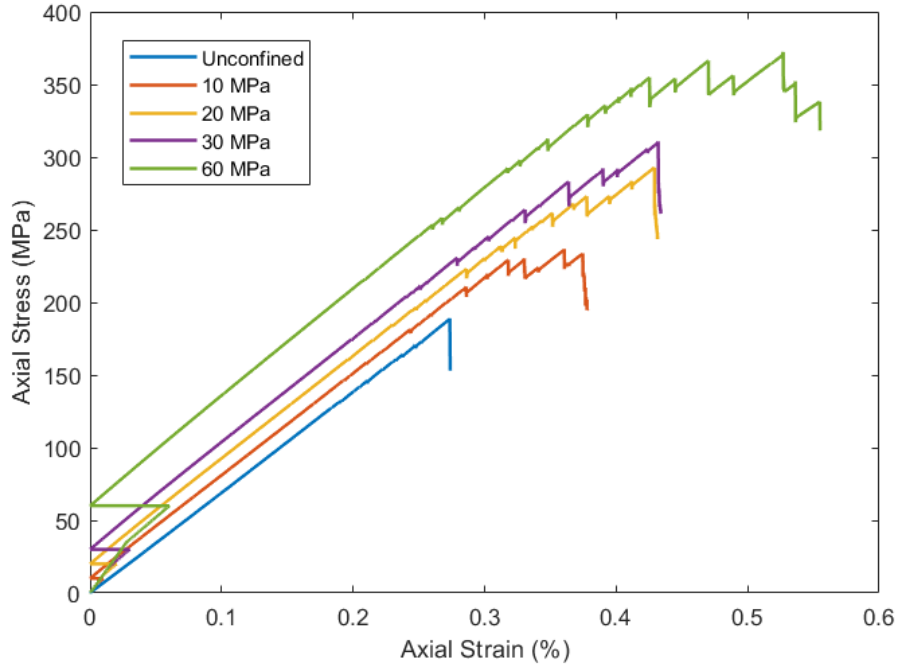


Figure 5.3: Stress-strain curve of the model under different confining conditions.

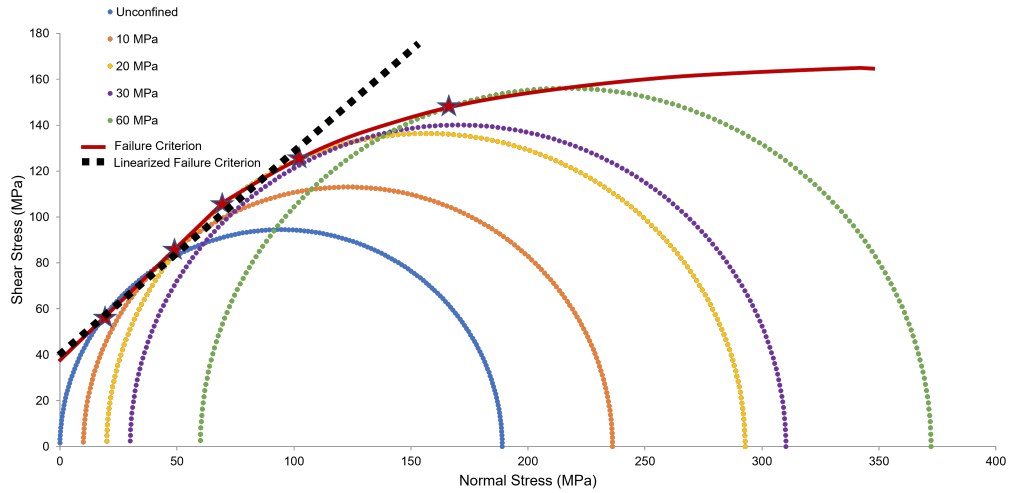


Figure 5.4: Compressive rock strength and failure criterion of Lac du Bonnet granite model expressed as Mohr circles at failure. The red stars indicate where the failures occur along the failure criterion. The black dashed line indicates the linearized Mohr-Coulomb failure criterion.

# Chapter 6

## Analysis of Crack Formation and Internal Force Networks

### 6.1 Introduction

A failure will occur when a piece of rock is subject to sufficiently large stresses. This implies that the rock changes its shape permanently and possibly falls apart. Brittle rock failure can significantly affect many natural and engineered systems, including mining, civil engineering, and the oil and gas industries. Therefore, it is useful to predict under which conditions a rock is likely to fail. However, due to rock inhomogeneities, rock failure is a complex phenomenon that is still not fully understood.

Researchers have devoted efforts to investigating the mechanical properties, constitutive relation, mechanical models and calculation methods of rock failure. Previous studies (Radjai et al., 1996, 1999; Liu et al., 1995; Kondic et al., 2012) suggested that understanding the internal force distribution within a rock mass can be used to predict the failure behaviour of a rock mass. These studies have found that the internal force distribution

is influenced by several factors, such as rock properties, loading conditions, and the presence of pre-existing fractures, which can influence the failure behaviour of a rock mass.

Physical, analytical and numerical approaches can be used to study rock mechanics. Numerical modelling nowadays has become a widely used approach in rock mechanics to investigate the geomechanical behaviour of rock masses under various loading conditions with particle numbers comparable to those found in laboratory specimens while obtaining a complete data set on a microscopic scale.

This chapter will use the bonded particle method to numerically explore the rock failure and internal force networks in brittle intact rocks further. We then bring new insights into 1) crack development under compressive loading, 2) internal force networks within the cemented granular system, and 3) the relationship between the formation of cracks and internal force networks.

## **6.2 Background**

### **6.2.1 Deformation stages**

In addition to the microseismic event detection and monitoring, we also track axial stress and strain changes. The deformation of brittle rocks generally consists of four deformation stages, each of which is the elastic, strain-hardening, peak stress and strain-softening phases (post-peak).

In the elastic phase, the deformation is reversible if the force or load is removed. Elastic deformation is commonly seen at low strains. The elastic deformation can be described by Hooke's Law, which can be demonstrated

by its linear slope, where the stress in the material is always proportional to the strain. If the loading applied to the material increases, it will produce a stress-strain curve that rises continuously but becomes flattered until it reaches its maximum peak stress. This section of the stress-strain curve is called strain-hardening. In this phase, the deformation is plastic and non-reversible, leading to a permanent change in shape that is distinct from the reversible elastic deformation. Next, the stress reaches its maximum peak value at peak stress, immediately followed by a large stress drop. After the peak stress, the strain-softening phase is characterized by decreasing axial stress, indicating that the sample is continuously weakened.

### **6.2.2 Internal Force Networks**

It has been well recognized that defects such as flaws or openings strongly affect the internal stress distribution within samples (Hoek, 1968; Chester and Fletcher, 1997). Under external loading, the stress around flaws and openings gradually evolves. The evolution depends on the arrangement of flaws and openings, e.g., the flaw inclination angle. In bonded-particle models, since the grain particles are randomly placed, this randomness of actual particle packing creates heterogeneity of the internal force distributions. Scholz (1968) postulates that strong stress heterogeneity exists within rock samples subjected to triaxial deformation tests to explain the observed tensile failure mechanisms. Liu et al. (1995) presented large force inhomogeneities in stationary random bead packs. In their model, the force inhomogeneities are affected by the variations in the contact angle.

Several studies have examined internal force networks within the non-cohesive granular system under compression (Kondic et al., 2012; Radjai

et al., 1996, 1998, 1999). Previous studies have subdivided evolving force populations into strong- and weak- forces to analyze the internal force networks, Radjai et al. (1998) discovered the weak- and strong-force networks in the granular sample. The strong-force network has chain-like connected contacts carrying shearing forces stronger than the average force. In the isotropic state, the weak-force network appears to be more dissipative and weaker than the average force. Radjai et al. (1998) also found that most grain-sliding occurs within the weak-force network, whereas the strong-force network is responsible for the major deformation. Van der Baan and Chorney (2019) found out that in the sandstone model, the cracks and acoustic emissions predominantly occur within the weak force network, and the major failure of the rock is only related to the collapse of the strong force network. However, limited studies have focused on the development of force networks within a cohesive, cemented granular system. Also, comprehensive studies have yet to focus on the evolution of the internal force networks regarding the angular distribution. Therefore, this study will deliver new insights into rock failure processes by analyzing the orientation and distribution of the cracks and internal force networks.

### **6.3 Workflow**

The model is subjected to confining pressure at 10 MPa. The top and bottom are loaded at a constant strain rate of 0.01/sec. For other information about the experiment setup, please refer to the Chapter 5.

### 6.3.1 Tracking crack development

In order to understand the crack development process, the axial stress and strain, quantity, time and type of the cracks, and moment magnitude of acoustic emissions are continuously monitored during the simulation. Four observation windows are available at 30% peak stress, 70% peak stress, peak stress and 60% peak stress (post-peak). At observation windows, we use rose diagrams to compare and analyze the crack characteristics at different deformation stages: elastic, strain-hardening, peak and strain-softening. The crack characteristics expressed using the rose diagram will be quantity (length of the bar), orientation (azimuth of the bar), and tensile or shear (colour of the bar).

In many numerical studies of cracks, only the formation time and quantity of cracks are analyzed (Cundall and Strack, 1979a; Van der Baan and Chorney, 2019). However, in this chapter, we also bring crack type and orientation together to generate the rose diagrams, allowing us to visualize the angular distribution of tensile and shear cracks.

### 6.3.2 Identifying properties of the three distinct force networks

Previous research conducted by Van der Baan and Chorney (2019) demonstrated two distinct internal force networks that force magnitudes can distinguish. In this study, there are actually three distinct force networks in compressive force regimes. Also, in addition to the regular force analysis done by plotting quantity versus force magnitude, we examine the angular dependence of force magnitude to see if tensile and compressive forces tend to concentrate on certain angles. Therefore, the force distribution diagrams

be two-dimensional polar plots. The radius of the polar plot represents the force magnitude, azimuth represents the force orientation, and colour represents the quantity.

### **6.3.3 Identify the failure mechanism, the relationship between the formation of cracks and force networks**

Combining the results of crack development and force networks, we then be able to analyze the results and see how the crack formation is linked to the internal force networks. This allows us to understand the formation of microseismicity and the failure mechanism of macro events.

## **6.4 Results**

### **6.4.1 Crack Development**

#### **Stress drops and associated brittle deformation**

Recall that a bond breakage in the modelling represents a single micro-crack. When multiple bond breakages occur at a connected time and location, those micro-cracks are identified as part of the same rupturing event, which is an AE event. The top section of Figure 6.1 shows the changes in axial stress and AE event magnitude (orange circles) as strain increases with loading. The bottom section demonstrates the corresponding cracks formed in terms of their type and quantity. Four observation windows are indicated as red dots at 30% peak stress, 70% peak stress, peak stress and strain-hardening stress (60% peak stress). Each observation window is randomly

selected from the deformation phases: elastic, strain-hardening, peak and strain-softening.

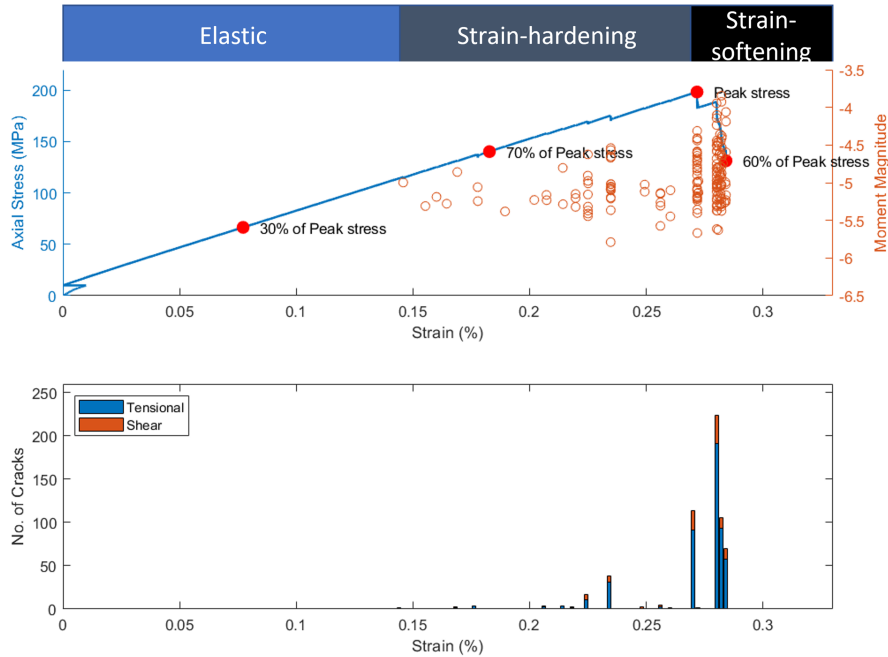


Figure 6.1: Top diagram: histories of stress-strain (blue line), moment tensor (orange circles) with four observation windows (red dots) 30% peak stress, 70% peak stress, peak stress and 60% peak stress (post-peak). Each observation window is selected from the middle of each deformation phase: elastic, strain-hardening, peak and strain-softening. Bottom diagram: monitoring the type and quantity of the cracks.

The left y-axis of the top section of Figure 6.1 is the axial stress in MPa. The x-axis is the axial strain in percentage ( $10^{-2}$ ). The axial stress linearly increases in the elastic phase until bonds break and form cracks. Then, it enters the strain-hardening phase, where the stress slope gradually decreases. The cracks form when stress is released, and strain energy is converted to kinetic energy. After a temporary stress drop, stress increases due to the constant loading. The peak stress occurs at the second stress drop, where the strain is 0.0027. After reaching the peak stress, the rock abruptly fails,

accompanied by a significant drop in stress and the generation of numerous cracks, and this deformation stage is called strain-softening.

The right y-axis of the top section of Figure 6.1 is the moment magnitude of the AEs indicated as the orange circles. When multiple bond breakages occur at a connected time and location, those cracks resulting from the bond breakages are identified as part of the same AE. The first acoustic emission indicates that the deformation phase transitions from the elastic to strain-hardening phase. In the strain-hardening phase, the axial strain and stress consistently accumulate. We observe the abundant number of AEs occurring at the peak stress. After the peak stress, we have a short time of temporary silence. The stress increases until it eventually reaches the major failure, where we see a significant cluster of AEs and the biggest AE event, whose moment magnitude is about -3.8 Mw.

The lower section of Figure 6.1 shows the monitoring of cracks and the crack type, either the tensile or shear crack. Like the AEs distribution, no crack formed in the elastic phase until entering the strain-hardening phase. In general, the majority of the cracks are tensile. Tensile cracks initiate first, and then the shear cracks occur later in the strain-hardening stage. The first crack that appears is a tensile crack at the axial strain of 0.00142, followed by a few scattered tensile cracks. The first shear crack manifests at a strain of 0.00225. Furthermore, Figure 6.1 also demonstrates that the last two stress drops have a much larger portion of shear failures than previous AEs.

## Crack Analysis

Based on the relationship among rock stress, times of AE events, and deformation phases, we show that stress, cracks, and AE events are all connected. Then, we further investigate the properties of the crack orientation to complete the crack analysis.

Figure 6.2 records the development of cracks, and it contains the rose diagrams showing the quantity and orientation of the cracks at each observation window. The elastic phase is at the point where 30% of the peak stress is reached. The observation window for strain hardening occurs at 70% of the peak stress. The peak stress itself is identified at the moment when the maximum stress is achieved. Lastly, the strain softening phase is at 60% of the peak stress. Since no cracks are formed in the elastic stage, only the strain-hardening, peak and strain-softening (post-peak) windows have crack data available. The length of the bar represents the quantity of the cracks, and the azimuth represents the orientation of the cracks. The orientation angle of the cracks is predominantly steep, indicating that they are most nearly vertical. The cracks formed in the strain-softening stage are significantly more than in the peak stage, indicating that most of the cracks formed are due to the final catastrophic failure.

In Figure 6.2, we can see the evolution of the crack distribution in terms of the orientation. No crack has yet been formed in the elastic phase. In the strain hardening phase, most cracks have an inclination angle, not exactly vertical but close to  $90^\circ$ . In our analysis,  $90^\circ$  represents the vertical angle and  $0^\circ$  and  $180^\circ$  indicate the angles are horizontal. This observation indicates that these cracks are likely tensile, which is also consistent with the previous results in Figure 6.1. The longest bar in the histograms does

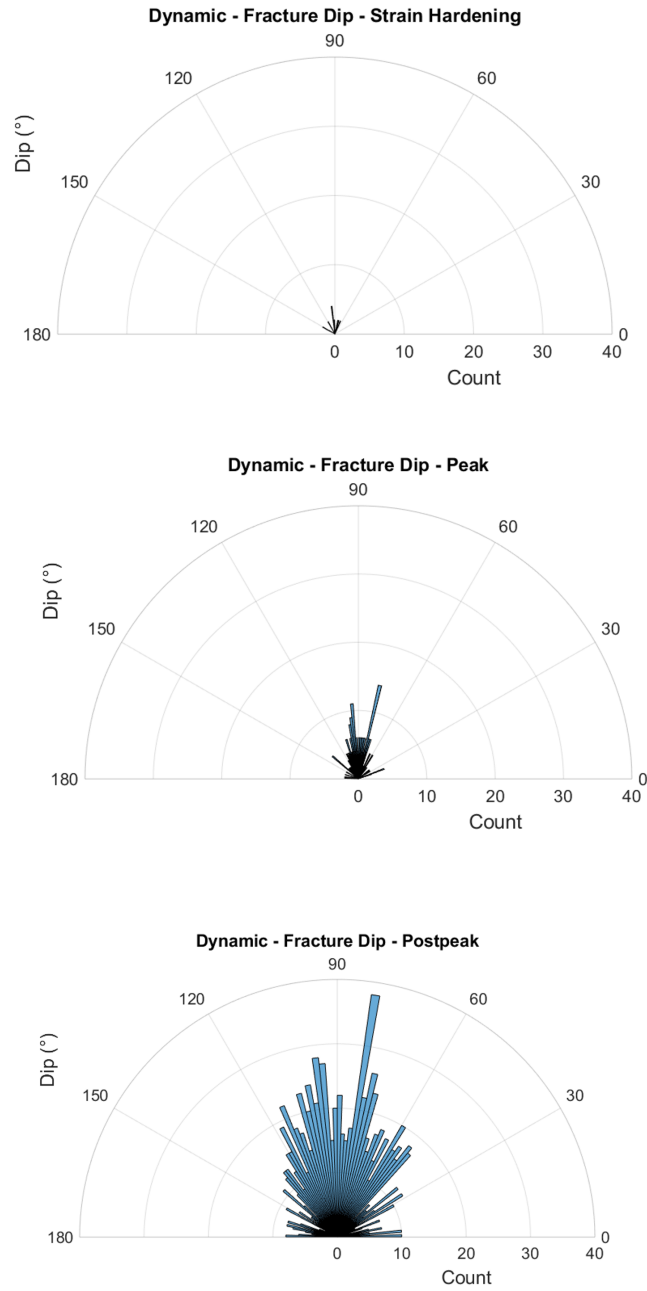


Figure 6.2: Rose diagrams at observation windows representing the strain-hardening, peak and strain-softening (post-peak) phases. The length of the bar represents the quantity of the cracks, and the azimuth represents the orientation of the cracks.

not change its orientation during the compressive test when the strain-hardening phase is compared with the post-peak phase. However, this angle is steeper than the orientation of the final catastrophic failure, implying other factors lower the orientation of final catastrophic failure, and there is no direct correlation between the orientation of tensile cracks and final catastrophic failure.

### **6.4.2 Internal Force Networks**

Radjai et al. (1998) identified two distinct force networks within the granular sample: one with a chain-like network carrying strong, above-average forces and another with weaker-than-average forces. Similarly, Topin et al. (2007) explored a granular medium with cemented contacts, finding an uneven stress field and a division between strong- and weak-force networks. Cundall and Strack (1979a) also reported the presence of strong and weak force networks in a bonded-particle sample. Furthermore, Van der Baan and Chorney (2019) not only confirmed the existence of these networks but also determined that the macro-failure stems from the breakdown of the strong-force network.

In order to understand the force network within the rock, we need to decompose the forces, based on PFC2D, into linear parallel bond model composed of linear contact forces and parallel bonded forces. The linear contact interface carries compressive and shear forces, but it does not resist tension and relative rotation. The parallel bonded interface describes the cement behaviour. The parallel bond carries forces and moments and resists tension and relative rotation. When the parallel bond interface is bonded, it is linearly elastic until the strength limit is exceeded and the bond breaks,

making it unbonded. After the bond breaks, the parallel bond is removed. The unbonded linear parallel bond model is equivalent to the linear contact model. Please refer to the linear parallel bond model explained in Chapter 3 for a detailed explanation.

### **Spatial Distribution of Forces**

Figure 6.3 shows the force chain of total forces for 10 MPa confining pressure at different deformation stages. The total force is the result of linear contact forces (Figure 6.4), and parallel bond forces (Figure 6.5), which also can be categorized into compressive parallel bond forces and tensile parallel bond forces (Figure 6.6).

### **1-D Force Distribution**

Similar to what is found in earlier studies (Van der Baan and Chorney, 2019), we noticed that all the forces in the different deformation stages have exponential distributions with linear or bi-linear slopes in the logarithmic domain. For all forces, the slope decreases due to a faster decline in the quantity of forces as the force magnitude increases. The tensile parallel bond forces have higher absolute logarithmic gradients than the other compressive forces for all deformation states. This implies a faster decay in the distribution of tensile parallel bond forces than for the compressive ones, yet tensile forces exist in all deformation stages.

The evolution of the resultant total force is illustrated in Figure 6.7. Upon comparison with the linear contact forces (Figure 6.8), compressive parallel bond forces (Figure 6.9), and tensile parallel bond forces (Figure 6.10), it becomes apparent that these two factors predominantly influence

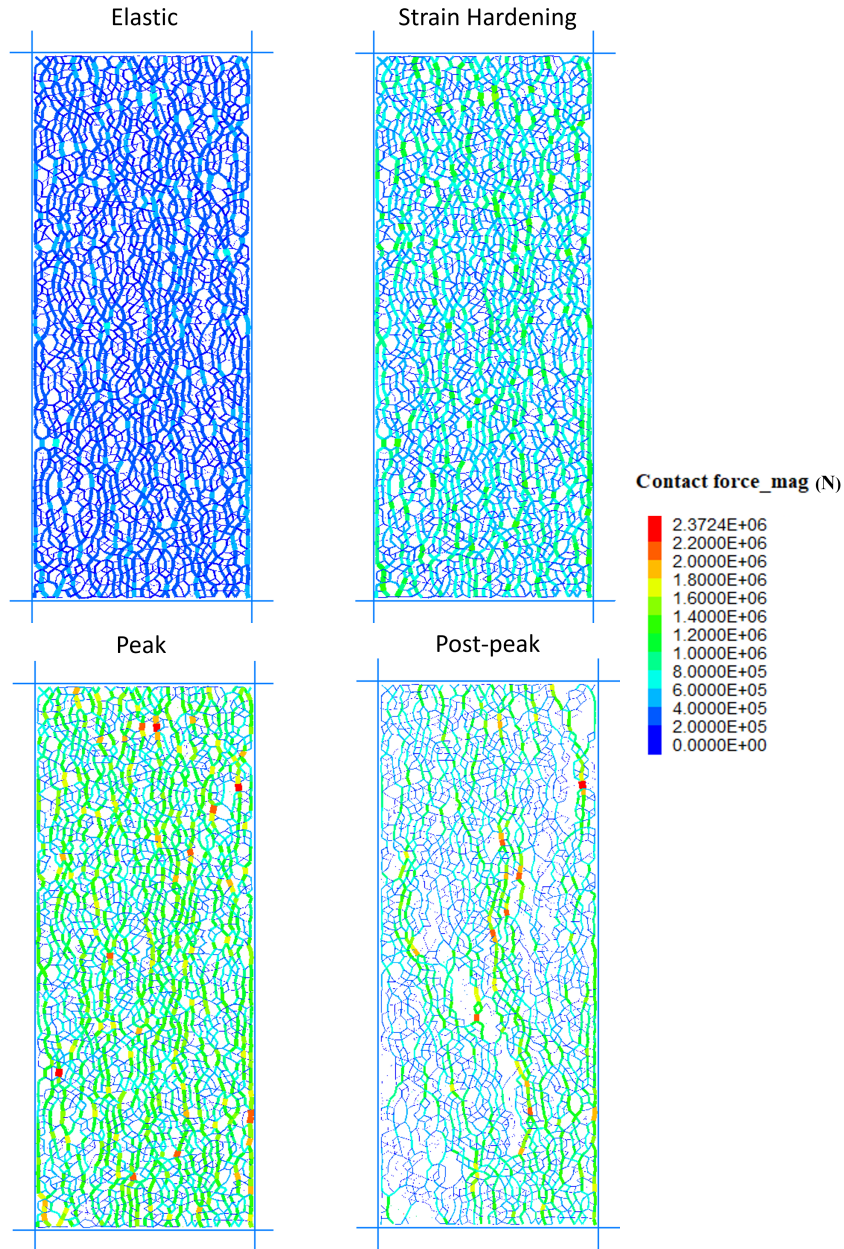


Figure 6.3: Spatial evolution of total force at elastic, strain-hardening, peak and strain-softening (post-peak) deformation stages in unit of  $N$ . The colored veins represent the forces in the bonds. The colour of the vein indicates the force magnitude. The tensile forces are in blue, and the compressional forces are in red.

the resultant total forces. This dominance is attributed to the lesser abundance and weaker force magnitude of tensile parallel bond forces.

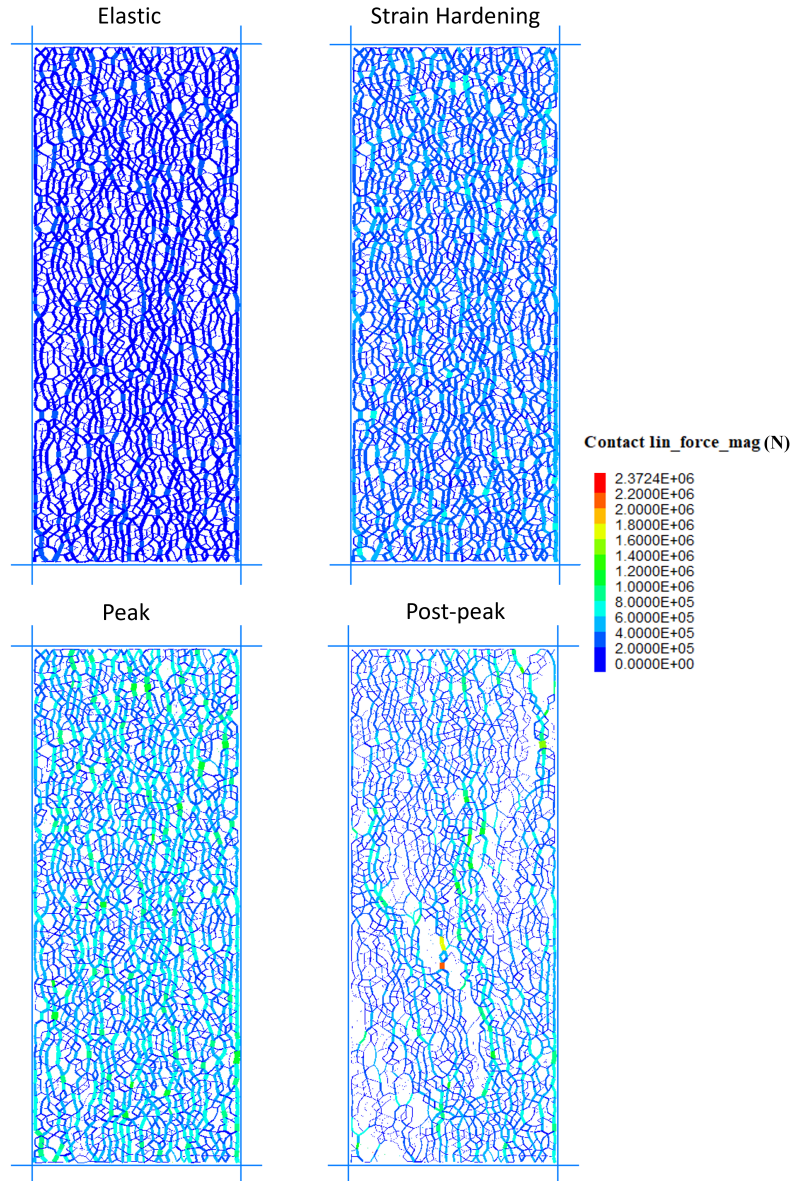


Figure 6.4: Spatial evolution of linear contact forces at elastic, strain-hardening, peak and strain-softening (post-peak) deformation stages in unit of  $N$ . The colored veins represent the linear contact forces in the bonds. The colour of the vein indicates

From elastic to peak phases, all total forces, linear contact forces and parallel bond forces continuously grow. The linear contact forces and compressive parallel bond forces are both compressive. Compressive forces predominantly exist within the sample, and the absolute magnitude of the

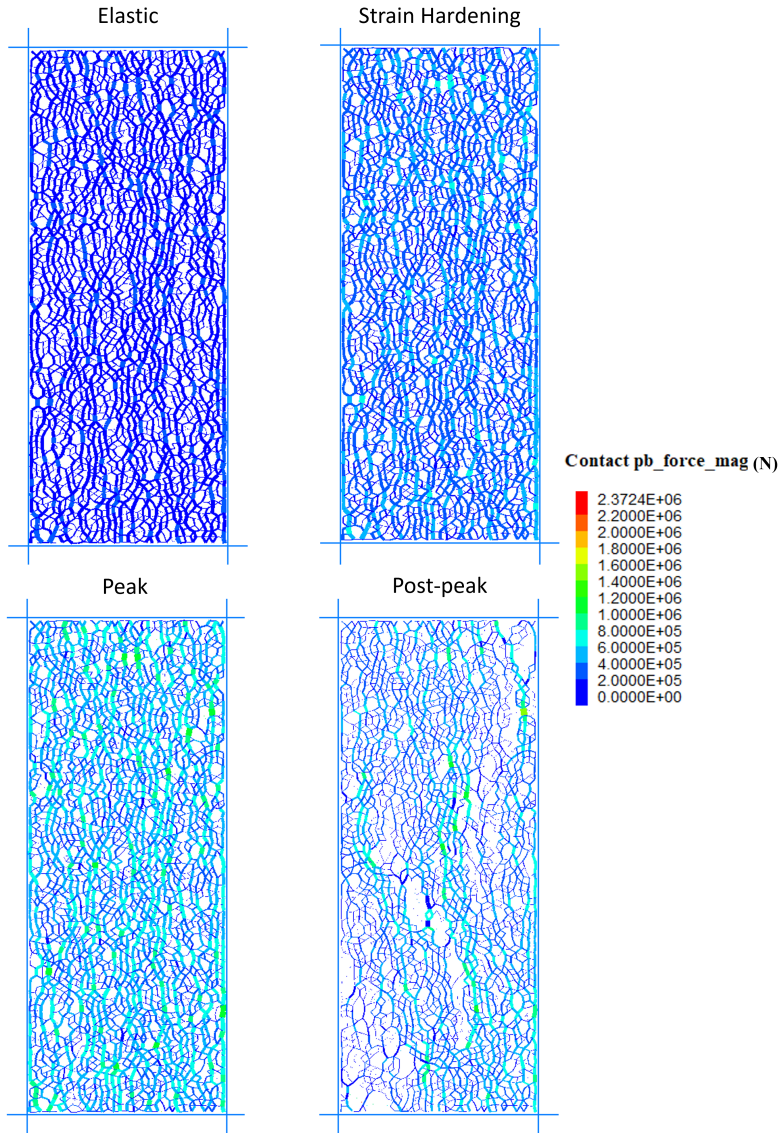


Figure 6.5: Spatial evolution of parallel bond forces at elastic, strain-hardening, peak and strain-softening (post-peak) deformation stages in unit of  $N$ . The colored veins represent the parallel bond forces in the bonds. The colour of the vein indicates the force magnitude.

maximum compressive parallel bond force is about twice that of the maximum tensile parallel bond force. Both compressive forces, linear contact forces and compressive parallel bond forces, clearly show a stronger force subgroup indicated by a significantly larger force magnitude accompanied with a wider base (Figure 6.8 and Figure 6.9). After the peak stress is

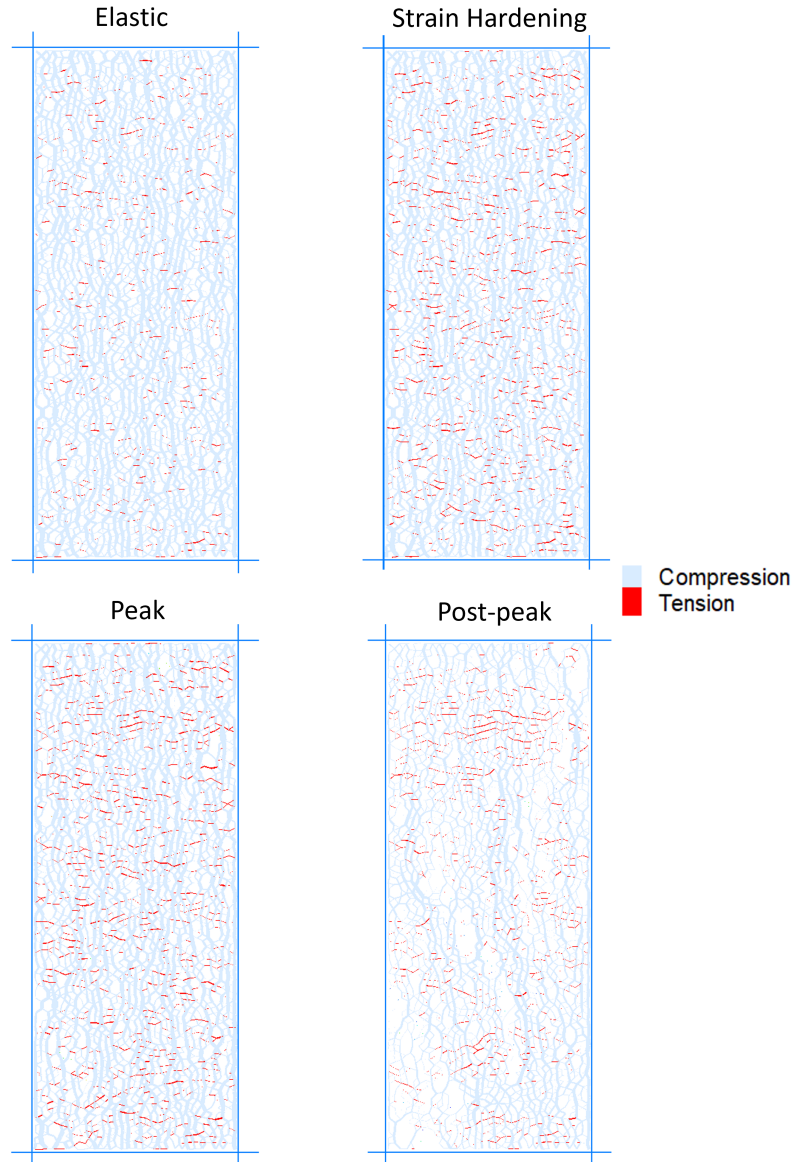


Figure 6.6: Spatial distribution of compressive parallel bond forces and tensile parallel bond forces at elastic, strain-hardening, peak and strain-softening (post-peak) deformation stages in unit of  $N$ . The colored veins represent the parallel bond forces in the bonds. The thickness of the vein indicates the force magnitude. The tensile forces are in red, and the compressional forces are in light blue.

reached, all the forces, regardless of compressive and tensile, show some degree of recession; however, the compressive forces (linear contact force and compressive parallel bond forces) decline more than the tensile parallel

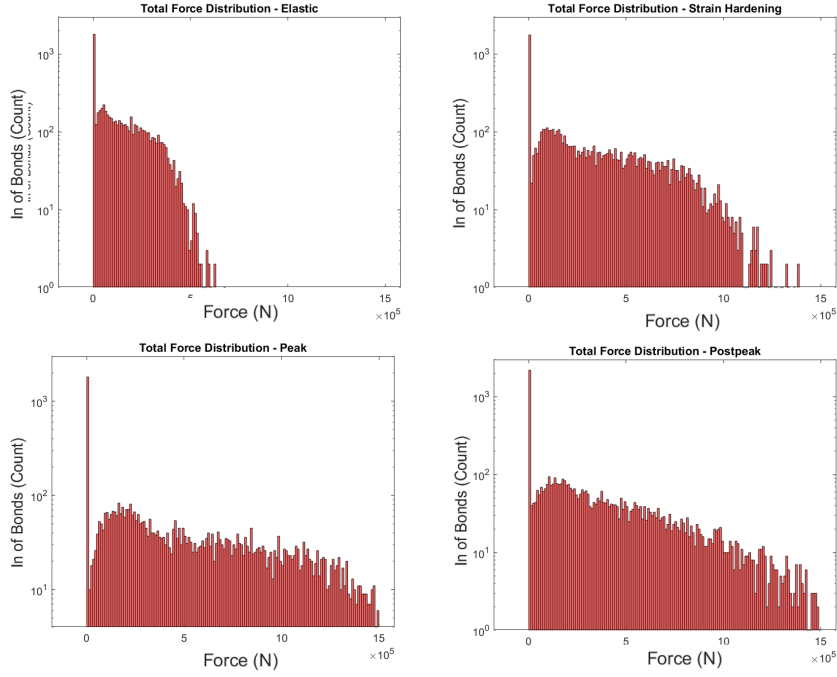


Figure 6.7: Evolution of total force for elastic, strain-hardening, peak and strain-softening (post-peak) deformation stages in unit of  $N$ . The x-axis represents the force magnitude. The y-axis represents the count of occurrence in a natural logarithmic scale.

bond forces, as shown in the strain-softening phase.

## 2-D Force Distribution

1-D force analysis directly visualizes the quantitative distribution of strong and weak force networks regarding the force magnitude. We create a two-dimensional diagram to examine how the weak and strong force networks vary with angle and to display the abundance of forces of varying magnitudes. Figure 6.11 displays the total force distribution at various deformation stages. The azimuth presents the linear parallel bond orientation, the radius represents the force magnitude of the linear parallel bonds, and the colour represents the occurrence count.

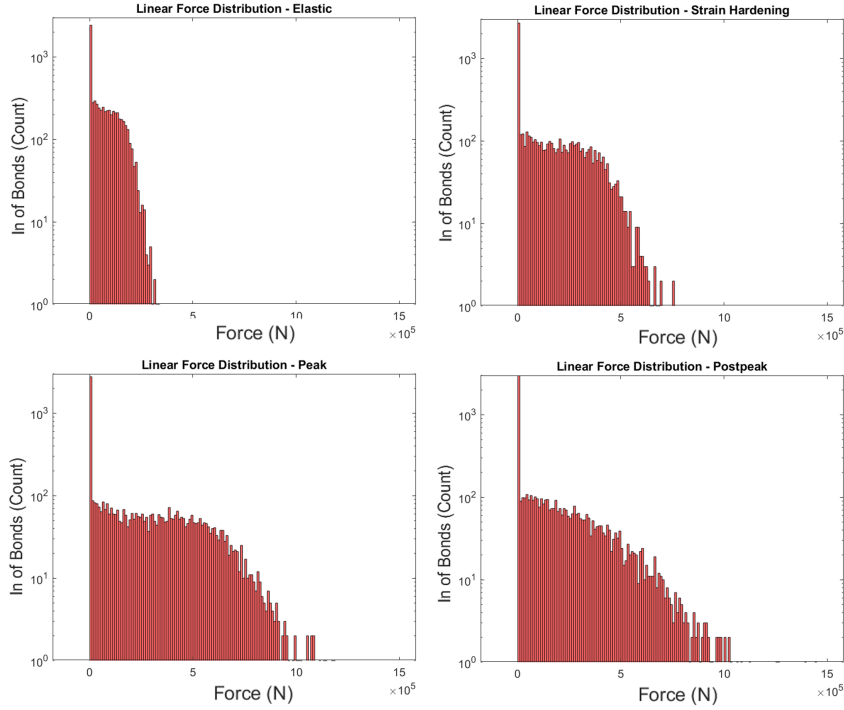


Figure 6.8: Evolution of linear contact force for elastic, strain-hardening, peak and strain-softening (post-peak) deformation stages in unit of  $N$ . The x-axis represents the force magnitude. The y-axis represents the count of occurrence in a natural logarithmic scale. The linear contact forces are compressive only.

While Figure 6.11 shows a 2D total force distribution, Figures 6.12 - 6.14 show the linear contact forces, compressive parallel bond forces and tensile parallel bond forces, respectively.

In Figure 6.11, the total forces show evident and consistent angular preference throughout the deformation stages. We discovered that clear boundaries separate the force network, and these two angles that separate the three force subgroups are identified as critical angles. We named them as force subgroups: Strong A, Strong B, and Weak Force subgroups. We see the development of the Strong force subgroups A and B throughout the first three deformation stages. The top "rays" in Figure 6.11 represent the

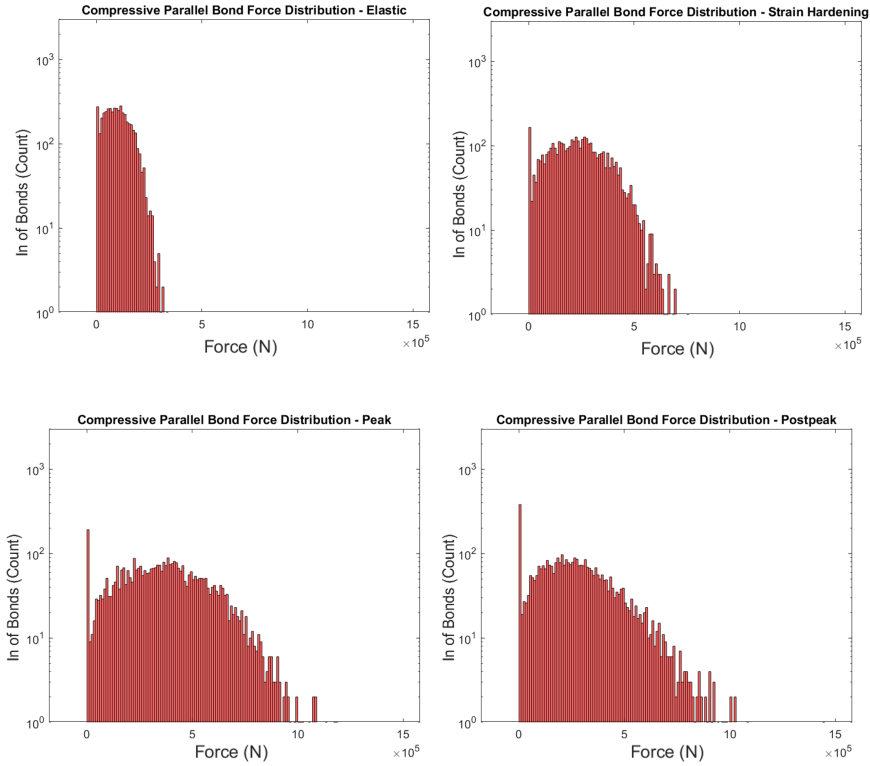


Figure 6.9: Evolution of compressive parallel bond forces for elastic, strain-hardening, peak and strain-softening (post-peak) deformation stages in unit of  $N$ . The x-axis represents the force magnitude. The y-axis represents the count of occurrence in a natural logarithmic scale.

Strong A force subgroup consisting of the group of bonds that has a larger force in it, and the middle "rays" are the Strong B force subgroup with an intermediate magnitude of force in it. The bottom "fan" represents the Weak force subgroup. These two Strong force subgroups are not present in the elastic phase, but the central "fan" expands and grows in azimuth and magnitude in the strain-hardening phase until the peak stress is reached. In the strain-softening (post-peak) phase, the strong force network starts to decline and shrinks in size, indicating the collapse of the force subgroups in terms of its force magnitude. Also, we notice that the Strong A, Strong B and Weak force subgroups are separated by critical angles, which can be

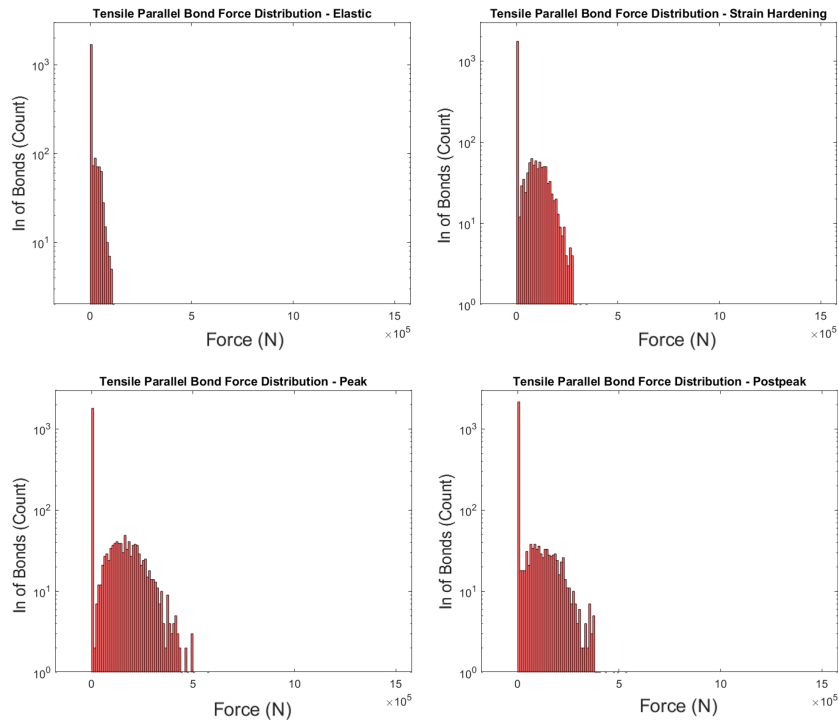


Figure 6.10: Evolution of tensile parallel bond forces for elastic, strain-hardening, peak and strain-softening (post-peak) deformation stages in unit of  $N$ . The x-axis represents the force magnitude. The y-axis represents the count of occurrence in a natural logarithmic scale.

clearly shown in the peak stage (Figure 6.11).

In Figure 6.11, we can see that the critical angle between Weak and Strong B is at  $38^\circ$ , and the critical angle separating Strong A and B is  $64^\circ$ . These two critical angles are also can be found in the other two compressive force regimes, the compressive linear contact forces (Figure 6.12) and compressive parallel bond forces (Figure 6.13).

Figure 6.11 displays the resultant total force acting within the rock. It is evident that this resultant total force is notably shaped by two compressive force networks: the linear contact forces (Figure 6.12) and the compressive parallel bond forces (Figure 6.13). These compressive networks exhibit sim-

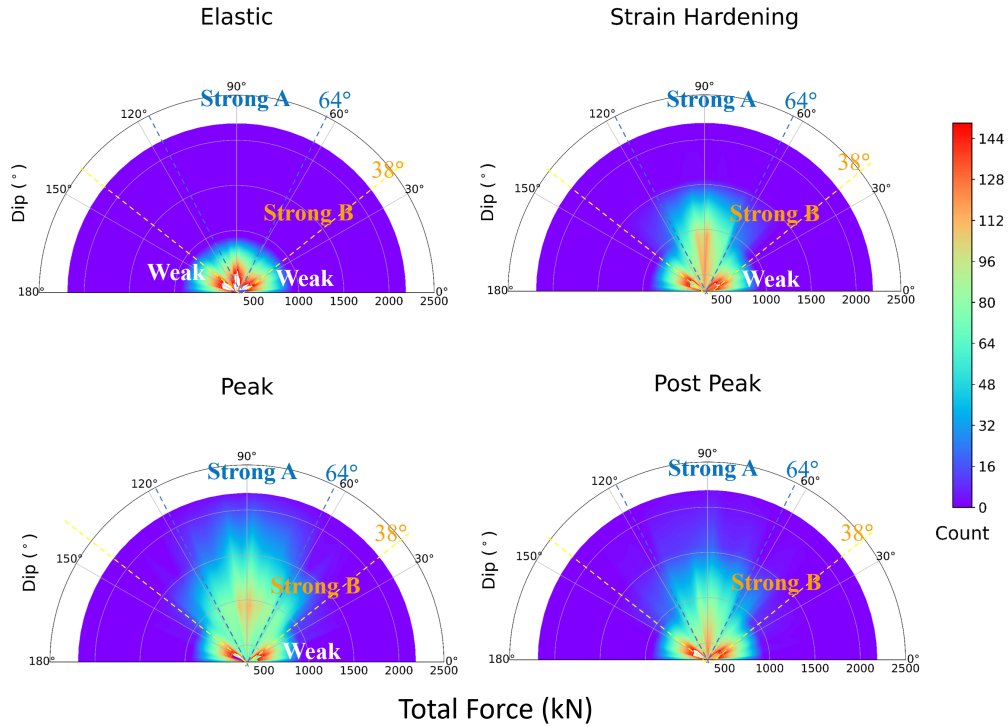


Figure 6.11: The 2D total force distribution for the elastic, strain-hardening, peak and post-peak phases for the elastic, strain-hardening, peak and post-peak phases. There are three force subgroups: Strong A, Strong B, and Weak Force subgroups. The critical angles are the boundaries between force subgroups. Radius represents the force magnitude. The azimuth presents the dipping of the linear parallel bond, and the colour represents the count of occurrence.

ilar force progression and align with identical critical angles, contributing substantially to the resultant force.

In terms of the tensile parallel bond forces (Figure 6.14), there is no Strong force subgroup. They are only associated with one Weak force network, as found in one-dimensional force results. The two "fans" below the critical inclinations represent the weak forces. For the tensile forces, the only weak force network mainly concentrates in the horizontal zone between  $0^\circ$  and  $38^\circ$ .

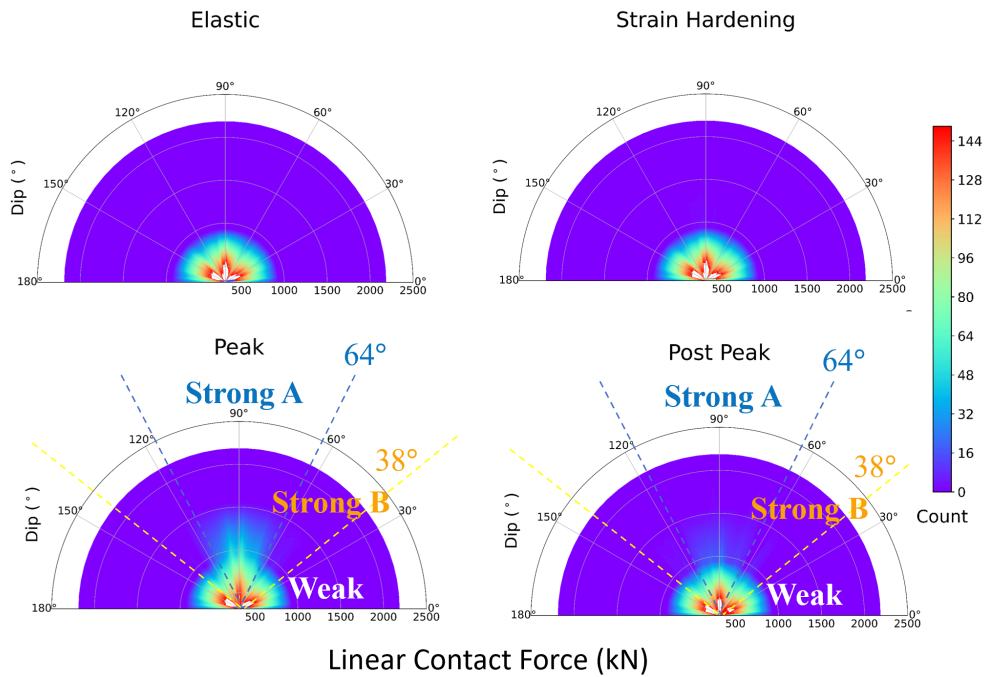


Figure 6.12: The 2D linear contact force distribution for the elastic, strain-hardening, peak and post-peak phases for the elastic, strain-hardening, peak and post-peak phases. There are three force subgroups: Strong A, Strong B, and Weak Force subgroups. The critical angles are the boundaries between force subgroups. Radius represents the force magnitude. The azimuth presents the dipping of the linear parallel bond, and the colour represents the count of occurrence.

### 6.4.3 Final failure plane and spatial distribution of forces

Figure 6.15 shows the spatial distribution of the resultant force network and cracks. The left graph shows the spatial distribution of the resultant total force network, represented by the veins. The colour of the vein indicates the force magnitude in the bonds. The red line segments represent the cracks formed in the granite specimen. The right graph shows the spatial distribution of acoustic emissions, and the crosses represent the moment magnitude of the acoustic emissions.

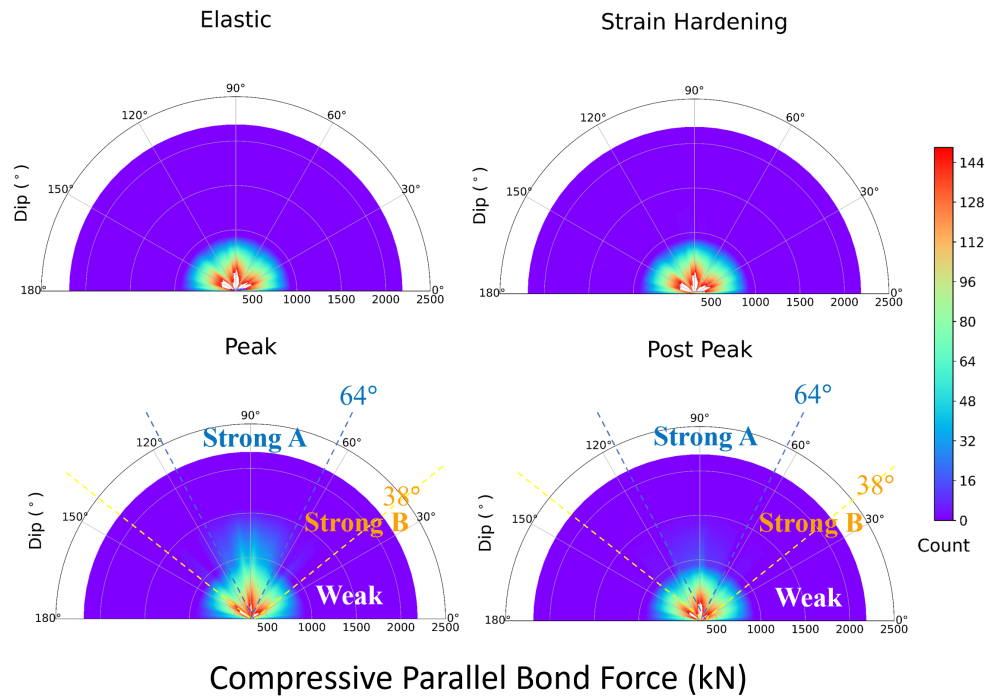


Figure 6.13: The 2D compressive parallel bond force distribution for the elastic, strain-hardening, peak and post-peak phases for the elastic, strain-hardening, peak and post-peak phases. There are three force subgroups: Strong A, Strong B, and Weak Force subgroups. The critical angles are the boundaries between force subgroups. Radius represents the force magnitude. The azimuth presents the dipping of the linear parallel bond, and the colour represents the count of occurrence.

Both internal force and moment tensor graphs in Figure 6.15 show the shearing plane, indicated by the linearly clustered cracks and acoustic emissions. From Figure 6.15, we found that the shearing plane occurs at  $64^\circ$ . The shearing plane is indicated by a high force gradient, i.e., a sudden change in force magnitude colors. To be more specific, the shearing plane is located in weak forces and adjacent to the strong force network. Also, the shearing plane angle well matches the orientation of the critical angle we previously found between Strong A and B in Figure 6.11, and by its nature, we know that this critical angle is exactly where the force gradient is high.

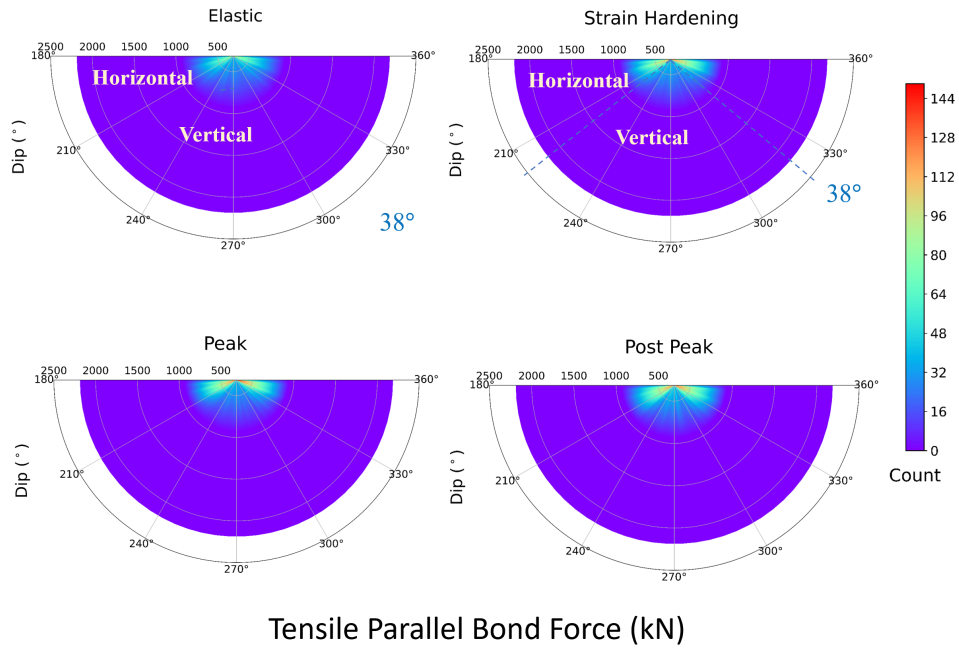


Figure 6.14: The 2D tensile parallel bond force distribution for the elastic, strain-hardening, peak and post-peak phases for the elastic, strain-hardening, peak and post-peak phases. For tensile forces, there is only one Weak force subgroup with critical angle  $38^\circ$ . Radius represents the force magnitude. The azimuth presents the dipping of the linear parallel bond, and the colour represents the count of occurrence.

## 6.5 Discussion

### 6.5.1 Crack Development

#### Stress Drop

Similar to earthquake stress drop (Kanamori, 1977, 1978; Kanamori and Brodsky, 2004; Scholz, 2019), we notice that every stress drop is also accompanied by acoustic emission and crack formation on a microscopic scale. In a sequence of events involving foreshocks, the mainshock, and aftershocks, the mainshock is typically where the most substantial decrease in stress

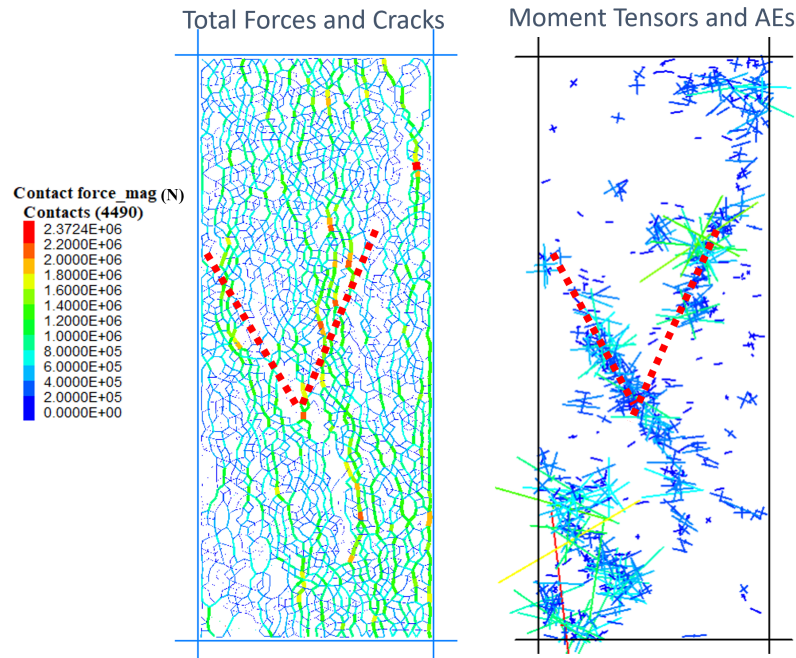


Figure 6.15: The total force and acoustic emissions after peak pressure. On the left graph, veins in the background are forces in bonds with colour-coded magnitudes and the thick dashed lines represent the location of the major shearing plane. On the right graph, the crosses represent the moment tensor of acoustic emissions. The size of the cross is proportional to the magnitude, which is also color-coded.

occurs (Van der Baan and Chorney, 2019).

Van der Baan and Chorney (2019) also found that the largest stress drop  $\Delta\sigma_{\text{main}}$  changes with different confining pressure applied and that the largest stress drop is inversely proportional to confining stress. Confining pressure increases the viscous component of deformation and the rock's ductility. The increase in ductility occurs because the confining pressure prevents the opening of cracks and fissures during deformation, effectively forcing the rock to change shape rather than rupture. In our simulation, 10 MPa is applied as the confining pressure, which is considered low to increase the ductility of brittle granite rock models. With low confining pressure,

our models experience a large stress drop at the mainshock with a steep angle, indicating low ductility.

Additionally, as Van der Baan and Chorney (2019) found, we observe that (Figure 6.1): 1. the mainshock occurs where the stress drop is most significant; 2. the cracks and acoustic emissions accelerate during the strain-hardening stage, but very few acoustic emissions occur during the elastic phase; 3. the largest acoustic emission event occurs after the peak stress reached; 4. after the largest event, the subsequent event rate continuously decreases during the following strain-softening phase. In addition to the above, from the relationship between stress-strain and moment tensors of acoustic emissions, we also found that the most significant stress drop indicates the mainshock and is accompanied by the largest acoustic emission size, the highest crack formation rate and the highest acoustic emission rate. In seismology, the stress drop  $\Delta\sigma_{\text{fault}}$  relates to the energy of the radiated seismic wave (Kanamori, 1977; Kanamori and Brodsky, 2004). When a bond breaks, leading to crack formation, a reduction in stress is anticipated due to the release of accumulated strain energy in the form of seismic waves. Consequently, the most significant decrease in stress suggests a considerable sudden release of strain energy, marked by numerous and intensive seismicities. The largest observed acoustic emission size, the highest rate of crack formation, and the highest acoustic emission rate evidence this.

### **Shear-tensile Distribution**

The lower section of Figure 6.1 shows tensile and shear cracks. Zhang et al. (2019) argues that under low-stress levels, the initially formed cracks are predominantly tensile and have little influence on the stress redistribution

of the sample. The stress redistribution and concentration phenomenon will be more obvious with the increased number of broken bonds. The specimen damage increases shear movement and accelerates the crack propagation (Zhang et al., 2019). The shear-tensile distribution shows that tensile crack is always dominant during failure. Shear cracks only occupy a minor portion of the crack formation rate, which is about 12.7%. Also, we found that only tensile cracks formed at the beginning (Figure 6.1). The cracks before peak stress are mainly tensile, and there were a few shear cracks during the late strain-hardening phase. The first local shear crack occurs when the stress is high, around 150 MPa, and the shear crack becomes obvious after passing the peak stress. Furthermore, the highest shear-tensile crack ratio is found where the major failure is. As the tensile and shear microcracks propagate and nucleate, they further develop into a larger shearing plane as the final stage of specimen failure.

### **Crack Orientation**

In Figure 6.2, we can see the evolution of the crack distribution in terms of the orientation. No crack has yet been formed in the elastic phase. In studying the fracture of brittle materials subjected to tension, a fracture is usually expected to form and propagate in a direction perpendicular to the normal stress and parallel to the shear stress (Hoek and Bieniawski, 1965). In the uniaxial compressive test, the tensile stresses in the directions perpendicular to the compression axis are not being suppressed by compression. As the compressive loading proceeds, these tensile stresses get stronger and cause propagation of preferably oriented pre-existing defects or parts of wing cracks (Dyskin and Sahouryeh, 1997). As a result, the

dilation occurs along the tensile stresses, as the wing cracks align with the direction of the maximum compression (Bobet and Einstein, 1998). This explains why we observe the orientation of cracks are mostly close to vertical with some degrees of inclination (Figure 6.2). This observation indicates that these cracks are likely tensile, consistent with the previous results in Figure 6.1.

### Orientation of Failure

Based on the modified Griffith theory previously mentioned in Chapter 2, Sibson (1990) identified the failure plane as favourably oriented, unfavourably oriented or severely misoriented based on the failure plane orientation to the principle stresses. The favourable orientation for fault reactivation is where the stress ratio,  $R = (\sigma_1/\sigma_3) = (1 + \mu \cot \theta_r)/(1 - \mu \tan \theta_r)$ , is low, where  $\theta_r$  is the angle of reactivation between failure plane and  $\sigma_1$  (Figure 2.3). This stress ratio  $R$  reaches a minimum positive value at the optimum angle for reactivation given by  $\theta_r^* = \frac{1}{2} \tan^{-1}(1/\mu)$  and the stress ratio will be  $R^* = \left(\sqrt{1 + \mu^2} + \mu\right)^2$ . This stress ratio  $R$  reaches infinity when  $\theta_r = 2\theta_r^*$ , so-called the potential "locked-up" angle, indicating that the stress ratio needed for failure plane reactivation goes to infinity. When  $\theta_r > 2\theta_r^*$ , i.e., the "locked-up" angle is exceeded, failure plane reactivation would not occur unless the minimum principal stress becomes tensile  $\sigma_3 < 0$  or pore fluid press  $P_f > \sigma_3$ .

Therefore, according to Sibson (1990), for typical rock friction coefficients, it is unlikely that normal faults will be reactivated as high-angle reverse faults or thrusts as low-angle normal faults unless the effective least principal stress is tensile. In Chapter 2, we discussed the Mohr Circle. It is

worth noting that the  $\theta$  used in Mohr's circle is between the failure plane and  $\sigma_3$  while the  $\theta_r$  used in Sibson's reactivation angle is the angle between the failure plane and  $\sigma_1$ . We can link Sibson's optimum reactivation angle with the idea of Mohr's circle: the optimum condition for fault reactivation is exactly where the Mohr's circle is touching the failure envelope (Figure 2.2), i.e., the angle of failure plane given by the Mohr's circle is same as the Sibson's optimum reactivation angle,  $\theta_r^* = 90^\circ - \theta$ .

From the Mohr Circle analysis detailed in Chapter 5, the friction coefficient of the granite sample is determined to be  $\mu = 0.83$ . Using this value in Equation of optimum angle for reactivation  $\theta_r^* = \frac{1}{2} \tan^{-1}(1/\mu)$ , the  $\theta_r^*$  for our granite sample is calculated to be  $25.2^\circ$ . Since this  $\theta_r^*$  is the angle from the direction of the  $\sigma_1$ , it is equivalent to  $64.8^\circ$  from the horizontal direction. This closely aligns with the final failure plane orientation and our Mohr Circle Analysis, suggesting that the optimum reactivation angle may serve as a reliable estimate for the final failure orientation angle.

## 6.5.2 Internal Force Distribution

### Force Subgroups

In previous studies conducted by Van der Baan and Chorney (2019), they identified the presence of both a weak and a strong force network within the rock. They also discovered a phenomenon of slope change in the 1D force distribution from the elastic stage to the final strain-softening stage. Our experiment also found these phenomena, prompting us to investigate these observations further.

We analyze the 1D force distribution by breaking it down according to the critical angles previously identified in 2D force distributions at  $38^\circ$

and  $64^\circ$ . These critical angles can be found in all linear contact forces, compressive parallel bond forces, and the resultant total force, as these two compressive force networks notably shape the resultant total force. These critical angles also can be found in Figure 6.16 for total forces, in Figure 6.17 for linear contact forces and in Figure 6.18 for the compressive parallel bond forces. For tensile parallel bond forces (Figure 6.19), the critical angle is  $38^\circ$ .

Our observation and analysis show that five distinct force subgroups are present within the brittle rocks under compression. There are three subgroups present in the compressive forces (Figure 6.12 and Figure 6.13): the Weak force group is oriented between  $0^\circ$  and  $38^\circ$ , the Strong B subgroup is between  $38^\circ$  and  $64^\circ$ , and the Strong A subgroup between  $64^\circ$  and  $90^\circ$ . There are two subgroups present in the tensile parallel bond forces (Figure 6.14), and the horizontal force group is oriented between  $0^\circ$  and  $38^\circ$ , and the vertical subgroup between  $38^\circ$  and  $90^\circ$ .

Once the critical angles and force subgroups are identified, it becomes possible to isolate the 1D force distribution of each force subgroup from the total forces (Figures 6.20 - 6.22). They illustrate the progression of various total force subgroups at each deformation stage. Firstly, there is noticeable growth observed in all Weak, Strong B, and Strong A subgroups, with particular emphasis on the Strong A subgroup. Secondly, both the Strong B and Strong A subgroups experience an initial increase followed by a decline after reaching their peak stages, suggesting occurrences of events and energy release. These patterns are also observable in the linear contact forces (See Figures Figures 6.23-6.25) and compressive parallel bond forces (See Figures 6.26-6.28).

## Total Forces

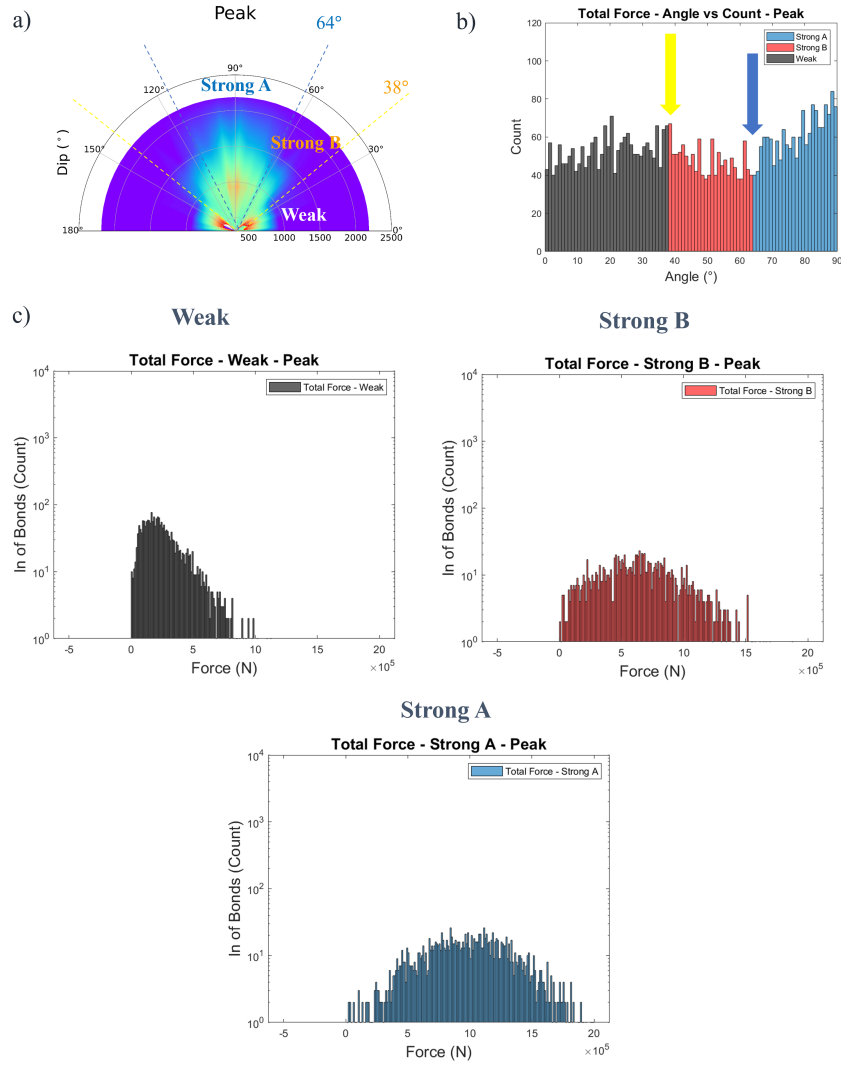


Figure 6.16: Decomposition of total force distribution according to the critical angles at the peak stage. a) The 2D force distribution with critical angles, 38° and 64°, indicated by dashed lines of yellow and blue respectively. b) The angular distribution of forces is colour-coded by different force subgroups according to the critical angles. c) The 1D force distribution of different force subgroups.

Similar patterns are observed in the horizontal subgroup forces of tensile parallel bond forces (Figure 6.29). However, this consistency does not extend to tensile vertical forces (Figure 6.30), where no discernible trend is

## Linear Contact Forces

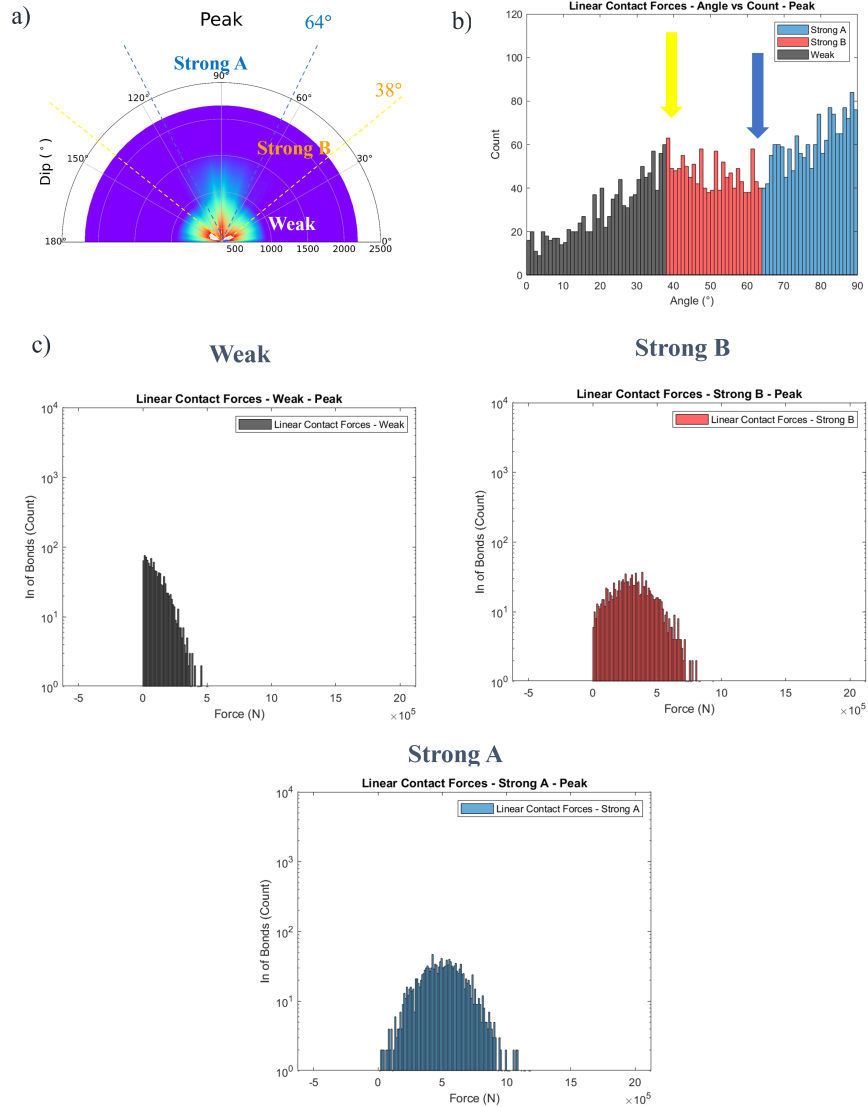


Figure 6.17: Decomposition of linear contact force distribution according to the critical angles at the peak stage. a) The 2D force distribution with critical angles, 38° and 64°, indicated by dashed lines of yellow and blue respectively. b) The angular distribution of forces is colour-coded by different force subgroups according to the critical angles. c) The 1D force distribution of different force subgroups.

evident throughout the deformation stages.

Figures 6.26-6.28 illustrate the evolution of compressive parallel bond

## Compressive Parallel Bond Forces

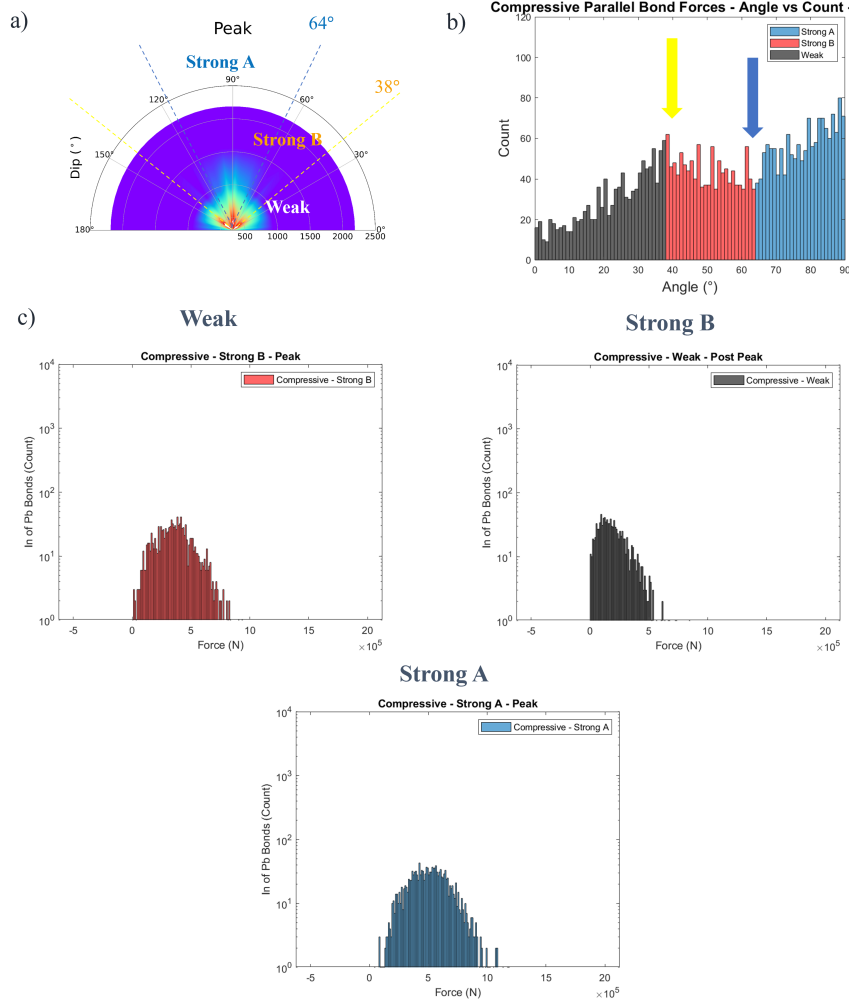


Figure 6.18: Decomposition of compressive parallel bond force distribution according to the critical angles at the peak stage. a) The 2D force distribution with critical angles, 38° and 64°, indicated by dashed lines of yellow and blue respectively. b) The angular distribution of forces is colour-coded by different force subgroups according to the critical angles. c) The 1D force distribution of different force subgroups.

force subgroups, displaying a consistent log-normal distribution across all deformation stages. This distribution pattern is also reflected in the horizontal subgroup of tensile parallel bond forces (Figures 6.30 - 6.29). Additionally, the Strong A and B force subgroups of linear contact forces (Figures

## Tensile Parallel Bond Forces

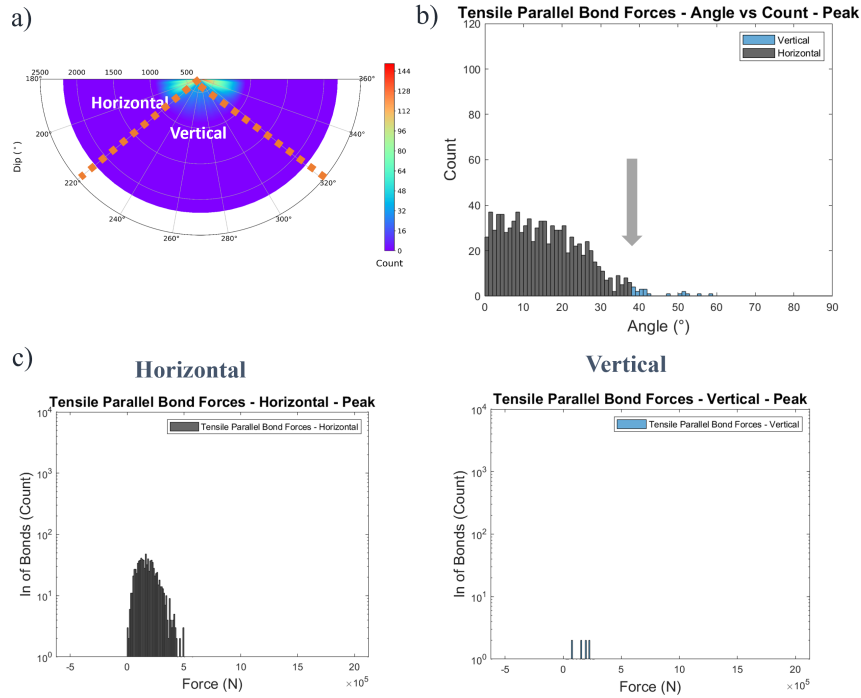


Figure 6.19: Decomposition of tensile parallel bond force distribution according to the critical angles at the peak stage. a) The 2D force distribution with critical angles at  $38^\circ$ , indicated by dashed blue line. b) The angular distribution of forces is colour-coded by different force subgroups according to the critical angles. c) The 1D force distribution of different force subgroups.

6.23 - 6.25) also exhibit a clear log-normal distribution. Consequently, the Strong A and B force subgroups of total forces (Figures 6.20 - 6.22) are similarly pronounced.

When the 1D force subgroups aggregate based on the deformation stages, they assemble to compose the 1D force distribution for each deformation stage, as depicted previously in Figures 6.7, 6.8, 6.9, and 6.10. This integration explains the changes in slope observed in the earlier 1D force distribution plots. The variation in slope, as reported by both the prior study and our research, is essentially a result of the development and cumulative

## Total Forces - **Weak**

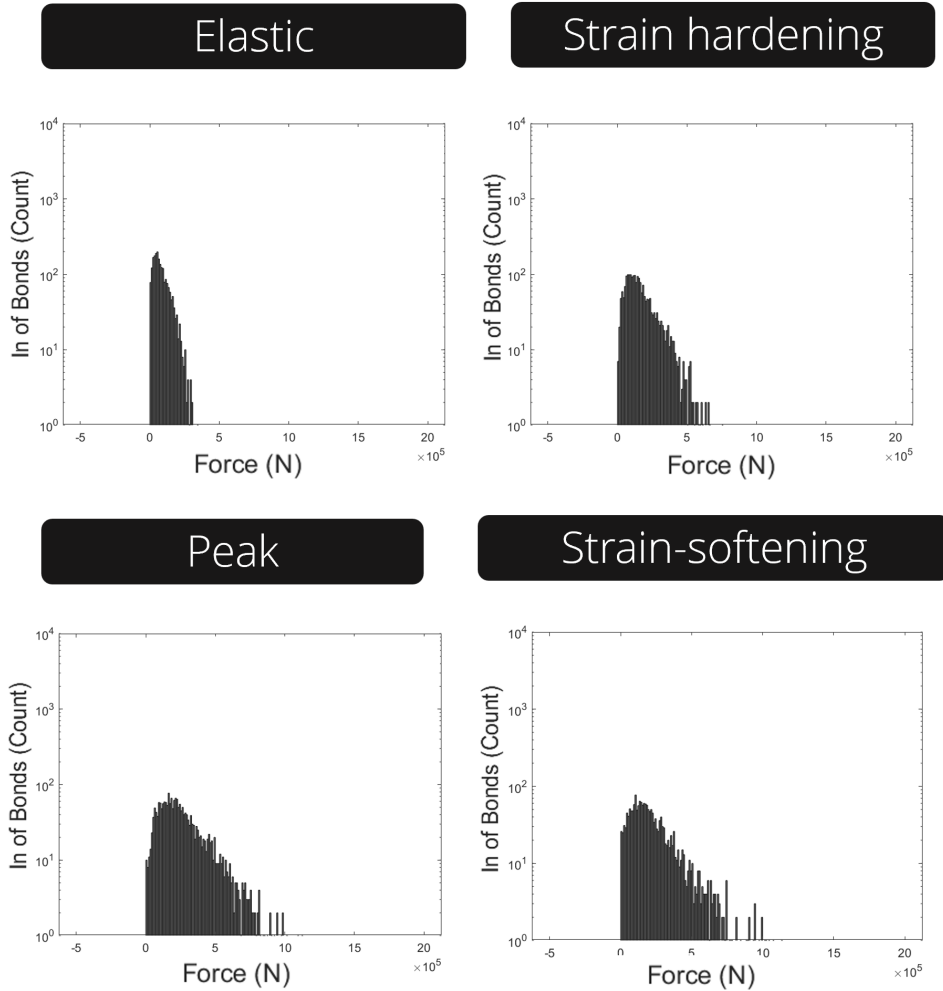


Figure 6.20: The development of the Weak subgroup of total forces throughout the deformation stages: elastic, strain-hardening, peak, and strain-softening.

effect of the force subgroups.

We show that the brittle rock internally comprises five unique force subgroups under compression, three force subgroups in compressive forces regimes and two force subgroups in tensile forces regimes. The Strong force subgroups are confined to compressive forces between specific critical angles and are characterized by their substantial magnitude, setting them apart

## Total Forces - Strong B

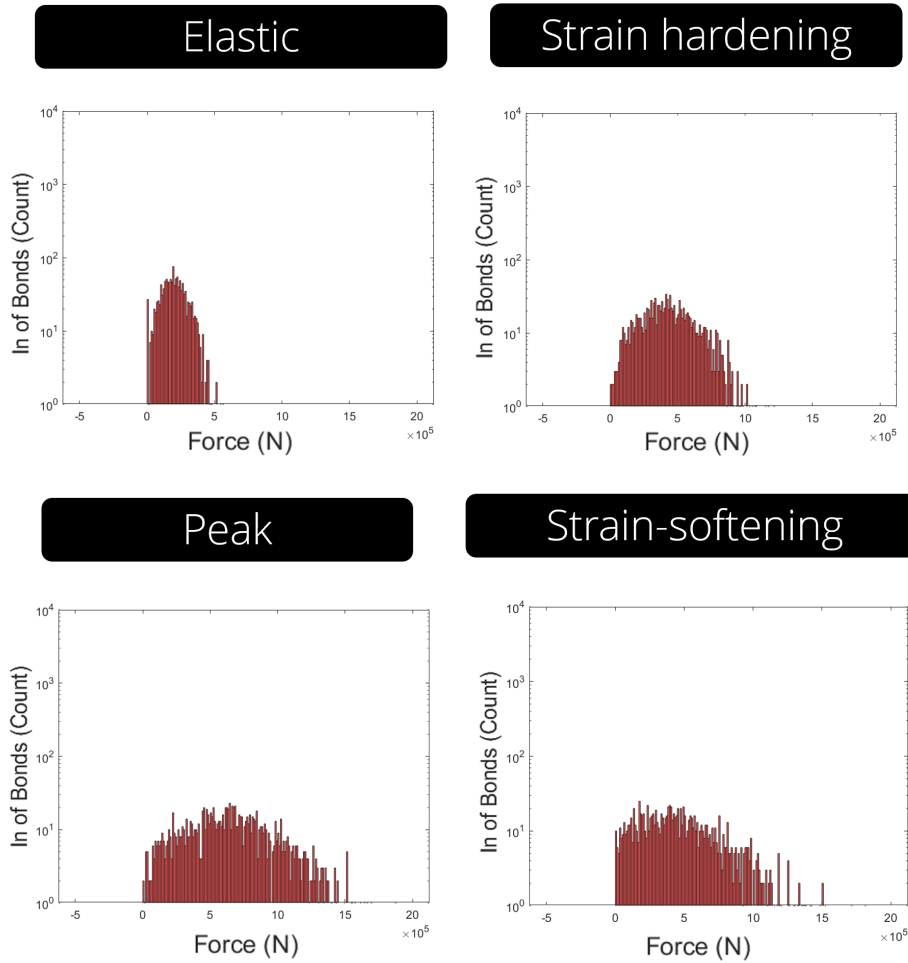


Figure 6.21: The development of the Strong B subgroup of total forces throughout the deformation stages: elastic, strain-hardening, peak, and strain-softening.

from the Weak force subgroup. The Strong force subgroups' growth and decline significantly correlate with the incidence of brittle failure events. Also, we found that the Strong force subgroup heavily depends on the orientation of forces within the bonds. We will continue our exploration of internal force distribution by thoroughly examining the interaction between the crack and internal force networks.

## Total Forces - Strong A

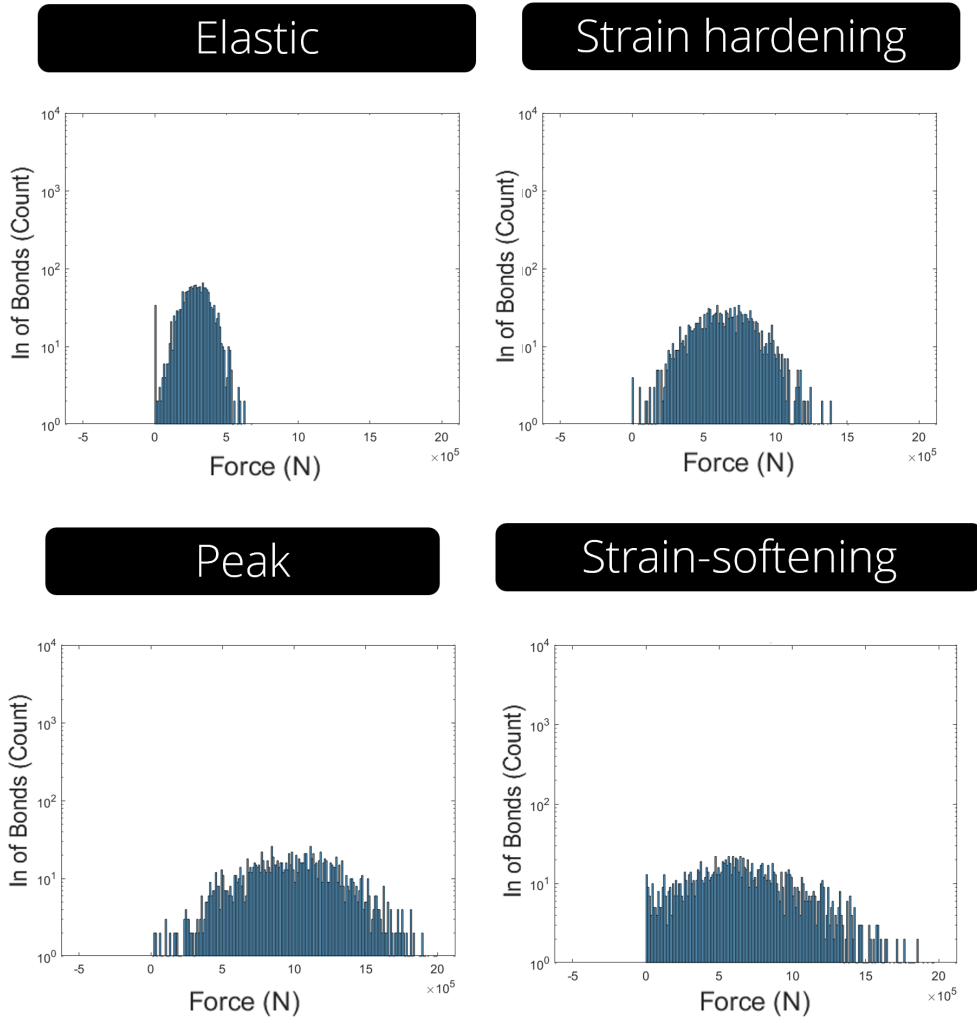


Figure 6.22: The development of the Strong A subgroup of total forces throughout the deformation stages: elastic, strain-hardening, peak, and strain-softening.

### 6.5.3 Relationship between Cracks and Internal Force Networks

For both compressive and tensile forces (Figure 6.31 and 6.32), the linear parallel bonds are evenly distributed at every angle. Figure 6.2 demonstrates a diverse angular distribution of cracks. However, when we separate

## Linear Contact Forces - **Weak**

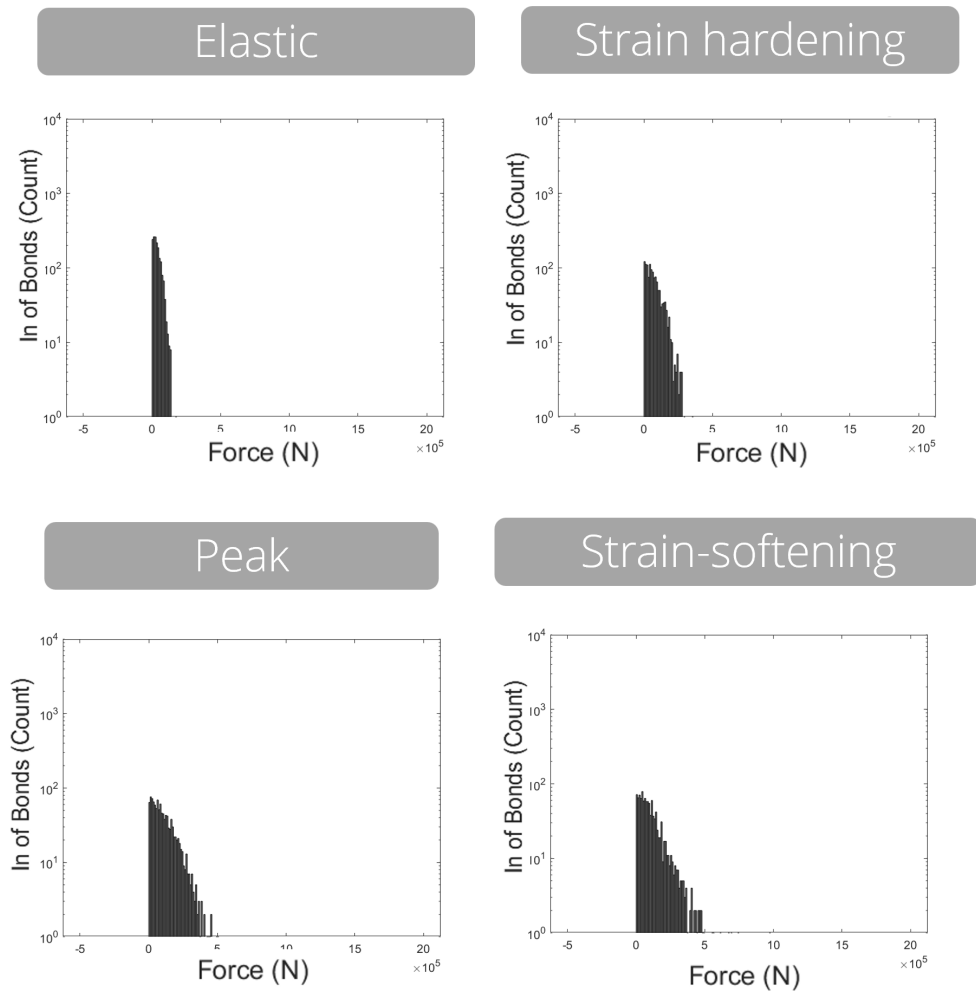


Figure 6.23: The development of the Weak subgroup of linear contact forces throughout the deformation stages: elastic, strain-hardening, peak, and strain-softening.

the cracks based on whether they are shear or tensile, we can see that the cracks also have a strong angular dependency similar to what we found in internal force networks. In contrast, linear parallel bonds are uniformly distributed at every angle with a relatively equal amount.

## Linear Contact Forces - **Strong B**

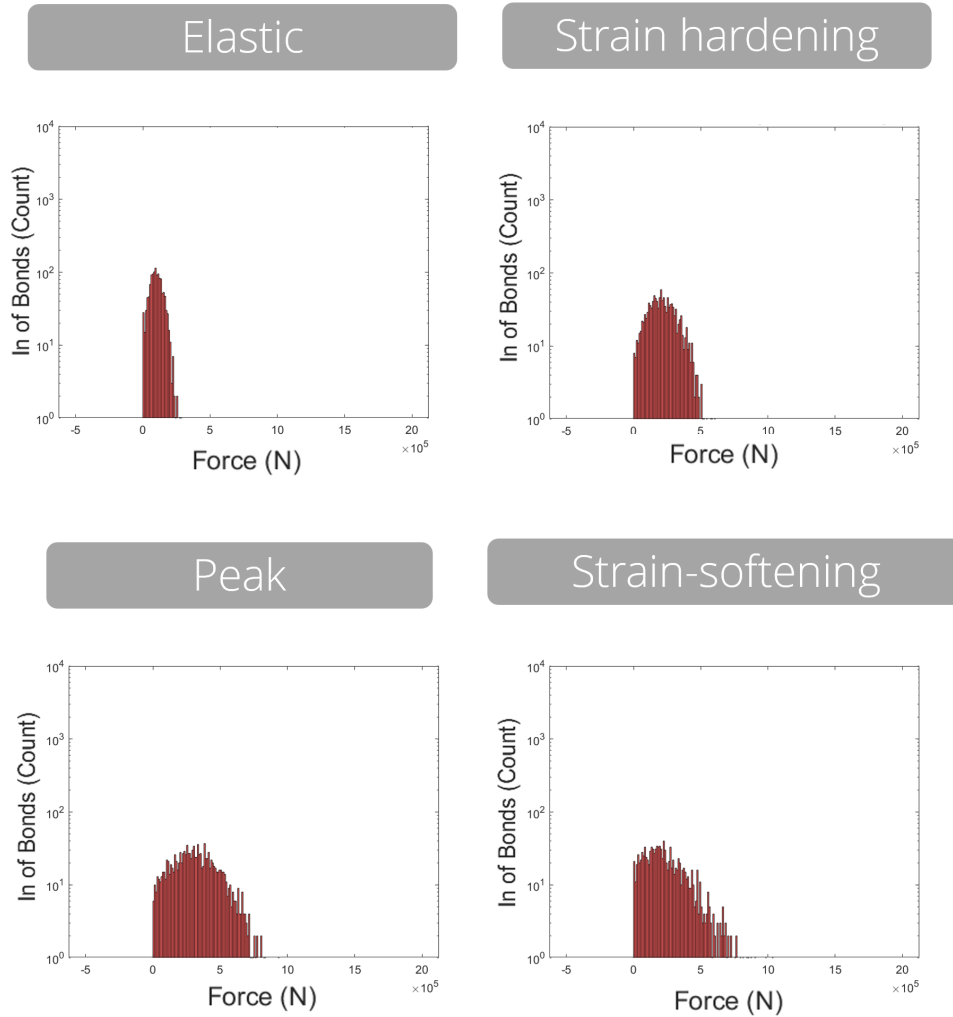


Figure 6.24: The development of the Strong B subgroup of linear contact forces throughout the deformation stages: elastic, strain-hardening, peak, and strain-softening.

### Compressive forces

A comparison between the spatial force distribution (Figure 6.15) and the 2D force distribution (Figure 6.11) graph highlights the shearing plane's angle closely aligning with the force boundaries between Strong A and B in the 2D force plot where a high force gradient is evident. This results

## Linear Contact Forces - **Strong A**

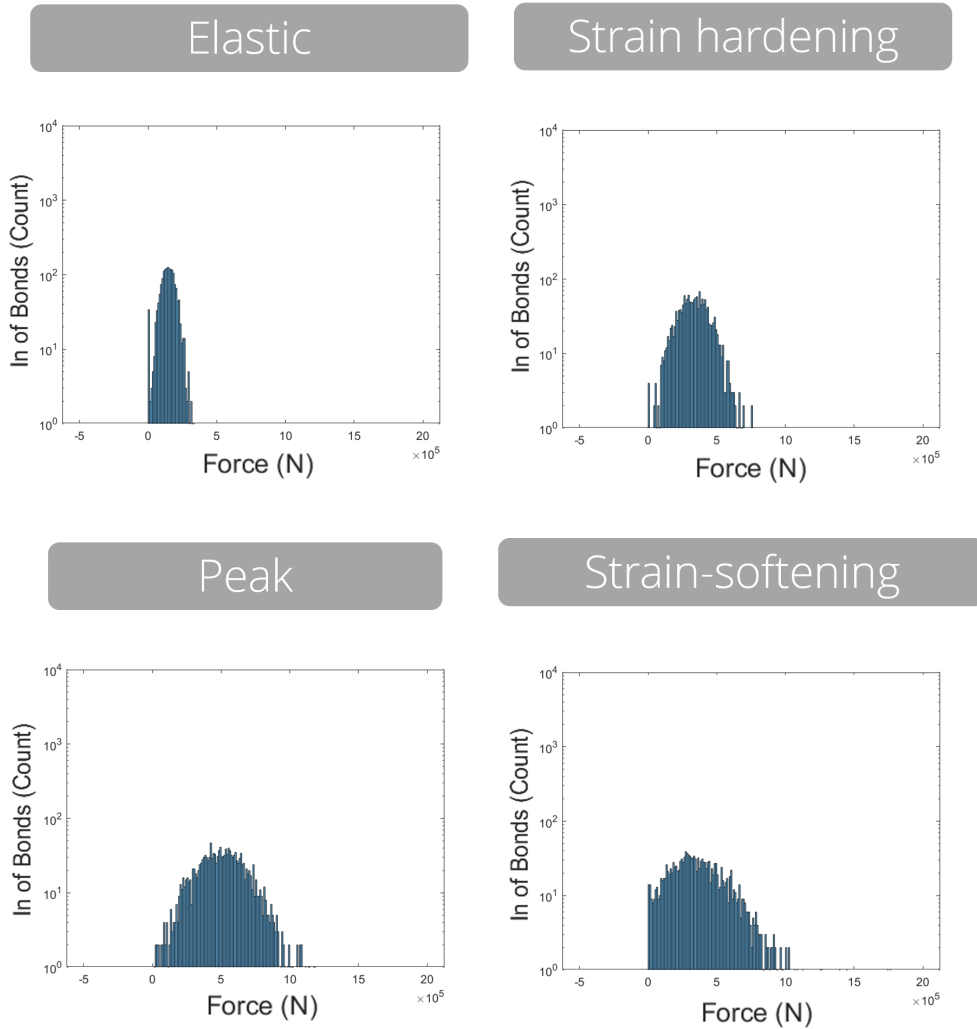


Figure 6.25: The development of the Strong A subgroup of linear contact forces throughout the deformation stages: elastic, strain-hardening, peak, and strain-softening.

in major failures at points where the force gradient is most acute, and the failure plane's angle coincides with the force boundary between Strong A and B force subgroups at  $64^\circ$ . This failure angle is also consistent with the conclusions from the Mohr circle analysis from Chapter 5.

We suggest that the critical angles we previously found in the 2D force

## Compressive Parallel Bond Forces - **Weak**

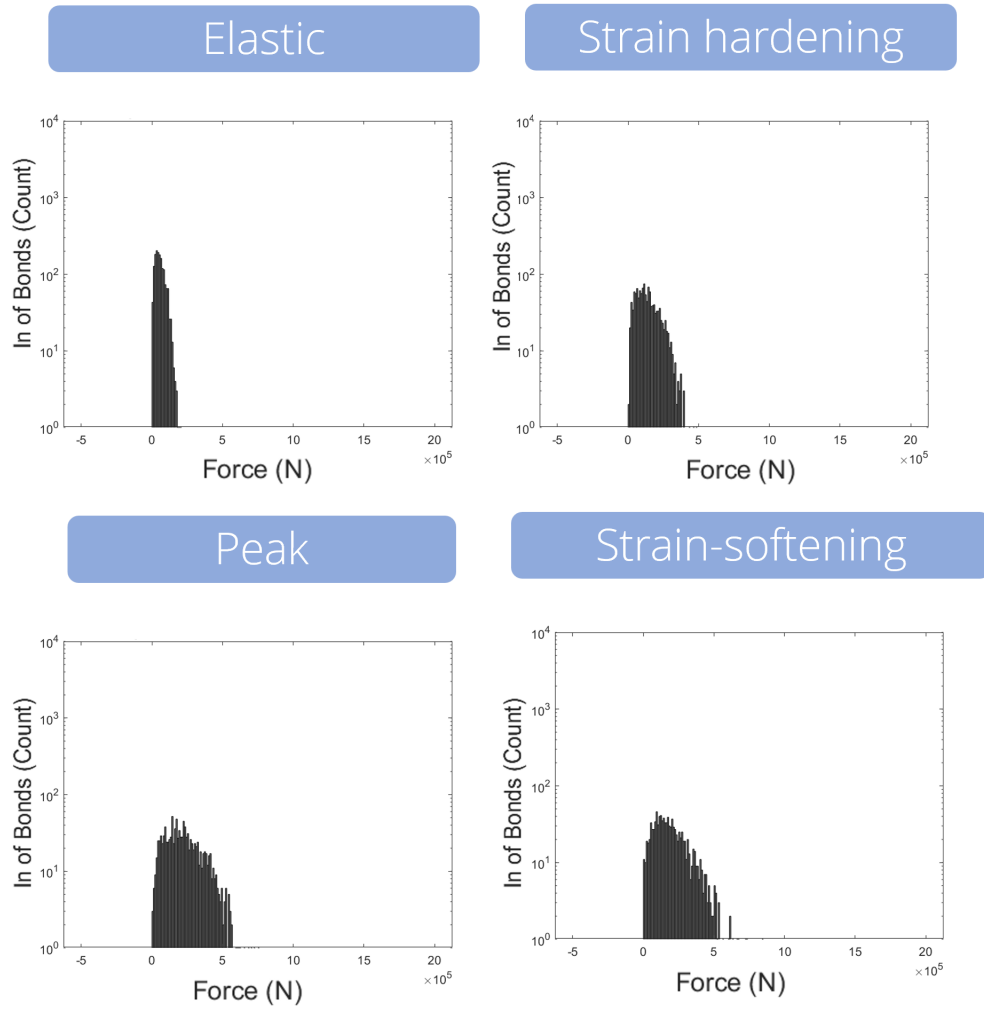


Figure 6.26: The development of the Weak subgroup of compressive parallel bond forces throughout the deformation stages: elastic, strain-hardening, peak, and strain-softening.

distribution are the optimum reactivation angle  $\theta_r^*$  (Sibson, 1990) discussed in Chapter 2.  $\theta_r^* = \frac{1}{2} \tan^{-1}(1/\mu)$ , and from the Mohr Circle Analysis, we obtained that the friction coefficient  $\mu = 0.83$ . Therefore, we can calculate that the optimum reactivation angle for our granite sample is  $25.2^\circ$ . Recall that  $\theta_r^* = 90^\circ - \theta$ ,  $\theta$  represents the angle between failure plane P and  $\sigma_3$ . Therefore,  $\theta$  is  $64.8$ , consistent with the critical angle marking the boundary

## Compressive Parallel Bond Forces - **Strong B**

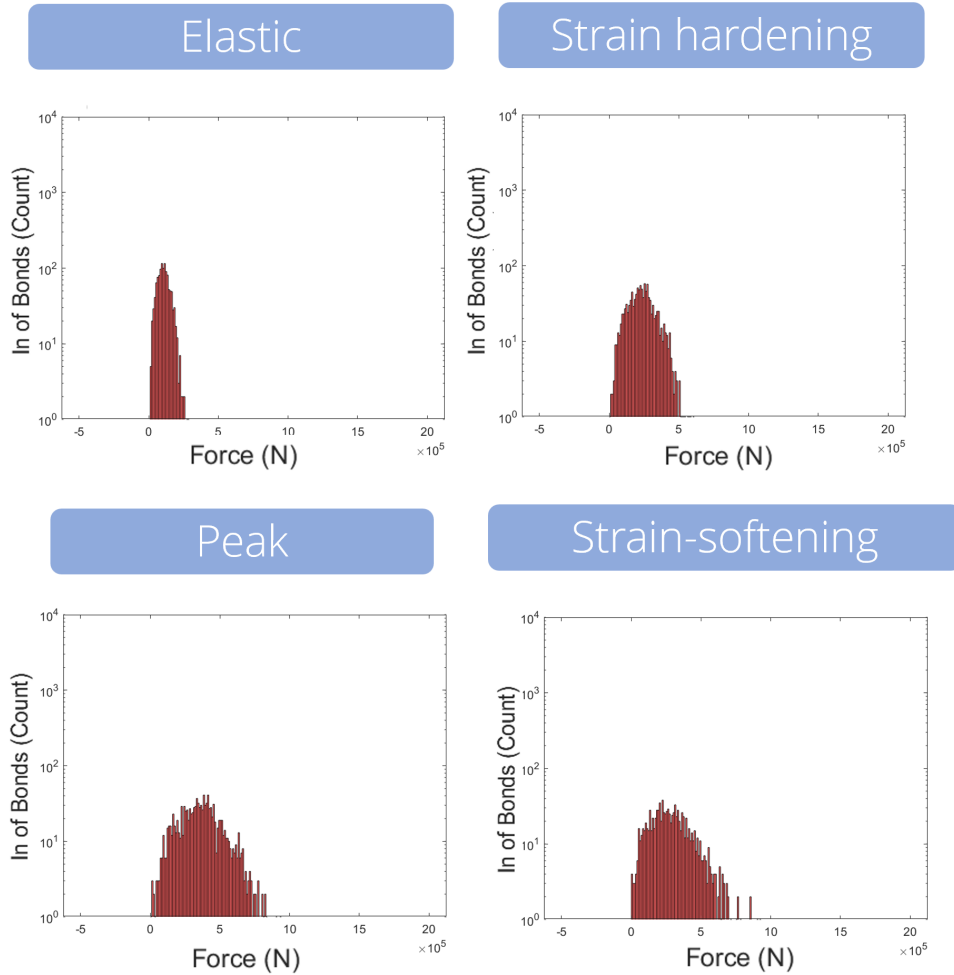


Figure 6.27: The development of the Strong B subgroup of compressive parallel forces throughout the deformation stages: elastic, strain-hardening, peak, and strain-softening.

between Strong A and Strong B subgroups.

Also, recall that when stress ratio  $R = (\sigma_1/\sigma_3)$  reaches infinity when  $\theta_r = 2\theta_r^*$ , so-called the potential "locked-up" angle, indicating that the stress ratio needed for failure plane reactivation goes to infinity. Shearing is unlikely unless the minimum principal stress becomes tensile  $\sigma_3 < 0$  or pore fluid press  $P_f > \sigma_3$ . In our case of friction coefficient  $\mu = 0.83$ , the

## Compressive Parallel Bond Forces -**Strong A**

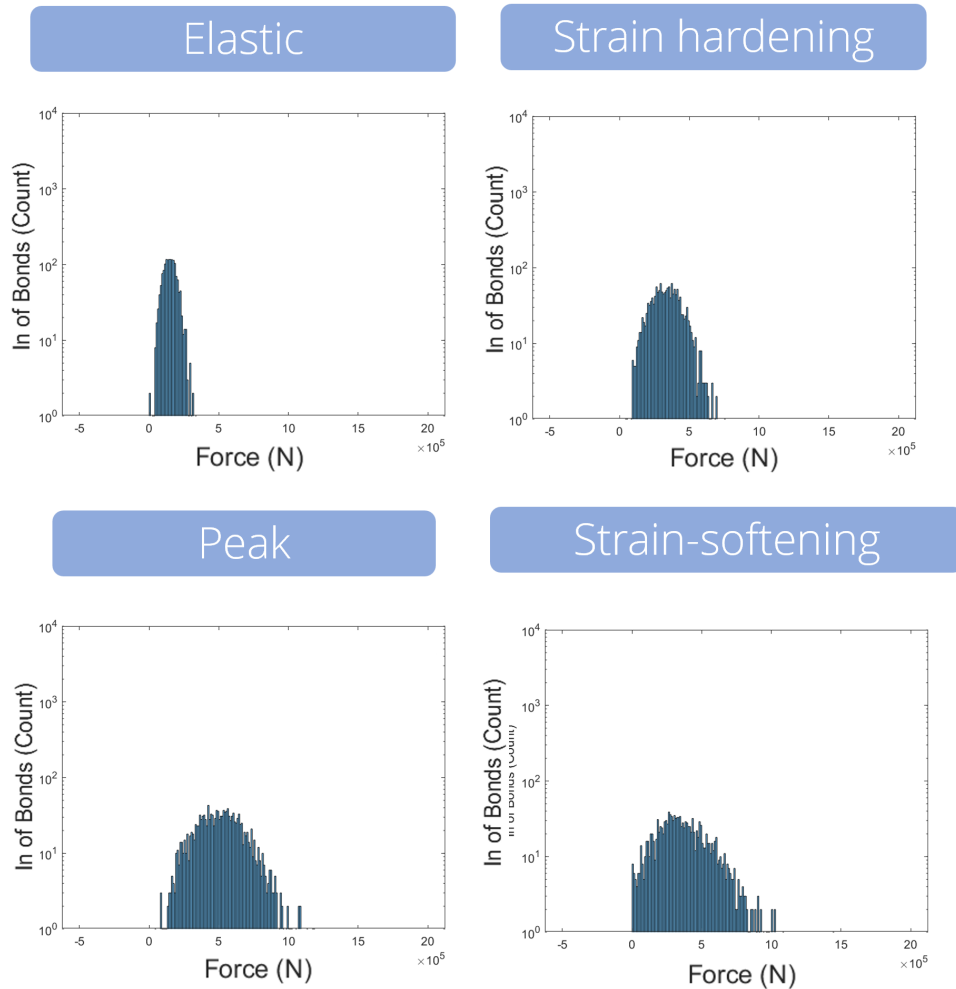


Figure 6.28: The development of the Strong A subgroup of compressive parallel forces throughout the deformation stages: elastic, strain-hardening, peak, and strain-softening.

”locked-up” angle will be  $2\theta_r^* = 2 * 25.2^\circ = 50.4^\circ$ , and the corresponding angle between this ”locked-up” and  $\sigma_3$  is  $39.6^\circ$ , which is also align with the other critical angle at  $38^\circ$  that is between the compressive weak and Strong A force subgroups.

Cracks oriented outside the ”locked-up” angles are considered severely misoriented, requiring an infinity stress ratio  $R$  to induce shearing. Hence,

## Tensile Parallel Bond Forces - **Horizontal**

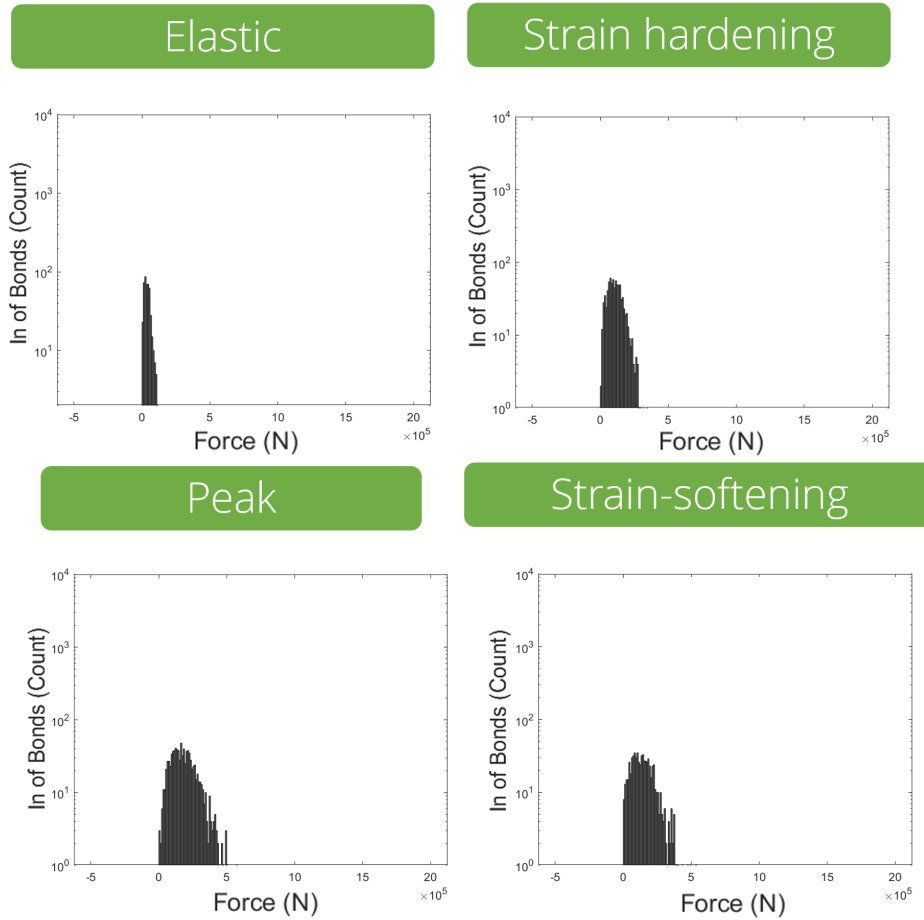


Figure 6.29: The development of the horizontal subgroup of tensile parallel forces throughout the deformation stages: elastic, strain-hardening, peak, and strain-softening.

failure is unlikely to happen if the system remains compressive. Observations from Figure 6.31 corroborate this, showing no evident cracks below this "locked-up" angle, thereby supported by Sibson's theory.

The Strong A subgroup depicted in the 2D force diagrams is the most robust force subgroup, primarily oriented vertically. This is attributed to the necessity for a more substantial force at a higher but unfavourably oriented angle to cause the failure of compressive bonds, resulting in an

## Tensile Parallel Bond Forces - **Vertical**

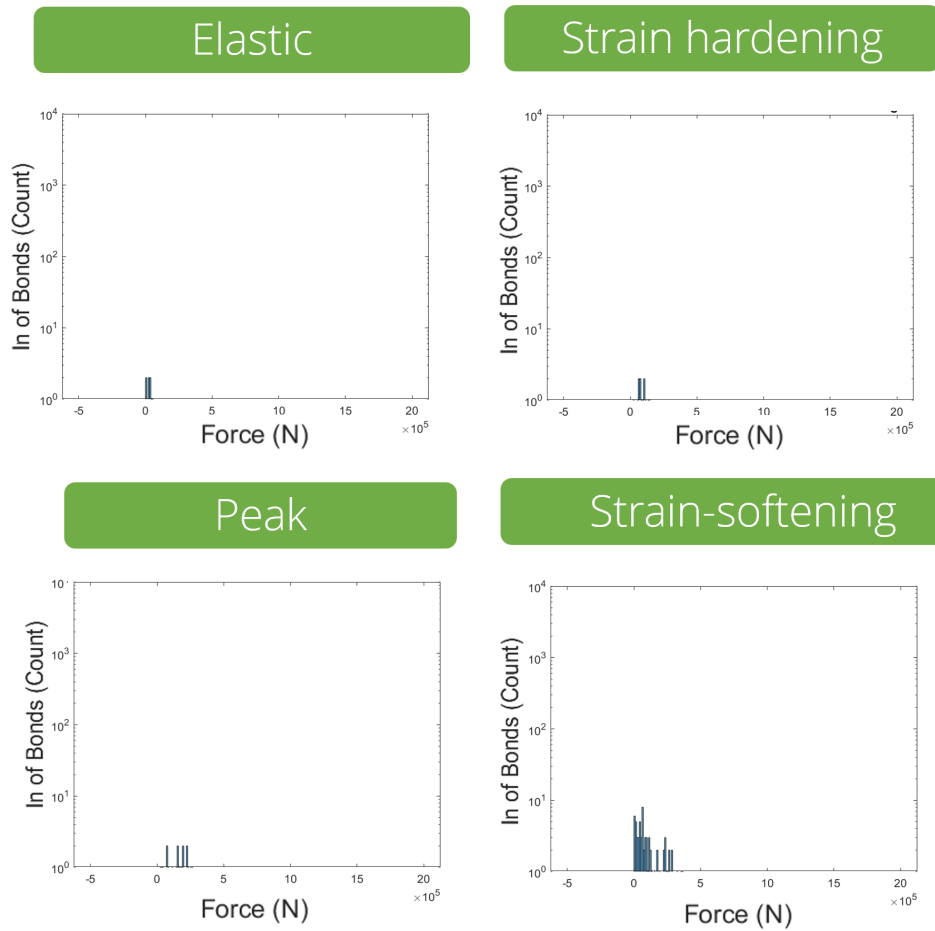


Figure 6.30: The development of the vertical subgroup of tensile parallel forces throughout the deformation stages: elastic, strain-hardening, peak, and strain-softening.

observed escalation of force magnitude from Strong B to Strong A force groups as the angle increases to surpass the critical angle at  $64.8^\circ$ . The spatial distribution of the failure shows that the shearing plane is indicated by a high force gradient and a sudden change in force magnitude; failure is located in relatively weak forces but adjacent to the strong force network. This critical angle of  $64.8^\circ$  separating the Strong B force group from the

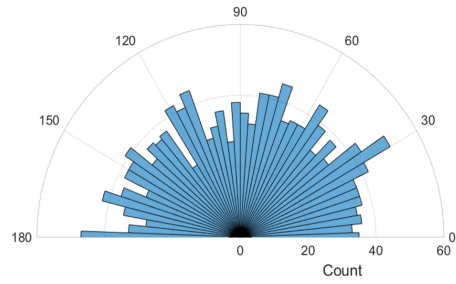
Strong A force group indicates the specific orientation of the highest force gradient and, therefore, predicts the orientation of the final catastrophic failure.

Combining the spatial result of internal force and final failure location ( $64^\circ$ ), 2D force distribution analysis ( $64^\circ$ ), Mohr's circle analysis ( $65^\circ$ ), and Sibson's fault reactivation theory ( $64.8^\circ$ ), it is likely that the critical angles we found are the same as Sibson's fault reactivation theory. The critical angle found between Strong A and B subgroups predicts the orientation of the final catastrophic failure if the loading persistently escalates. Simultaneously, the critical angle observed between the Strong B and Weak force subgroups delineates the foundational angular threshold for the occurrence of shearing.

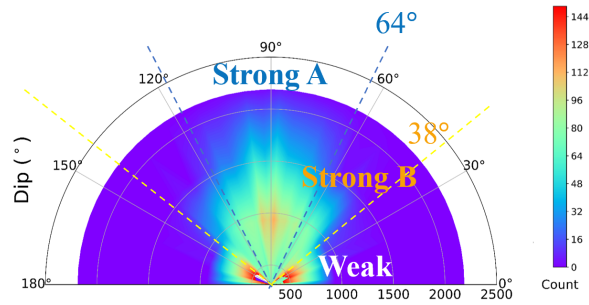
### **Tensile forces**

In scenarios involving tensile forces, those originating solely from parallel bond forces, it appears that forces oriented between  $38^\circ$  and  $142^\circ$  vanish from the 2D force diagram. This absence is attributed to compressive loading, wherein the tensile bonds positioned within the  $38^\circ$  to  $142^\circ$  range are misaligned for the formation of tensile cracks. Bonds oriented horizontally below  $38^\circ$  are more prone to initiating tensile cracks. Consequently, as shown in the tensile crack graph (Figure 6.32), the horizontal force zone below  $38^\circ$  or above  $142^\circ$  predominantly contributes to vertically oriented tensile crack formation. This suggests that tensile crack formation correlates with the collapse of the weak tensile network. The weak tensile forces transpire at any orientation; however, the horizontal segment of the tensile force network, situated below  $38^\circ$  or above  $142^\circ$ , stands out as the primary

### Compressive Bond Orientation and Count



### 2D Total Force Distribution



### Shear Crack Orientation and Count

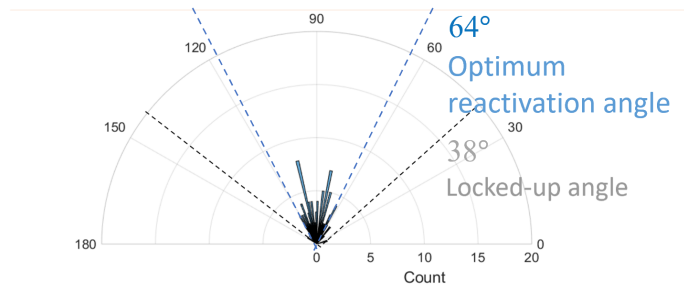
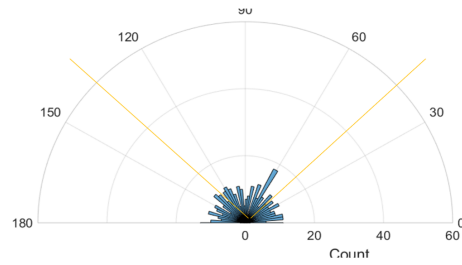


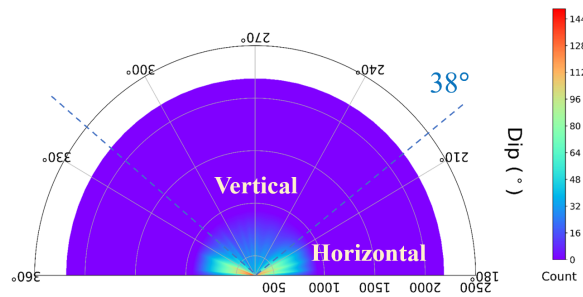
Figure 6.31: Compressive bonds, total forces and shear cracks at the peak phase. Top: Orientation and count of the bonds under compression. Radius represents the count. The azimuth presents the orientation of the linear parallel bond, and the colour represents the count of occurrence. Middle: 2D total force distribution. Radius represents the force magnitude. The azimuth presents the orientation of the force in the linear parallel bond, and the colour represents the count of occurrence. Bottom: Angular distribution of shear cracks. The azimuth presents the orientation of the shear cracks, and the colour represents the count of occurrence.

driver behind the creation of vertically oriented tensile cracks.

### Tensile Bond Orientation and Count



### 2D Tensile Parallel Bond Force Distribution



### Tensile Crack Orientation and Count

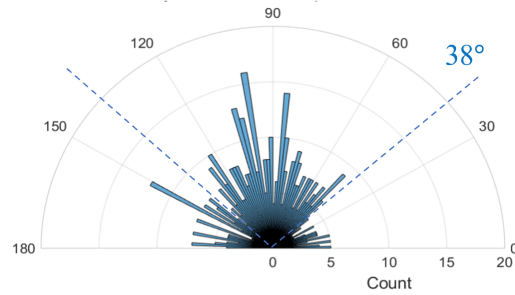


Figure 6.32: Tensile bonds, tensile parallel bond forces and shear cracks at the peak phase. Top: Orientation and count of the bonds under tension. Radius represents the count. The azimuth presents the orientation of the tensile parallel bond, and the colour represents the count of occurrence. Middle: 2D tensile parallel bond force distribution. Radius represents the force magnitude. The azimuth presents the orientation of the force in the linear parallel bond, and the colour represents the count of occurrence. Bottom: Angular distribution of tensile cracks. The azimuth presents the orientation of the tensile cracks, and the colour represents the count of occurrence.

## 6.6 Conclusion

In conclusion, this study comprehensively explores the rock failure and internal force networks in brittle intact rocks, leveraging the bonded particle method. The diligent observation and analysis of crack development and internal force networks illuminated significant insights into the behaviour of rocks under compressive loading. It was observed that the mainshock and largest acoustic emission events notably occur where the stress drop is most substantial. Moreover, identifying five distinct force subgroups within brittle rocks under compression provides a more nuanced understanding of the internal force networks. The analysis of the orientations and magnitudes of these force subgroups and their relationship with crack development substantiates the notion that the orientation and type of forces contribute significantly to the formation of cracks and eventual failure of the rock mass. The critical angles identified in this study align with Sibson's fault reactivation theory, reinforcing the predictive capability of this study for assessing the likelihood of catastrophic failure under continued loading. Understanding the angular dependence of internal forces and its implications on rock failure mechanisms opens avenues for improved predictive models. It reinforces the utility of numerical methods in rock mechanics research, potentially contributing to enhanced safety and efficiency in related fields such as mining, civil engineering, and seismology.

# Chapter 7

## Conclusion

### 7.1 Summary of Results

This thesis demonstrates a progression in geomechanics research, with an emphasis on investigating the mechanisms behind brittle rock failure and the patterns of internal stress. It fills the knowledge gaps of the behavior of internal forces under compressive stresses. This is the final chapter summarizes the contributions of the chapters and possible industrial implications and suggests areas for further research.

Chapter 4 aims to verify the bonded particle method (BPM) as a reliable tool for simulating the complex behavior of brittle rocks under compression. The contributions of this chapter are:

1. Bridging theory and practice by combining both numerical and analytical/semi-analytical methods to validate the bonded particle method.
2. Proving BPM reliability by focusing on the simulation of elastic wave propagation. This chapter demonstrates the BPM's capability to replicate real-world phenomena accurately. This verification process

increases the reliability of BPM for future research and practical applications in rock failure analysis.

Chapter 5 focuses on using the bonded particle method (BPM) to model the behaviour of Lac du Bonnet granite, a well-documented rock material. The main goal of this chapter is to describe the material generation process and calibrate the model for the following simulations. The contributions of this chapter are:

1. Outlining the detailed procedure for creating a Particle Flow Code (PFC) 2D model of the Lac du Bonnet granite.
2. Providing micro-mechanical parameters to match the physical properties and behavior of Lac du Bonnet granite.

Chapter 6 represents the cumulative effort to explore complex rock failure mechanisms and internal force networks in brittle rocks. This chapter advances the understanding of internal force networks:

1. Identifying the characteristics of a catastrophic failure. We found that catastrophic failure occurs after peak stress is reached, accompanied by the most significant stress drop, the largest acoustic emission size, the highest crack formation rate, the highest acoustic emission rate, and the highest shear-tensile crack ratio.
2. Five distinct subgroups of forces within the overall internal force distribution are discovered: Weak, Strong A, Strong B, horizontal and vertical force subgroups. This distinction allows for a detailed analysis of the forces and contributes to a further understanding of their individual and collective effects on rock failure. This chapter also

determines the critical angles separating the boundaries between the identified force subgroups.

3. Determine the relationship between internal forces and catastrophic failure. Failure occurs in regions with high force gradients, oriented according to the critical angle that is between the Strong A and B subgroups. Therefore, this critical value can predict the orientation of catastrophic failure. At the same time, the critical angle observed between the Strong B force subgroup and the Weak force subgroup shows the angular threshold of shearing. This insight is important for predicting failures in geotechnical applications and designing interventions that enhance rock stability.

## **7.2 Industry Implications**

1. Predicting Catastrophic Failure in Mining, Hydraulic Fracturing and Geothermal Extraction. The identification of catastrophic failure characteristics, such as stress-drop conditions and acoustic emission rates which can be measured and monitored on the field, can improve monitoring systems within geotechnical operations. This enables the prediction and prevention of collapses or other hazardous incidents, thereby safeguarding workers and infrastructure.
2. Optimizing Resource Extraction Techniques. Given that catastrophic failure occurs in areas of high force gradients at specific critical angles, intentionally creating minor geological weaknesses away from these critical angles could optimize extraction processes in the oil, gas, and geothermal sectors. This approach enhances both stability and safety.

By focusing on the strategic targeting of weak points for extraction. Utilizing this insight to develop innovative strategies can decrease operational costs and boost efficiency while ensuring safe operations.

3. Mitigating Induced Seismicity. The relationship between internal forces and catastrophic failure, especially the orientation of failure according to critical angles, is crucial for industries that induce stress in the crust, such as hydraulic fracturing and geothermal energy extraction. By predicting the orientation and conditions of potential failure, these industries can adjust their operations to mitigate the risks of induced seismicity. Therefore protecting nearby communities and infrastructure.
4. Guiding Environmental and Regulatory Policies. These insights can guide environmental and regulatory policies by identifying the conditions that could lead to rock failure and pose potential risks. This knowledge can help to reduce environmental impacts, particularly in ecologically sensitive regions and populated areas.

### **7.3 Suggested future research**

Still, a more comprehensive analysis is required to further understand the failure mechanism and internal forces. Here, we outline some potential directions for future investigation:

1. Extension to Three-Dimensional Modeling. The current study primarily utilizes two-dimensional BPM simulations to explore the behavior of brittle rocks under stress. Future research could extend

these simulations to three-dimensional models, offering a more comprehensive understanding of the spatial complexities involved in rock failure. Three-dimensional modeling would provide insights into out-of-plane forces and fracture propagation paths that are not captured in two-dimensional simulations, enhancing the predictive accuracy of rock failure mechanisms.

2. Investigation of Anisotropic Rock Behavior. Rocks in nature often exhibit anisotropic mechanical properties due to their formation processes, mineral composition, and existing stress fields (Garcia-Teijeiro and Rodriguez-Herrera, 2014). Future studies could focus on incorporating anisotropy into BPM simulations to investigate its impact on rock failure behavior. Understanding how anisotropy influences crack initiation, propagation, and the distribution of internal forces would contribute to more accurate models of natural rock behavior.
3. Integration with Machine Learning Techniques. The integration of machine learning techniques with BPM simulations presents an exciting avenue for future research. Machine learning algorithms could be employed to analyze simulation data, identify patterns in rock failure mechanisms, and predict rock behavior under various loading conditions. This approach could significantly enhance the efficiency and accuracy of geomechanical models, paving the way for real-time monitoring and predictive analytics in geotechnical applications.
4. Experimental Validation Under Dynamic Loading Conditions. While this thesis provides a thorough experimental validation of BPM under static loading conditions, future research could explore the behavior

of brittle rocks under dynamic loading conditions. This would involve conducting experiments to simulate seismic events, shock loading, and other transient stress conditions. Such studies would offer valuable insights into the rock's response to dynamic stresses (Hulse, 1959), which is relevant for understanding natural hazards like earthquakes.

5. Exploration of Fluid-Rock Interactions. The interaction between fluids and rock plays a critical role in many geotechnical processes, including hydraulic fracturing and enhanced geothermal systems. Future research could focus on simulating fluid-rock interactions using BPM to investigate how fluid pressure, flow rate, and fluid properties influence rock failure and fracture propagation. This research would be particularly relevant for optimizing hydraulic fracturing techniques and understanding subsurface fluid migration.
6. Studies on Rock Failure Mitigation Strategies. Future research could focus on designing and evaluating rock failure mitigation strategies. This could include the development of novel rock bolting techniques, the use of engineered fluids to stabilize fractures, or the application of external stress fields to prevent failure. Such studies would have direct implications for improving the safety and sustainability of geotechnical operations.

# Bibliography

- Aki, K., and P. G. Richards, 2002, Quantitative seismology: University Science Books.
- Al-Ajmi, A. M., and R. W. Zimmerman, 2006, Stability analysis of vertical boreholes using the mogi–coulomb failure criterion: *International Journal of Rock Mechanics and Mining Sciences*, **43**, 1200–1211.
- Al-Busaidi, A., J. F. Hazzard, and R. P. Young, 2005, Distinct element modeling of hydraulically fractured lac du bonnet granite: *Journal of Geophysical Research: Solid Earth*, **110**.
- Ashby, M., and C. Sammis, 1990, The damage mechanics of brittle solids in compression: *Pure and applied geophysics*, **133**, 489–521.
- Bao, X., and D. W. Eaton, 2016, Fault activation by hydraulic fracturing in western canada.: Science.
- Barton, N., 1976, The shear strength of rock and rock joints: *International Journal of rock mechanics and mining sciences & Geomechanics abstracts*, Elsevier, 255–279.
- Bobet, A., and H. H. Einstein, 1998, Numerical modeling of fracture coalescence in a model rock material: *International Journal of Fracture*, **92**, 221–252.
- Brace, W., and E. Bombolakis, 1963, A note on brittle crack growth in compression: *Journal of Geophysical Research*, **68**, 3709–3713.

- Brace, W., B. Paulding Jr, and C. Scholz, 1966, Dilatancy in the fracture of crystalline rocks: *Journal of geophysical research*, **71**, 3939–3953.
- Brodsky, E. E., V. Karakostas, and H. Kanamori, 2000, A new observation of dynamically triggered regional seismicity: Earthquakes in greece following the august 1999 izmit, turkey earthquake: *Geophysical Research Letters*, **27**, 2741–2744.
- Burdekin, F. M., and D. Stone, 1966, The crack opening displacement approach to fracture mechanics in yielding materials: *Journal of Strain Analysis*, **1**, 145–153.
- Byerlee, J., 1978, Friction of rocks, *in* *Rock friction and earthquake prediction*: Springer, 615–626.
- Byerlee, J. D., 1967, Frictional characteristics of granite under high confining pressure: *Journal of Geophysical Research*, **72**, 3639–3648.
- Camones, L. A. M., E. do Amaral Vargas, R. P. de Figueiredo, and R. Q. Velloso, 2013, Application of the discrete element method for modeling of rock crack propagation and coalescence in the step-path failure mechanism: *Engineering Geology*.
- Chester, J. S., and R. C. Fletcher, 1997, Stress distribution and failure in anisotropic rock near a bend on a weak fault: *Journal of Geophysical Research: Solid Earth*, **102**, 693–708.
- Cho, N. a., C. Martin, and D. Segol, 2007, A clumped particle model for rock: *International journal of rock mechanics and mining sciences*, **44**, 997–1010.
- Cipolla, C., and C. Wright, 2000, Diagnostic techniques to understand hydraulic fracturing: what? why? and how?: Presented at the SPE/CERI Gas Technology Symposium, OnePetro.

- Clarke, H., L. Eisner, P. Styles, and P. A. Turner, 2014, Felt seismicity associated with shale gas hydraulic fracturing: The first documented example in Europe: *Geophysical Research Letters*.
- Costin, L., 1983, A microcrack model for the deformation and failure of brittle rock: *Journal of Geophysical Research: Solid Earth*, **88**, 9485–9492.
- , 1985, Damage mechanics in the post-failure regime: *Mechanics of Materials*, **4**, 149–160.
- Cundall, P. A., and R. D. Hart, 1992, Numerical modelling of discontinua: *Engineering Computations*.
- Cundall, P. A., and O. D. L. Strack, 1979a, A discrete numerical model for granular assemblies: *Géotechnique*, **29**, 47–65.
- , 1979b, A discrete numerical model for granular assemblies: *Géotechnique*, **29**, 47–65.
- Dey, T., and C.-Y. Wang, 1981, Some mechanisms of microcrack growth and interaction in compressive rock failure: *International Journal of Rock Mechanics and Mining Sciences & Geomechanics Abstracts*, Elsevier, 199–209.
- Donzé, F.-V., J. Bouchez, and S.-A. Magnier, 1997, Modeling fractures in rock blasting: *International Journal of Rock Mechanics and Mining Sciences*.
- Dyskin, A., and E. Sahouryeh, 1997, Mechanism of dilatancy and fracture of brittle materials in uniaxial compression: *International Journal of Fracture*, **86**, L45–L50.
- Ellsworth, W. L., 2013, Injection-induced earthquakes: *Science*.
- Engelder, T., and S. Marshak, 1988, Analysis of data from rock-deformation

- experiments: *Basic Methods of Structural Geology*, 193–212.
- Fairhurst, C., and N. Cook, 1966, The of maximum phenomenon of rock splitting parallel to the direction compression in the neighbourhood of a surface: Presented at the 1st ISRM Congress, OnePetro.
- Fakhimi, A., and T. Villegas, 2007, Application of dimensional analysis in calibration of a discrete element model for rock deformation and fracture: *Rock Mechanics and Rock Engineering*, **40**, 193–211.
- Fink, J., 2013, *Hydraulic fracturing chemicals and fluids technology*: Gulf Professional Publishing.
- Garcia-Teijeiro, X., and A. Rodriguez-Herrera, 2014, Dependence of stress-induced micro-seismicity on natural fracture properties and in-situ stress: SPE Canada Unconventional Resources Conference?, SPE, D031S010R004.
- Gibowicz, S. J., 1994, *An introduction to mining seismology*: International Geophysics.
- Griffith, A., 1924, The theory of rupture: *First Int. Cong. Appl. Mech.*, 55–63.
- Griffith, A. A., 1921, Vi. the phenomena of rupture and flow in solids: *Philosophical transactions of the royal society of london. Series A, containing papers of a mathematical or physical character*, **221**, 163–198.
- Groenenboom, J., and D. B. V. Dam, 2000, Monitoring hydraulic fracture growth: Laboratory experiments: *Geophysics*, **65**, 603–611.
- Hadi, Haeri, Kouros, Shahriar, Mohammad, Fatehi, Marji, Parviz, and Moarefvand, 2014, Cracks coalescence mechanism and cracks propagation paths in rock-like specimens containing pre-existing random cracks under compression: *Journal of Central South University*.

- Hazzard, J., and R. P. Young, 2004, Dynamic modelling of induced seismicity: *International Journal of Rock Mechanics and Mining Sciences*, **41**, 1365–1376.
- Hazzard, J. F., and R. P. Young, 2002, Moment tensors and micromechanical models: *Tectonophysics*, **356**, 181–197.
- Hazzard, J. F., R. P. Young, and S. C. Maxwell, 2000, Micromechanical modeling of cracking and failure in brittle rocks: *Journal of Geophysical Research: Solid Earth*, **105**, 16683–16697.
- Hill, D. P., P. Reasenber, A. Michael, W. Arabaz, G. Beroza, D. Brumbaugh, J. Brune, R. Castro, S. Davis, D. dePolo, et al., 1993, Seismicity remotely triggered by the magnitude 7.3 landers, california, earthquake: *Science*, **260**, 1617–1623.
- Hobbs, D., 1966, A study of the behaviour of a broken rock under triaxial compression, and its application to mine roadways: *International Journal of Rock Mechanics and Mining Sciences & Geomechanics Abstracts*, Elsevier, 11–43.
- Hoek, E., 1968, Brittle fracture of rock: *Rock mechanics in engineering practice*, **130**.
- Hoek, E., and Z. Bieniawski, 1965, Brittle fracture propagation in rock under compression: *International Journal of Fracture Mechanics*, **1**, 137–155.
- Hokka, M., J. Black, D. Tkalich, M. Fourmeau, A. Kane, N.-H. Hoang, C. Li, W. Chen, and V.-T. Kuokkala, 2016, Effects of strain rate and confining pressure on the compressive behavior of kuru granite: *International Journal of Impact Engineering*, **91**, 183–193.
- Horii, H., and S. Nemat-Nasser, 1983, Overall moduli of solids with micro-

- cracks: load-induced anisotropy: *Journal of the Mechanics and Physics of Solids*, **31**, 155–171.
- Hulse, D. S., 1959, Fracturing process with superimposed cyclic pressure. (US Patent 2,915,122).
- Hunt, S., A. Meyers, and V. Louchnikov, 2003, Modelling the kaiser effect and deformation rate analysis in sandstone using the discrete element method: *Computers and Geotechnics*.
- Ibrahimbegovic, A., 2009, *Nonlinear solid mechanics: theoretical formulations and finite element solution methods*: Springer Science & Business Media.
- Irwin, G. R., 1957, Analysis of stresses and strains near the end of a crack traversing a plate.
- , 1960, *Fracture mechanics: Presented at the Structural mechanics: Proceedings of the First Symposium on Naval Structural Mechanics*, Pergamon.
- Itasca Consulting Group, I., 2008, Pfc2d — particle flow code in 2 dimensions, version 4.0, user’s manual.
- Ivars, D. M., M. E. Pierce, C. Darcel, J. Reyes-Montes, D. O. Potyondy, R. P. Young, and P. A. Cundall, 2011, The synthetic rock mass approach for jointed rock mass modelling: *International Journal of Rock Mechanics and Mining Sciences*, **48**, 219–244.
- Jing, L., and J. Hudson, 2002, Numerical methods in rock mechanics: *International Journal of Rock Mechanics and Mining Sciences*, **39**, 409–427.
- Kanamori, H., 1977, The energy release in great earthquakes: *Journal of geophysical research*, **82**, 2981–2987.
- , 1978, Quantification of earthquakes: *Nature*, **271**, 411–414.

- Kanamori, H., and E. E. Brodsky, 2004, The physics of earthquakes: Reports on Progress in Physics, **67**, 1429.
- Kazerani, T., and J. Zhao, 2010, Micromechanical parameters in bonded particle method for modelling of brittle material failure: International journal for numerical and analytical methods in geomechanics, **34**, 1877–1895.
- Kelly, D., D. Peck, and R. James, 1993, Petrography of granitic rock samples from the 420 level of the underground research laboratory, pinawa, manitoba: Department of Geology, Laurentian University, Sudbury, Ontario.
- Keranen, K. M., and M. Weingarten, 2018, Induced seismicity: Annual Review of Earth and Planetary Sciences.
- Khazaei, C., J. Hazzard, and R. Chalaturnyk, 2015, Damage quantification of intact rocks using acoustic emission energies recorded during uniaxial compression test and discrete element modeling: Computers and Geotechnics.
- Kondic, L., A. Goulet, C. O’Hern, M. Kramar, K. Mischaikow, and R. Behringer, 2012, Topology of force networks in compressed granular media: EPL (Europhysics Letters), **97**, 54001.
- Krajcinovic, D., 1995, Continuum damage mechanics: when and how?: International Journal of Damage Mechanics, **4**, 217–229.
- Labuz, J. F., S. Cattaneo, and L. H. Chen, 2001, Acoustic emission at failure in quasi-brittle materials: Construction and Building Materials.
- Lajtai, E., 1971, A theoretical and experimental evaluation of the griffith theory of brittle fracture: Tectonophysics, **11**, 129–156.
- Lajtai, E., B. Carter, and M. Ayari, 1989, Criteria for brittle fracture in

- compression.
- Lee, W. H. K., 2002, International handbook of earthquake and engineering seismology: Academic Press eBooks.
- Li, X., X. Lei, Q. Li, and X. Li, 2017, Experimental investigation of sinian shale rock under triaxial stress monitored by ultrasonic transmission and acoustic emission: *Journal of Natural Gas Science and Engineering*.
- Liu, C.-h., S. R. Nagel, D. Schecter, S. Coppersmith, S. Majumdar, O. Narayan, and T. Witten, 1995, Force fluctuations in bead packs: *Science*, **269**, 513–515.
- Lockner, D. A., 1993, The role of acoustic emission in the study of rock fracture: *International Journal of Rock Mechanics and Mining Sciences & Geomechanics Abstracts*.
- Martin, C., 1993, Strength of massive lac du bonnet granite around underground openings, phd thesis, university of manitoba, winnipeg.
- Mas Ivars, D., D. Potyondy, M. Pierce, and P. Cundall, 2008, The smooth-joint contact model: *Proceedings of WCCM8-ECCOMAS*, **2008**, 8th.
- Maxwell, S., 2014, Microseismic imaging of hydraulic fracturing: Improved engineering of unconventional shale reservoirs: *Society of Exploration Geophysicists*.
- Mogi, K., 1974, On the pressure dependence of strength of rocks and the coulomb fracture criterion: *Tectonophysics*, **21**, 273–285.
- Murrell, S. A. F., 1965, The effect of triaxial stress systems on the strength of rocks at atmospheric temperatures: *Geophysical Journal International*, **10**, 231–281.
- Nikolić, M., T. Roje-Bonacci, and A. Ibrahimbegović, 2016, Overview of the numerical methods for the modelling of rock mechanics problems.:

- Tehnicki vjesnik/Technical Gazette, **23**.
- Okui, Y., and H. Horii, 1995, A micromechanics-based continuum theory for microcracking localization of rocks under compression: Continuum models for materials with microstructure. New York: Wiley (1995): 27-68.
- Patton, F. D., et al., 1966, Multiple modes of shear failure in rock: Presented at the 1st ISRM Congress, International Society for Rock Mechanics and Rock Engineering.
- Potyondy, D., 2014, Material-modeling support in pfc: Minneapolis, Minnesota, USA.
- Potyondy, D., P. Cundall, C. Lee, et al., 1996, Modelling rock using bonded assemblies of circular particles: Presented at the 2nd North American rock mechanics symposium, American Rock Mechanics Association.
- Potyondy, D., et al., 2012a, A flat-jointed bonded-particle material for hard rock: Presented at the 46th US rock mechanics/geomechanics symposium, American Rock Mechanics Association.
- , 2012b, A flat-jointed bonded-particle material for hard rock: Presented at the 46th US rock mechanics/geomechanics symposium, American Rock Mechanics Association.
- Radjai, F., M. Jean, J.-J. Moreau, and S. Roux, 1996, Force distributions in dense two-dimensional granular systems: Physical review letters, **77**, 274.
- Radjai, F., S. Roux, and J. J. Moreau, 1999, Contact forces in a granular packing: Chaos: An Interdisciplinary Journal of Nonlinear Science, **9**, 544–550.
- Radjai, F., D. E. Wolf, M. Jean, and J.-J. Moreau, 1998, Bimodal character

- of stress transmission in granular packings: *Physical review letters*, **80**, 61.
- Rawling, G. C., P. Baud, and T.-f. Wong, 2002, Dilatancy, brittle strength, and anisotropy of foliated rocks: Experimental deformation and micromechanical modeling: *Journal of Geophysical Research: Solid Earth*, **107**, ETG-8.
- Read, R., and C. Martin, 1996, Technical summary of aecls mine-by experiment phase i: Excavation response.
- Rice, J., 1975, Continuum mechanics and thermodynamics of plasticity in relation to microscale deformation mechanisms. constitutive equations in plasticity: A.S. Argon, 23–79.
- Rice, J. R., 1968, A path independent integral and the approximate analysis of strain concentration by notches and cracks.
- Rice, J. R., et al., 1968, Mathematical analysis in the mechanics of fracture: *Fracture: an advanced treatise*, **2**, 191–311.
- Rudnicki, J., and K.-T. Chau, 1996, Multiaxial response of a microcrack constitutive model for brittle rock: Presented at the 2nd North American Rock Mechanics Symposium, OnePetro.
- Rutledge, J. T., and W. S. Phillips, 2003, Hydraulic stimulation of natural fractures as revealed by induced microearthquakes, carthage cotton valley gas field, east texashydraulic stimulation of natural fractures: *Geophysics*, **68**, 441–452.
- Sammis, C., and M. Ashby, 1986, The failure of brittle porous solids under compressive stress states: *Acta metallurgica*, **34**, 511–526.
- Scholz, 1968, Microfracturing and the inelastic deformation of rock in compression: *Journal of Geophysical Research*, **73**, 1417–1432.

- Scholz, C. H., 2019, *The mechanics of earthquakes and faulting*: Cambridge university press.
- Scott Jr, T., Z.-W. Zeng, J.-C. Roegiers, et al., 2000, Acoustic emission imaging of induced asymmetrical hydraulic fractures: Presented at the 4th North American Rock Mechanics Symposium, American Rock Mechanics Association.
- Shah, K., B. Carter, and A. Ingraffea, 1997, Hydraulic fracturing simulation in parallel computing environments: *International Journal of Rock Mechanics and Mining Sciences*, **34**, 474–474.
- Shipton, Z. K., 2012, Shale gas extraction in the uk: a review of hydraulic fracturing.: Presented at the .
- Shirzaei, M., W. L. Ellsworth, K. F. Tiampo, P. J. Gonzalez, and M. Manga, 2016, Surface uplift and time-dependent seismic hazard due to fluid injection in eastern texas.: *Science*.
- Sibson, R. H., 1990, Rupture nucleation on unfavorably oriented faults: *Bulletin of the Seismological Society of America*, **80**, 1580–1604.
- Soeder, D. J., 2018, The successful development of gas and oil resources from shales in north america: *Journal of Petroleum Science and Engineering*.
- Stead, D., E. Eberhardt, and J. Coggan, 2006, Developments in the characterization of complex rock slope deformation and failure using numerical modelling techniques: *Engineering geology*, **83**, 217–235.
- Stein, S., and M. Wysession, 2009, *An introduction to seismology, earthquakes, and earth structure*: John Wiley & Sons.
- Stone, D., D. Kamineni, A. Brown, and R. Everitt, 1989, A comparison of fracture styles in two granite bodies of the superior province: *Canadian Journal of Earth Sciences*, **26**, 387–403.

- Topin, V., J. Y. Delelle, F. Radjai, L. Brendel, and F. Mabilie, 2007, Strength and failure of cemented granular matter.: The European Physical Journal E, **23**, 413–429.
- van der Baan, M., and D. Chorney, 2019, Insights from micromechanical modeling of intact rock failure: Event characteristics, stress drops, and force networks: Journal of Geophysical Research: Solid Earth, **124**, 12955–12980.
- , 2019, Insights from micromechanical modeling of intact rock failure: Event characteristics, stress drops, and force networks: Journal of Geophysical Research: Solid Earth, **124**, 12955–12980.
- van der Pluijm, B., and S. Marshak, 2004, An introduction to structural geology and tectonics.
- Vandamme, L., and J. Curran, 1989, A three-dimensional hydraulic fracturing simulator: International Journal for Numerical Methods in Engineering, **28**, 909–927.
- Verlet, L., 1967, Computer” experiments” on classical fluids. i. thermodynamical properties of lennard-jones molecules: Physical review, **159**, 98.
- Wang, P.-t., T.-h. Yang, T. Xu, Q.-l. Yu, and H.-l. Liu, 2013, A model of anisotropic property of seepage and stress for jointed rock mass: Journal of Applied Mathematics, **2013**.
- Wang, Y., C. Li, and Y. Z. Hu, 2018, Experimental investigation on the fracture behaviour of black shale by acoustic emission monitoring and ct image analysis during uniaxial compression: Geophysical Journal International.
- Warpinski, N. R., J. Du, and U. Zimmer, 2012, Measurements of hydraulic-fracture-induced seismicity in gas shales: Spe Production & Operations.

- Warpinski, N. R., Z. Moschovidis, C. Parker, I. Abou-Sayed, et al., 1994, Comparison study of hydraulic fracturing models—test case: Gri staged field experiment no. 3 (includes associated paper 28158): SPE Production & Facilities, **9**, 7–16.
- Wells, A., 1961, Unstable crack propagation in metals: cleavage and fast fracture: Presented at the Proceedings of the crack propagation symposium.
- Wriggers, P., 2008, Nonlinear finite element methods: Springer Science & Business Media.
- Wyllie, D. C., 2017, Rock strength properties and their measurement, *in* Rock slope engineering: CRC Press, 117–162.
- Yang, B., Y. Jiao, and S. Lei, 2006, A study on the effects of microparameters on macroproperties for specimens created by bonded particles: Engineering Computations.
- Yokoi, H., 1968, Relationship between soil cohesion and shear strength: Soil Science and Plant Nutrition, **14**, 89–93.
- Young, R. P., J. F. Hazzard, and W. Pettitt, 2000, Seismic and micromechanical studies of rock fracture: Geophysical Research Letters.
- Zhang, Y., Z. Shao, W. Wei, and R. Qiao, 2019, Pfc simulation of crack evolution and energy conversion during basalt failure process: Journal of Geophysics and Engineering, **16**, 639–651.